Die approbierte Originalversion dieser Diplom-/Masterarbeit ist in der Hauptbibliothek der Technischen Universität Wien aufgestellt und zugänglich.

http://www.ub.tuwien.ac.at

TU UB WIEN Universitätsbibliothek

The approved original version of this diploma or master thesis is available at the main library of the Vienna University of Technology.

http://www.ub.tuwien.ac.at/eng

TECHNISCHE UNIVERSITÄT WIEN
Vienna University of Technology

DIPLOMARBEIT

Microscopic Modeling of NBTI in MOS Transistors

ausgeführt zum Zwecke der Erlangung des akademischen Grades eines Diplom-Ingenieurs unter der Leitung von

Ao.Univ.Prof. Dipl.-Ing. Dr.techn. Tibor Grasser

E360 - Institut für Mikroelektronik

und der Assistenz von

Dipl.-Ing. Dr.techn. Wolfgang Gös

E360 - Institut für Mikroelektronik

und

Dipl.-Ing. Markus Karner

Global TCAD Solutions

eingereicht an der Technischen Universität Wien

Fakultät für Elektrotechnik und Informationstechnik

von

Gerhard Rzepa BSc

0625735 / E 066 439

Berg 3, 3071 Böheimkirchen

Wien, im November 2013

Kurzfassung

Instabiles Verhalten von Transistorparametern in MOS Technologien ist seit jeher bekannt, trotzdem konnten die Ursachen dafür noch nicht vollständig geklärt werden. Durch die immer dünneren Oxidschichten in modernen Strukturen wirken sich speziell die temperatur- und gatespannungsabhängigen Instabilitäten (Bias Temperature Instabilities - BTI) immer entscheidender auf die Funktionalität und die Lebensdauer von Bauelementen aus.

Die intensive Forschung der letzten Jahre hat gezeigt, dass die Effekte im Zusammenhang mit BTI durch die Nonradiative Multiphonon (NMP) Theorie beschrieben werden können. Daraus wurde das NMP Four State Modell entwickelt, welches den Austausch von Ladungsträgern mit Störstellen im Oxid beschreibt. Um die komplexen BTI-Vorgänge erfassen zu können, berücksichtigt dieses Modell zwei stabile und zwei metastabile Zustände. Durch Messungen an kleinen Strukturen mittels Time Dependent Defect Spectroscopy konnte festgestellt werden, dass es Störstellen mit grundlegend unterschiedlichen Gatespannungsabhängigkeiten der Emissionszeitkonstanten gibt. Die in dieser Arbeit durchgeführten Simulationen konnten dank der metastabilen Zustände des NMP Four State Modells die Temperatur- und Gatespannungsabhängigkeit verschiedener Störstellen richtig reproduzieren.

Um BTI von großen Strukturen beschreiben zu können, muss eine Vielzahl von Störstellen berücksichtigt werden. Messungen lieferten Hinweise auf Störstellen, die sich nicht mehr entladen, sobald sie einen Ladungsträger eingefangen haben. Diese Störstellen werden oft mit Zuständen an der Grenzschicht zwischen Oxid und Substrat in Verbindung gebracht und können mittels eines Double Well Modells beschrieben werden. Mit diesen beiden Modellen ist eine vollständige Charakterisierung von BTI-Vorgängen großer Strukturen für verschiedene Temperaturen und Gatespannungen möglich. Um eine gute Übereinstimmung der durchgeführten Simulationen mit den Messdaten von einem pMOSFET zu erzielen, wurden die Parameter der Modelle optimiert. Die so erhaltenen Parameter wurden verwendet, um Capture/Emission Time (CET) Maps zu berechnen und ihre Form hinsichtlich Temperatur- und Gatespannungsabhängigkeit zu untersuchen. Zusätzlich wurden theoretische Betrachtungen zu CET Maps angestellt, die auf analytischen Berechnungen und Simulationen basieren. Diese Untersuchungen ermöglichten einen detaillierten Einblick in das Verhalten des NMP Four State Modells, und bestätigten, dass dieses Modell BTI-Effekte korrekt beschreibt.

Abstract

Instabilities of transistor parameters have been observed since the beginnings of the MOS technology, but they are still not fully understood. Especially the thinning of oxide layers in modern devices has further increased the effect of the bias and temperature induced instabilities (BTI) on the functionality and lifetime of modern devices.

In recent studies BTI effects were described with the help of the non-radiative multi-phonon (NMP) theory. This led to the NMP four state model, which is able to explain many effects related to BTI. This model is based on the exchange of charge carriers with oxide defects. In addition to two stable states, it considers two metastable states, which are essential to capture the complex processes involved in BTI. Measurement data obtained by time dependent defect spectroscopy on small-area devices has revealed defects with distinct bias dependence of their emission time constants. Using the metastable states of the NMP four state model, the temperature and bias dependence of the time constants of different defect types have been simulated and correctly reproduced in this work.

In order to describe BTI of large-area devices, a multitude of defects have to be considered. Measurements indicated defects which do not recover once they have captured a charge. These defects are typically linked to interface states, which can be described by a double well model. With these two models, BTI of large-area devices has been studied through simulations in this thesis. The model parameters have been optimized to obtain a good match with the experimental data of pMOSFETs for different gate bias and temperatures. Based on the obtained model parameters for the defects, capture/emission time (CET) maps have been calculated and the effects of temperature and gate bias on the shape of these maps have been analyzed. Furthermore, a theoretical study of CET maps, including analytical calculations and simulations, have been conducted. These investigations provide a detailed insight into the behavior of the NMP four state model, confirming that the model correctly describes BTI effects.

Acknowledgement

A few semesters ago, Prof. Tibor Grasser drew my interest to the modeling of semiconductor devices with his inspiring lecture, and I was very happy about the chance to work on a master thesis under his direction.

Next to Prof. Tibor Grasser, who topped my high expectations and fueled my motivation with his contributions to this work, I also want to thank many other people for valuable discussions and suggestions.

First of all, I want to thank Dr. Wolfgang Gös. Without his endless effort and support, I would not have been able to complete the work to the level of quality in which it is presented in this thesis. He improved my understanding and shared his knowledge about defect modeling in countless discussions regarding this work.

In the last years of my work at Global TCAD Solutions I always enjoyed the competent guiding of Markus Karner. His passion for the modeling of semiconductor devices was inspiring. I am grateful that Global TCAD Solutions funded my master thesis and I was very lucky being supported by such an excellent team. Christian Kernstock, Ferdinand Mitterbauer, Philipp Prause, and Klaus Schnass always followed my requests with helpful software updates and the work of Dr. Oliver Triebl was essential for my simulations.

At the institute of microelectronics, Prof. Erasmus Langer and Prof. Siegfried Selberherr ensured great working conditions. Prof. Hans Kosina raised my interest with an outstanding lecture on quantum mechanics and my colleagues at this institute were always friendly and supportive. Zlatan Stanojevic provided the LaTeX template for this work, and further valuable contributions were made by Dr. Franz Schanovsky, Michael Waltl, Stefanie Wolf, Yannick Wimmer, Markus Bina, Johannes Hanke, Markus Kampl, and many others.

Furthermore, I want to thank the competent staff of the institute of sensor and actuator systems, first and foremost Prof. Ulrich Schmid, who will be on the examining committee. My work at this institute sparked my interest in scientific research during the last semesters.

Finally, it is hard to find words to express my gratitude to my family and friends. I hope each of them know their importance in my life.

Contents

1 Introduction **1**
1.1 Motivation 1
1.2 Focus and Scope of this Work 1
1.3 The Structure of this Work 2

2 Bias Temperature Instability **3**
2.1 Definition and Effects 3
2.2 Measurement Techniques 4
2.2.1 Measure-Stress-Measure 4
2.2.2 On-The-Fly Measurement 4
2.2.3 Time-Dependent Defect Spectroscopy 4
2.2.4 Capture/Emission Time Map 6
2.3 Recoverable Defects 8
2.3.1 Oxygen Vacancy 8
2.3.2 Hydrogen Bridge 9

3 Modeling of BTI Traps **11**
3.1 NMP Transitions 11
3.1.1 Configuration Coordinate Diagram 11
3.1.2 Energy Mimima 12
3.1.3 Quantum Mechanical Derivation of Transition Rates 14
3.1.4 Transition Rates for a Continuous Band of States 15
3.1.5 Approximated Transition Rates 16
3.1.6 Energy Barriers 18
3.1.7 Electron-Phonon Coupling Regimes 19
3.2 Pure Thermal Barriers 21
3.3 NMP Four State Model 24
3.3.1 States and Definitions 24
3.3.2 Transition Rates 25
3.3.3 Occupation Probabilities and Charges 26
3.3.4 Capture and Emission Times 27

3.4 Double Well Model 28
3.4.1 Configuration Coordinate Diagram 28
3.4.2 Rates and Occupation Probabilities 28
3.4.3 Charge and Time Constants 30

4 Single Trap Simulation **31**
4.1 Measurement Data 31
4.2 Simulation Setup 32
4.2.1 Device Generation 32
4.2.2 Device Simulation 32
4.2.3 NMP Four State Model 33
4.2.4 Parameter Optimization 33
4.3 Results 34
4.3.1 Fixed Positive Charge Trap 34
4.3.2 Switching Trap 34
4.4 Regimes 37
4.4.1 Capture Time Constant 38
4.4.2 Emission Time Constant 40
4.5 Conclusions 41

5 Simulation of Degradation **43**
5.1 Measurement Data 43
5.1.1 Threshold Voltage Shift 43
5.1.2 CV Curve 44
5.2 Device Generation 44
5.2.1 Geometry 44
5.2.2 Device Optimization 46
5.3 Device Simulation 46
5.3.1 General Simulation Setup 46
5.3.2 NMP Four State Model 50
5.3.3 Double Well Model 51
5.3.4 Threshold Voltage Shift 52
5.4 Optimization of the Model Parameters 53
5.5 Results 56
5.5.1 Threshold Voltage 56
5.5.2 Band Diagram 57
5.5.3 CET Map 58
5.6 Conclusions 61

6 CET Map Considerations **63**
6.1 NMP Four State Model 63
6.1.1 Bias Dependence 63
6.1.2 Temperature Dependence 64
6.1.3 Negative Weak Electron-Phonon Coupling 66

6.2 Equilibrium Occupancy Difference 66
6.2.1 General Expression for NMP Transitions 68
6.2.2 Relation to Time Constants 69
6.2.3 Temperature Dependence 72
6.2.4 Intersection Point Difference 72
6.2.5 Dependence on the Electric Field and the Trap Positions 76
6.2.6 Estimated Distributions 76
6.3 Comparison of Results 78
6.4 Conclusions 82

7 Summary and Outlook **83**

Bibliography **85**

CHAPTER 1 Introduction

1.1 Motivation

In order to increase the performance of integrated circuits, their geometry was scaled dramatically in the past decades. Especially the thinning of oxide layers between two conducting or semiconducting materials lead to improvements. At the same time, the scaling intensified known issues and brought up new ones which have to be addressed. Beside well understood processes, like the tunneling of carriers through oxide layers, phenomena which are not fully established yet, such as the random telegraph noise (RTN) [1, 2] and bias temperature instabilities (BTI) [3, 4], became crucial. Both, RTN and BTI are traced back to charge exchange of the oxide with the adjacent layers. Because of the amorphous structure of typical oxide materials, direct measurements are difficult and even density functional theory (DFT) simulations of possible defect structures [5, 6, 7, 8] were not able to explain the ongoing processes so far. However, based on the experimental information available, accurate microscopic models have been developed in the past few years [9]. These models can describe the phenomena linked to charge trapping of oxide layers. Even though the development of these models was based on a vague idea about the processes involved, they promote the understanding of BTI and contribute to a further improvement of the performance of modern circuits.

1.2 Focus and Scope of this Work

Based on microscopic models, BTI of metal-oxide-semiconductor field effect transistors (MOSFET) will be investigated. The investigations will cover BTI at negative gate voltages (NBTI) and p-channel MOSFETs (pMOSFET), as the severest degradation is observed for this case [3, 4]. BTI will be modeled within the non-radiative multi-phonon (NMP) four state model and a double well model but the detailed discussions will focus on the former. Beside the transitions between the valence band and the oxide defects, the contributions of the charge carriers of the conduction band will be included. The time constants of single traps will be simulated for different temperatures and gate voltages, and a multitude of those defects will be used to handle large-area devices. Furthermore, a major topic will be the simulation and interpretation of capture/emission time maps.

1.3 The Structure of this Work

The phenomenon of BTI and related measurements will be introduced and possible defect candidates will be outlined in **Chapter 2**, followed by a comprehensive description of the NMP four state model and a double well model in **Chapter 3**.

In **Chapter 4** and **Chapter 5** the previously introduced models are applied to describe the behavior of single traps and reproduce BTI of large-area devices, respectively. The results will be discussed with regard to their bias and temperature dependence.

Chapter 6 focuses on CET maps. Their bias and temperature dependent behavior will be analyzed and possible contributions of traps will be estimated.

CHAPTER 2 Bias Temperature Instability

2.1 Definition and Effects

The shift of MOSFET parameters over time is termed “degradation” and is often quantified by the threshold voltage shift $\Delta V_{\mathrm{th}}(t)$. Even for constant voltages at the source, drain, bulk, and gate terminals and a stable temperature a degradation can be observed. The threshold voltage shifts faster at higher gate voltages and higher transistor temperatures. For the case of a negligible source/drain voltage, this phenomenon is termed “bias temperature instability” [3, 4]. Depending on the sign of the applied gate voltage, the case of negative BTI and positive BTI is distinguished.

Modern semiconductor technologies show increasing susceptibility to BTI. As circuit switching speeds, charging times, and device lifetime can be affected [10], the cause of BTI has been investigated excessively in the past years. Still, the microscopic nature of the defects causing BTI is controversial but the key characteristics of BTI can be described based on the phenomenologically classified border traps [11, 12]. These border traps suggest a connection between BTI and other non-ideal transistor behaviors, such as the random telegraph and $1/f$ noise [9].

It was found that a previously stressed device does not fully recovery, even for large measurement times [13]. Various measurements of degradation and defects indicated that the recoverable component of this degradation can be ascribed to the charging of pre-existing oxide defects, whereas the non-recovering component might be caused by the creation of new interface states [14, 13]. Actually, the latter recovers eventually, but the emission times of the corresponding traps are larger than any reasonable measurement time and therefore this component will be termed “permanent”. In the following, measurement techniques which are related to BTI will be described and possible defects will be discussed.

2.2 Measurement Techniques

In order to extract the bias dependence of the device degradation, BTI measurements are usually based on stress/recovery phases. Initially a low gate voltage V_G^L is applied to the measured MOSFET, until the threshold voltage V_{th} does not change anymore. At at the time $t = 0$, the gate voltage V_G is set to V_G^H and the threshold voltage starts to shift. After the stress time t_s, the gate voltage is set to V_G^L again, and the threshold voltage will start to shift backwards until the end of the measurement at $t = t_r + t_s$, where t_r is the recovery time.

2.2.1 Measure-Stress-Measure

With the measure-stress-measure (MSM) technique, the threshold voltage $V_{th}(t)$ of a stress/recovery phase can be obtained [15]. First, a reference level for the drain current $I_D(V_G^L)$ has to be determined at $t < 0$. In the stress phase at $0 < t < t_s$, no measurements are carried out at V_G^H, but the gate voltage repeatedly switches to V_G^L for short periods of time, in order to determine the drain current $I_D(V_G^L)$. These short measurements are done with a minimum delay of Δt_{delay}, and the part of ΔV_{th} which recovers quickly, can not be measured. The obtained drain currents can be mapped to V_{th} with the help of the transfer characteristics of the transistor around V_{th}. As there is a significant threshold voltage shift nearly instantaneously after $t = t_s$, it is important to make Δt_{delay} as small as possible.

2.2.2 On-The-Fly Measurement

Similar to MSM setups, on-the-fly (OTF) measurements [16] are designed to determine the threshold voltage shift of stress/recovery phases. But, in contrast to the MSM technique, V_{th} is measured during both, high and low gate voltage. This requires a mapping of the measured drain current in the linear regime $I_D(V_G^H)$ to a threshold voltage shift. Using a simple mapping, the threshold voltage shift can be calculated with the threshold voltage V_{th0} and the reference value $I_{D0}(V_G^L)$ as [15]

$$\Delta V_{th} \approx \frac{I_D - I_{D0}}{I_{D0}}(V_G - V_{th0}). \tag{2.1}$$

2.2.3 Time-Dependent Defect Spectroscopy

As the microscopic nature of BTI traps is still unclear, measurements of single traps are important to improve the understanding of the underlying process of BTI. The time-dependent defect spectroscopy [2, 17] (TDDS) is such a measurement, as it provides the capture and emission time constants τ_c and τ_e of single traps at different gate voltages and temperatures. Usually, a lot of traps contribute to a threshold voltage shift, and the resulting recovery traces $\Delta V_{th}(t > t_s)$ will show a continuous decrease of the threshold voltage. In order to get information about single traps, the recovery traces of small area MOSFETs, where discrete steps are observed, have to be analyzed. TDDS measurements

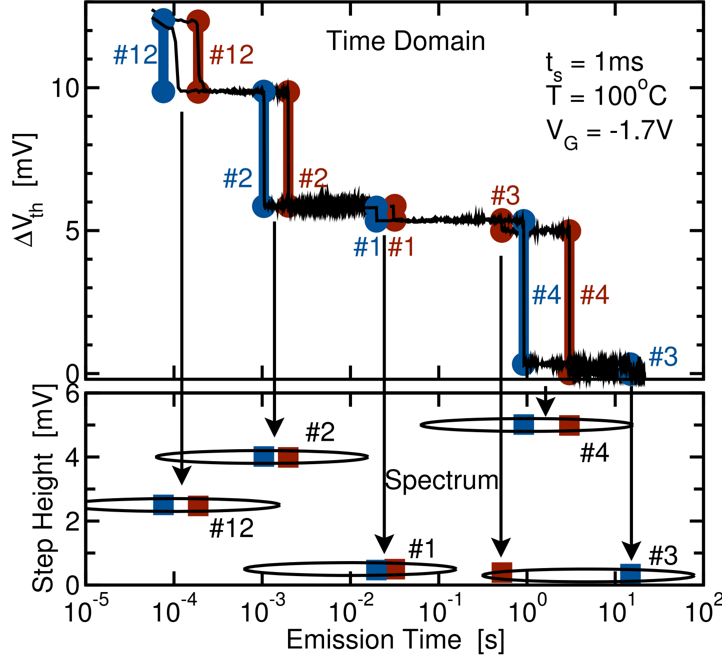

Figure 2.1: **Top**: Exemplary recovery traces with discrete steps which are related to single hole emission events. **Bottom**: The mapping of those steps according to their step height and emission time, indicated by the vertical arrows, results in a spectral map [2].

are based on the assumption that step heights in recovery traces are characteristics of traps. The latter assumption is reasonable, because the step heights are mainly governed by the position of the corresponding trap. Thereby discrete steps in the recovery traces can be linked to a certain trap, even for different measurement conditions. As the emission times are stochastic quantities, a number of recovery traces have to be recorded at the same conditions. For each step in each recovery trace, a step height and an emission time can be collected. With this data, a spectral map can be created [2, 18], as shown in Figure 2.1 [2]. The maxima of the clusters in such spectral maps represent the average emission time constants of the traps. To get information about the corresponding capture time constants, the measurement as described above has to be repeated for N different stress times $t_\mathrm{s} = \{t_{\mathrm{s},1}, t_{\mathrm{s},2}, \ldots t_{\mathrm{s},N}\}$ with $t_{\mathrm{s},i} > t_{\mathrm{s},i-1}$ and $i \epsilon \{1, 2, \ldots N\}$. If a cluster at an emission time τ_e can be observed in the spectral map i but disappears in the spectral map $i-1$ the corresponding capture time constant of the trap has to be between $t_{\mathrm{s},i-1}$ and $t_{\mathrm{s},i}$. As single traps of such small area devices can be identified via their step heights, the TDDS measurement can be repeated for different gate voltages and temperatures. Thereby, TDDS provides capture and emission time constants of single traps for different temperatures and gate voltages.

Recovery traces of small devices sometimes show a random switching between two voltage levels, which appears to be uncorrelated to t_s and t_r. Such random telegraph

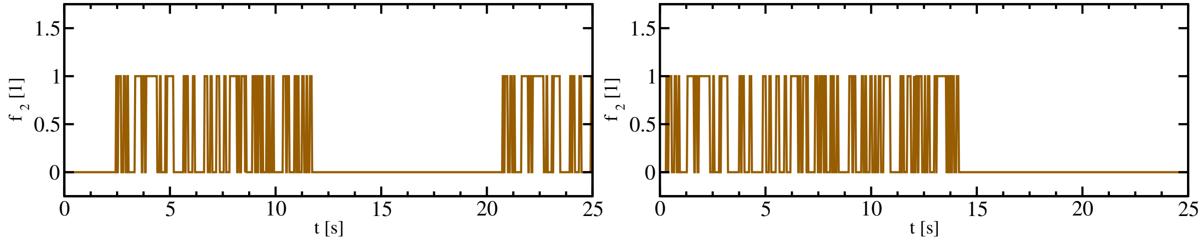

Figure 2.2: Exemplary anomalous (left) and temporary (right) RTN signals simulated on a small area pMOSFET [2].

noise (RTN) can cause detection failures in TDDS measurements. Studies on RTN [1] in MOSFETs revealed defects, which repeatedly produce noise in the drain current for stochastic amounts of time (compare Figure 2.2). This phenomenon was termed "anomalous RTN". A similar phenomenon termed "temporary RTN" was observed recently [2]: after a stress phase, a noise in the drain current can be observed, which disappears after some time and, but does not reappear within reasonable measurement times (compare Figure 2.2). Both phenomena indicate the existence of metastable states.

2.2.4 Capture/Emission Time Map

The threshold voltage shift during a stress/recovery phase usually includes contributions of a lot of traps with a wide distribution of time constants. But, while the time constants of the single traps are obscured in MSM and OTF measurements, TDDS is designed for measurements on small area devices with few traps. The CET map [9, 19], which is outlined in the following, can provide information about the distribution of time constants even for large devices. A CET map represents the density $g(\tau_\mathrm{c}^\mathrm{H}, \tau_\mathrm{e}^\mathrm{L})$ with the time constants $\tau_\mathrm{c}^\mathrm{H}$ and $\tau_\mathrm{e}^\mathrm{L}$ defined as

$$\tau_\mathrm{c}^\mathrm{H} = \tau_\mathrm{c}(V_\mathrm{G}^\mathrm{H}) \tag{2.2}$$
$$\tau_\mathrm{e}^\mathrm{L} = \tau_\mathrm{e}(V_\mathrm{G}^\mathrm{L}). \tag{2.3}$$

This density is related to the trap density and their charge difference at V_G^L and V_G^H and can be extracted from the threshold voltage shift ΔV_th of a stress/recovery phase according to [9]

$$g(\tau_\mathrm{c}, \tau_\mathrm{e}) \approx -\frac{\partial^2 \Delta V_\mathrm{th}(\tau_\mathrm{c}, \tau_\mathrm{e})}{\partial \tau_\mathrm{c} \partial \tau_\mathrm{e}}. \tag{2.4}$$

Therefore, the threshold voltage shift after a stress/recovery phase with the stress time t_s and the relaxation time t_r can be obtained by the equation [9]

$$\Delta V_\mathrm{th}(t_\mathrm{s}, t_\mathrm{r}) \approx \int_0^{t_\mathrm{s}} \mathrm{d}\tau_\mathrm{c} \int_{t_\mathrm{s}}^{\infty} \mathrm{d}\tau_\mathrm{e} g(\tau_\mathrm{c}, \tau_\mathrm{e}). \tag{2.5}$$

Thus, ΔV_th is obtained by integrating the CET map from 0 s to t_s and from t_r to ∞. The other way round, CET maps can be constructed by taking the mixed partial derivative

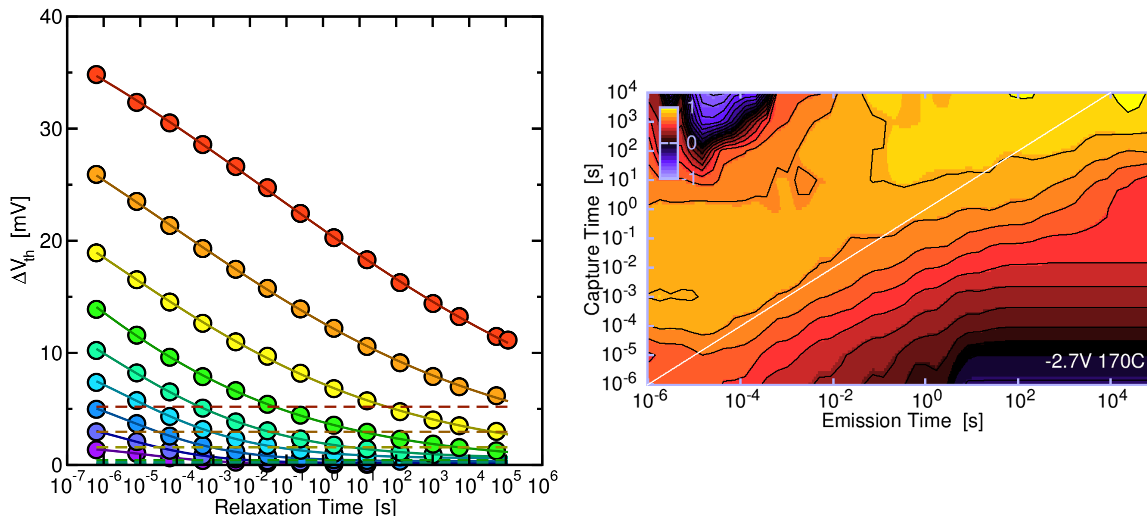

Figure 2.3: Based on $\Delta V_{\mathrm{th}}(t_{\mathrm{s}}, t_{\mathrm{r}})$ of measured recovery traces (circles in the left figure), a CET map (right) can be calculated. The obtained CET map represents the contribution of traps to ΔV_{th}, depending on their time constants $\tau_{\mathrm{c}}^{\mathrm{H}}$ and $\tau_{\mathrm{e}}^{\mathrm{L}}$. The other way round, a threshold voltage shift can be obtained by integrating the density $g(\tau_{\mathrm{c}}^{\mathrm{H}}, \tau_{\mathrm{e}}^{\mathrm{L}})$ of CET maps (lines in the left figure) [9].

of recovery traces. An exemplary CET map together with the corresponding recovery traces is shown in Figure 2.3. Details of CET maps will be discussed in Section 5.5.3 and Chapter 6.

2.3 Recoverable Defects

The phenomenologically classified border traps [11, 12] are considered as the main contributors to BTI degradation. Measurements, such as the electron spin resonance (ESR) [20], can provide information about the behavior of these traps but their exact microscopic nature is still controversial. Some studies suggested the oxygen vacancy as a likely defect candidate [21], others brought up defects involving hydrogen bonds [22, 23, 6]. In this chapter these two defect types are discussed.

2.3.1 Oxygen Vacancy

The oxygen vacancy defect, or E' center, is a well studied defect, because early on, it was considered as the main positive defect responsible for BTI in MOS oxides. In a defect-free silicon dioxide, every silicon atom is bonded to four neighboring oxide atoms. Therefore, a missing oxygen can cause a covalent bond between two silicon atoms, which results in a stable neutral system. DFT calculations of atomic configurations suggested two different results for the case of hole trapping [7]: The dimer configuration and the puckered configuration of the positively charge defect. These two positive states are shown in Figure 2.4 [5, 6].

- In the dimer configuration the silicon atoms which face the vacancy, are slightly displaced from their initial equilibrium positions and share the remaining electron almost equally.
- In the puckered configuration a dangling bond occurs at one of the involved silicon atoms, and this atom is considerably distorted from its initial equilibrium position.

The puckered configuration has a considerably lower energy minimum than the dimer configuration. Therefore, after hole capture of the neutral oxide vacancy with the Si-Si bond, the defect is assumed to relax in the more favorable puckered configuration, if it has enough energy to overcome the energy barrier between the dimer and the puckered configuration. Otherwise it will remain in the dimer configuration. Beside the transition via the dimer state, an immediate relaxation into the puckered configuration was suggested [7]. A fourth state of the neutral oxygen vacancy, was assumed [24, 25], caused by annealing processes, but this is not rigorously studied yet.

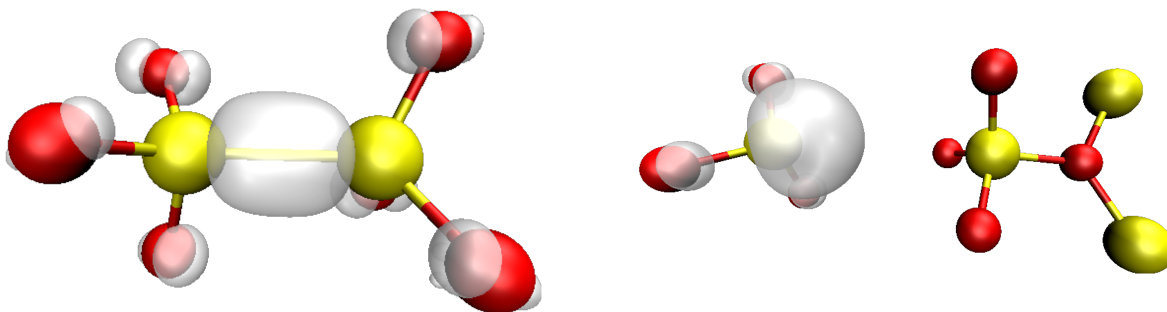

Figure 2.4: DFT results of two configurations of the oxygen vacancy [5, 6]. **Left**: The neutral oxygen vacancy with a covalent bond between the two silicon atoms. **Right**: The positive puckered configuration, which is more stable than the positive dimer configuration (not shown here). Compared to the neutral oxygen vacancy, the distance between the silicon atoms is larger and one atom has a dangling bond.

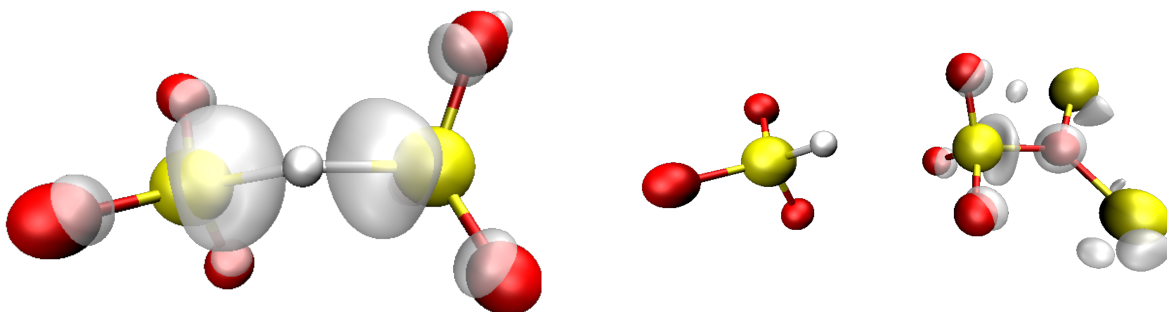

Figure 2.5: DFT results of two positive configurations of the hydrogen bridge [5, 6]. **Left**: The hydrogen is weakly bonded to both neighboring silicon atoms. **Right**: In the positive "broken" configuration the hydrogen has a covalent bond to one of the silicon atoms. The distance between the two silicon atoms is larger, compared to the positive configuration with weak bondings.

2.3.2 Hydrogen Bridge

The replacement of an oxygen atom by a hydrogen atom in silicon dioxide gives the defect structure of a hydrogen bridge. As hydrogen is available in considerable amounts, this defect is discussed as a potential contributor to BTI. For both, the positively charged and the neutral hydrogen bridge defect, the hydrogen can either have a weak bond to both neighbouring silicon atoms, or a strong bond to one of the silicon atoms, resulting in a dangling bond of the other silicon atom. The two configurations of the positive charged hydrogen bride are depicted in Figure 2.5 [5, 6]. If a neutral oxygen defect with a dangling bond captures a hole, the hydrogen shifts towards the center of the bridge, instead of being localized at on silicon atom [6, 26].

CHAPTER 3 Modeling of BTI Traps

As discussed in Chapter 2, BTI can be ascribed to charge capture and emission between the oxide traps, the semiconductor, and the gate of a transistor. The resulting charge of the oxide traps affects the channel region and thereby causes BTI. These oxide defects have been classified as permanent or recoverable traps based on their emission times. The latter can be described within the nonradiative multiphonon (NMP) theory [9, 27]. In this chapter the NMP transition as well as pure thermal transitions are introduced. They are both part of the NMP four state model [9], which will be explained afterwards. Finally, the double well model [25] is discussed, as it can be used to describe the permanent component of BTI degradation.

3.1 NMP Transitions

3.1.1 Configuration Coordinate Diagram

When electrons or holes are captured in or emitted from oxide defects, their charges influence the surrounding electrons and nuclei. These interactions can be described by the Schrödinger equation for this system of electrons and nuclei. These interactions are commonly described in a Born-Oppenheimer picture [28]. In this picture, the quantum mechanical state of the electronic system causes a potential, that acts on the nuclei. Different quantum mechanical states give rise to different potentials, which are called "potential energy surfaces".

The potential energy surface of a system in state i with N atoms is represented by a $3N$-dimensional surface as it depends on the three spatial coordinates of each atom. The global energy minimum $V_{i,\min}$ of this multidimensional surface corresponds to the most stable atomic configuration. With respect to transitions from the energy minimum $V_{i,\min}$ of state i to the energy minimum $V_{j,\min}$ of state j, only the transition path at the potential energy surface is of relevance. Even though this path along the $3N$-dimensional surface does not corresponds to a real coordinate, it can represented by the configuration coordinate q, which includes the energy mimima $V_{i,\min}$ and $V_{j,\min}$ at the equilibrium positions q_i and q_j, respectively. Still, the system energy $V(q)$ along the configuration coordinate can be quite complex. However, for sufficiently small displacements from

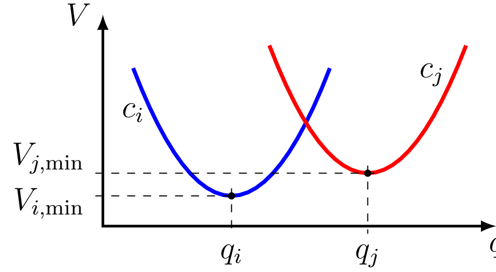

Figure 3.1: The system energy along the configuration coordinate q is approximated by a quantum harmonic oscillator for each state of the system.

the equilibrium position, the potential energy curve can be approximated by a quantum harmonic oscillator. With the curvature c_i, the potential of the corresponding quantum harmonic oscillator (compare Figure 3.1) reads

$$V_i(q) = V_{i,\min} + c_i(q - q_i)^2. \tag{3.1}$$

3.1.2 Energy Mimima

NMP transitions can describe an electron transfer between the conduction or valence band of a semiconductor and an oxide trap. In the following a system with one donor-like defect and one electron, which can move between the defect and the semiconductor via NMP transitions is considered. If the electron is in the semiconductor, it is assumed to be located at the interface to the oxide, where it lies at one of the band edges. For such a system, three different states can be identified:

- State i with system energy minimum $V_{i,\min}$: The trap is neutral as the electron is at the oxide trap.
- State j^{V} with system energy minimum $V^{\mathrm{V}}_{j,\min}$: The trap is positive and the electron is in the semiconductor at the valence band edge.
- State j^{C} with system energy minimum $V^{\mathrm{C}}_{j,\min}$: The trap is positive and the electron is in the semiconductor at the conduction band edge.

Regarding NMP transitions, the total system energies of the different states are not important, but their differences between the energy mimima will be of interest in later discussions. For simplicity, it is assumed that the transfer of an electron does not affect other electrons or nuclei. During an NMP transition, the energy of the electron itself can change by ΔE_{el}, which results in an increase of the system energy by ΔE_{el} as well. Obviously, an electron increases its energy by $\Delta E_{\mathrm{el}} = E_{\mathrm{C}} - E_{\mathrm{V}}$ if it moves from the valence band edge to the conduction band edge. Therefore, a relation between the energy mimima $V^{\mathrm{V}}_{j,\min}$ and $V^{\mathrm{C}}_{j,\min}$ can be written as

$$V^{\mathrm{C}}_{j,\min} = V^{\mathrm{V}}_{j,\min} + \Delta E_{\mathrm{el}} = V^{\mathrm{V}}_{j,\min} + E_{\mathrm{C}} - E_{\mathrm{V}}. \tag{3.2}$$

If the electron moves from the valence band edge to the oxide trap, it changes its energy by $\Delta E_{\mathrm{el}} = \Delta E_{\mathrm{t}}$. Hence, the energy mimima $V^{\mathrm{V}}_{j,\min}$ and $V_{i,\min}$ of the system are related by

$$V_{i,\min} = V^{\mathrm{V}}_{j,\min} + \Delta E_{\mathrm{el}} = V^{\mathrm{V}}_{j,\min} + \Delta E_{\mathrm{t}}. \tag{3.3}$$

In order to obtain an expression for ΔE_{t}, following definitions are useful:

- The distance x perpendicular to the interface of the oxide and the semiconductor is zero at the interface and $x > 0$ in the oxide.
- The valence band edge energy is given by $E_{\mathrm{V}}(x) = E_{\mathrm{V0}} - q_0\psi(x)$ with the valance band edge energy E_{V0} for flat band conditions, the elementary charge q_0, and the electrostatic potential $\psi(x)$.
- The electron energy at the trap position x_{t} is termed "trap level". Using the trap energy E_{t0} for flat band conditions, its dependence on the electrostatic potential can be expressed as

$$E_{\mathrm{t}}(x_{\mathrm{t}}) = E_{\mathrm{t0}} - q_0\psi(x_{\mathrm{t}}). \tag{3.4}$$

Based on these definitions, the increase of the electron if it moves from the valence band to the oxide trap can be written as

$$\Delta E_{\mathrm{t}} = E_{\mathrm{t}}(x_{\mathrm{t}}) - E_{\mathrm{V}}(x = 0) \tag{3.5}$$

$$= E_{\mathrm{t0}} - q_0\psi(x_{\mathrm{t}}) - E_{\mathrm{V0}} + q_0\psi(x = 0). \tag{3.6}$$

With the electric field F in the oxide, whose sign is assumed such that F increases with decreasing gate voltage V_{G}, the difference of the electrostatic potentials can be expressed as

$$q_0\psi(x = 0) - q_0\psi(x_{\mathrm{t}}) = q_0 x_{\mathrm{t}} F. \tag{3.7}$$

As a result ΔE_{t} reads

$$\Delta E_{\mathrm{t}} = E_{\mathrm{t0}} - E_{\mathrm{V0}} + q_0 x_{\mathrm{t}} F. \tag{3.8}$$

Substituting this expression in equation (3.3) the relation between $V^{\mathrm{V}}_{j,\min}$ and $V_{i,\min}$ is obtained as

$$V_{i,\min} = V^{\mathrm{V}}_{j,\min} + E_{\mathrm{t0}} - E_{\mathrm{V0}} + q_0 x_{\mathrm{t}} F. \tag{3.9}$$

Thus, the energy mimima $V^{\mathrm{V}}_{j,\min}$, $V^{\mathrm{C}}_{j,\min}$, and $V_{i,\min}$ can be related to each other by equations (3.2) and (3.9). Their absolute values depend on the reference energy. The results in the later chapters will be based on a reference level V_{ref}, defined as

$$V_{\mathrm{ref}} = \frac{V^{\mathrm{C}}_{j,\min} + V^{\mathrm{V}}_{j,\min}}{2} = 0. \tag{3.10}$$

Substituting this reference energy in equation (3.9) yields the system energies

$$V^{\mathrm{V}}_{j,\min} = -\frac{E_{\mathrm{C}} - E_{\mathrm{V}}}{2} \tag{3.11}$$

$$V^{\mathrm{C}}_{j,\min} = +\frac{E_{\mathrm{C}} - E_{\mathrm{V}}}{2}. \tag{3.12}$$

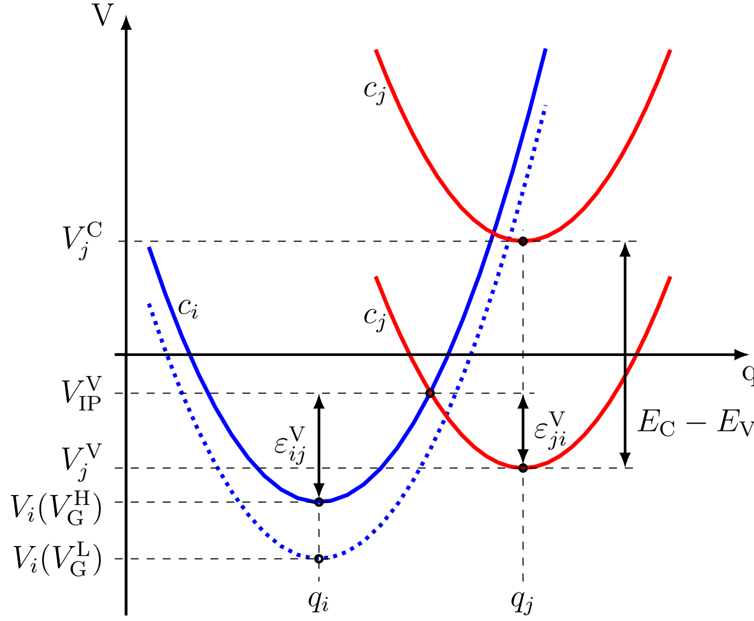

Figure 3.2: Schematic configuration coordinate diagram with the potential energy surface along the transition path for a neutral state i and a positive state j. In the positive state, the electron is either at the valence band edge (lower red line) or at the conduction band edge (upper red line). The energy minimum of the neutral state depends on the gate voltage V_{G} and on the trap level E_{t} according to equation (3.13). The blue dotted and the blue solid line represents the potential energy surface along the transition path of state i for a low ($V_{\mathrm{G}}^{\mathrm{L}}$) and a high ($V_{\mathrm{G}}^{\mathrm{H}}$) gate voltage, respectively. For $V_{\mathrm{G}}^{\mathrm{H}}$, the NMP barriers $\varepsilon_{ij}^{\mathrm{V}}$ and $\varepsilon_{ji}^{\mathrm{V}}$ between states i and j^{V} are shown.

E_{t0} is a trap parameter and in regard to the reference energy V_{ref} the system energy $V_{i,\mathrm{min}}$ is defined as

$$V_{i,\mathrm{min}} = E_{\mathrm{t0}} + q_0 x_{\mathrm{t}} F. \tag{3.13}$$

With these energy mimima, the potentials of the harmonic oscillator (3.1) read

$$\begin{aligned} V_j^{\mathrm{V}}(q) &= -\frac{E_{\mathrm{C}} - E_{\mathrm{V}}}{2} + c_j (q - q_j)^2 && (3.14) \\ V_j^{\mathrm{C}}(q) &= +\frac{E_{\mathrm{C}} - E_{\mathrm{V}}}{2} + c_j (q - q_j)^2 && (3.15) \\ V_i(q) &= E_{\mathrm{t0}} + q_0 x_{\mathrm{t}} F + c_i (q - q_i)^2. && (3.16) \end{aligned}$$

A corresponding configuration coordinate diagram is shown in Figure 3.2.

3.1.3 Quantum Mechanical Derivation of Transition Rates

Different charge states are associated with different energy potential surfaces and are therefore represented by different harmonic oscillators in the configuration coordinate

diagram. According to perturbation theory, the transition rate k_{ij} from state i to state j can be written as [6, 29]

$$k_{ij} = A_{ij} f_{ij}. \tag{3.17}$$

The electronic matrix element A_{ij} contains the electron wave functions of both states and accounts for possible tunneling processes. For device simulation an approximation of the electronic matrix element with a WKB factor [30] is reasonable. f_{ij} denotes the lineshape function [6, 29], which is defined as

$$f_{ij} = \underset{\alpha}{\text{ave}} \sum_{\beta} |\langle \eta_{i\alpha} | \eta_{j\beta} \rangle|^2 \delta(E_{i\alpha} - E_{j\beta}). \tag{3.18}$$

The Franck-Condon factor $|\langle \eta_{i\alpha} | \eta_{j\beta} \rangle|^2$ in the lineshape function increases with the overlap of the vibrational wave function α of the atomic configuration i with the vibrational wave function β of the atomic configuration j. The thermal average of the sum of the Franck-Condon factors of the corresponding vibrational wave functions result in the lineshape function. Details about the electronic matrix element and the lineshape function can be found in [6].

3.1.4 Transition Rates for a Continuous Band of States

In Section 3.1.2, it was assumed that the involved charge carriers in the semiconductor occupy an electric state at one of the band edges. However, these charge carriers are distributed over the conduction and the valance band. With the density of states of conduction (D_n) and valence band (D_p) and the carrier distribution functions for electrons (f_n) and holes (f_p), the concentration of electrons (n) and holes (p) are obtained by

$$n = \int_{E_\mathrm{C}}^{\infty} D_\mathrm{n}(E) f_\mathrm{n}(E) \mathrm{d}E \tag{3.19}$$

$$p = \int_{-\infty}^{E_\mathrm{V}} D_\mathrm{p}(E) f_\mathrm{p}(E) \mathrm{d}E. \tag{3.20}$$

Each charge carrier with the energy E can be described by an own system with a trap level E_t, the neutral state i, and the positive state j as explained in Section 3.1.2. Therefore, a transitions rate k_{ij} can be found for each of these systems, as discussed in Section 3.1.3. The sum of all these rates yields the rate between all states i and all states j. In the following, k_{ij} will denote the sum of the rates of the systems.

In general the energies of the charge carriers in the semiconductor are continuously distributed, and the total NMP transition rates for the valence and conduction band

can be written as [6, 29]

$$k_{ij}^{\mathrm{C}}(E,E_{\mathrm{t}}) = \int_{E_{\mathrm{C}}}^{\infty} D_{\mathrm{n}}(E)f_{\mathrm{p}}(E)A_{ij}(E,E_{\mathrm{t}})f_{ij}(E,E_{\mathrm{t}})\mathrm{d}E \tag{3.21}$$

$$k_{ji}^{\mathrm{C}}(E,E_{\mathrm{t}}) = \int_{E_{\mathrm{C}}}^{\infty} D_{\mathrm{n}}(E)f_{\mathrm{n}}(E)A_{ji}(E,E_{\mathrm{t}})f_{ji}(E,E_{\mathrm{t}})\mathrm{d}E \tag{3.22}$$

$$k_{ij}^{\mathrm{V}}(E,E_{\mathrm{t}}) = \int_{-\infty}^{E_{\mathrm{V}}} D_{\mathrm{p}}(E)f_{\mathrm{p}}(E)A_{ij}(E,E_{\mathrm{t}})f_{ij}(E,E_{\mathrm{t}})\mathrm{d}E \tag{3.23}$$

$$k_{ji}^{\mathrm{V}}(E,E_{\mathrm{t}}) = \int_{-\infty}^{E_{\mathrm{V}}} D_{\mathrm{p}}(E)f_{\mathrm{n}}(E)A_{ji}(E,E_{\mathrm{t}})f_{ji}(E,E_{\mathrm{t}})\mathrm{d}E. \tag{3.24}$$

3.1.5 Approximated Transition Rates

Analytical expressions for the transition rates (3.21) to (3.24) can be obtained, considering following approximations:

- The energies of the charge carriers in the semiconductor are strongly localized at the respective band edges. So the energy distributions (3.19) to (3.20) can be approximated by the respective band edge energies at the interface $E_{\mathrm{C}}^{\mathrm{s}}$ and $E_{\mathrm{V}}^{\mathrm{s}}$. The Fermi-Dirac distributions for electrons (f_{n}) and holes (f_{p}) are

$$f_{\mathrm{n}}(E) = \frac{1}{1+\mathrm{e}^{-\beta(E_{\mathrm{F}}-E)}} \tag{3.25}$$

$$f_{\mathrm{p}}(E) = \frac{1}{1+\mathrm{e}^{-\beta(-E_{\mathrm{F}}+E)}}. \tag{3.26}$$

With the Boltzmann constant k_{B} and the device temperature T, β is defined as

$$\beta = \frac{1}{k_{\mathrm{B}}T}. \tag{3.27}$$

The Fermi-Dirac distributions can be related to each other by

$$f_{\mathrm{n}}(E) = f_{\mathrm{p}}(E)\mathrm{e}^{-\beta(-E_{\mathrm{F}}+E)} \tag{3.28}$$

$$f_{\mathrm{p}}(E) = f_{\mathrm{n}}(E)\mathrm{e}^{-\beta(E_{\mathrm{F}}-E)}. \tag{3.29}$$

Substituting these expressions into the equations (3.21) to (3.24) one obtains

$$k_{ij}^{\mathrm{C}}(E,E_{\mathrm{t}}) = \int_{E_{\mathrm{C}}}^{\infty} D_{\mathrm{n}}(\mathrm{E}) f_{\mathrm{n}}(E) A_{ij}(E,E_{\mathrm{t}}) f_{ij}(E,E_{\mathrm{t}}) \mathrm{e}^{-\beta(E_{\mathrm{F}}-E)} \mathrm{d}E \tag{3.30}$$

$$k_{ji}^{\mathrm{C}}(E,E_{\mathrm{t}}) = \int_{E_{\mathrm{C}}}^{\infty} D_{\mathrm{n}}(\mathrm{E}) f_{\mathrm{n}}(E) A_{ji}(E,E_{\mathrm{t}}) f_{ji}(E,E_{\mathrm{t}}) \mathrm{d}E \tag{3.31}$$

$$k_{ij}^{\mathrm{V}}(E,E_{\mathrm{t}}) = \int_{-\infty}^{E_{\mathrm{V}}} D_{\mathrm{p}}(\mathrm{E}) f_{\mathrm{p}}(E) A_{ij}(E,E_{\mathrm{t}}) f_{ij}(E,E_{\mathrm{t}}) \mathrm{d}E \tag{3.32}$$

$$k_{ji}^{\mathrm{V}}(E,E_{\mathrm{t}}) = \int_{-\infty}^{E_{\mathrm{V}}} D_{\mathrm{p}}(\mathrm{E}) f_{\mathrm{p}}(E) A_{ji}(E,E_{\mathrm{t}}) f_{ji}(E,E_{\mathrm{t}}) \mathrm{e}^{-\beta(-E_{\mathrm{F}}+E)} \mathrm{d}E. \tag{3.33}$$

As we approximate the energy of the carriers by $E_{\mathrm{C}}^{\mathrm{s}}$ and $E_{\mathrm{V}}^{\mathrm{s}}$, respectively, the electronic matrix element and the lineshape function are not a function of the integrand anymore, and substituting equations (3.19) and (3.20) in the transition rates (3.30) to (3.33) yields

$$k_{ij}^{\mathrm{C}} = nA_{ij}(E_{\mathrm{C}}^{\mathrm{s}},E_{\mathrm{t}}) f_{ij}(E_{\mathrm{C}}^{\mathrm{s}},E_{\mathrm{t}}) \mathrm{e}^{-\beta(E_{\mathrm{F}}-E_{\mathrm{C}}^{\mathrm{s}})} \tag{3.34}$$

$$k_{ji}^{\mathrm{C}} = nA_{ji}(E_{\mathrm{C}}^{\mathrm{s}},E_{\mathrm{t}}) f_{ji}(E_{\mathrm{C}}^{\mathrm{s}},E_{\mathrm{t}}) \tag{3.35}$$

$$k_{ij}^{\mathrm{V}} = pA_{ij}(E_{\mathrm{V}}^{\mathrm{s}},E_{\mathrm{t}}) f_{ij}(E_{\mathrm{V}}^{\mathrm{s}},E_{\mathrm{t}}) \tag{3.36}$$

$$k_{ji}^{\mathrm{V}} = pA_{ji}(E_{\mathrm{V}}^{\mathrm{s}},E_{\mathrm{t}}) f_{ji}(E_{\mathrm{V}}^{\mathrm{s}},E_{\mathrm{t}}) \mathrm{e}^{-\beta(-E_{\mathrm{F}}+E_{\mathrm{V}}^{\mathrm{s}})}. \tag{3.37}$$

- The electronic matrix element $A_{ij}(E,E_{\mathrm{t}})$ can be approximated by the effective capture cross section $\sigma = \sigma_0\vartheta$ times the thermal velocity v_{th}, where ϑ is the tunneling factor [31, 29]. Therefore the transition rates read

$$k_{ij}^{\mathrm{C}} = nv_{\mathrm{th,n}}\sigma_{0,\mathrm{n}}\vartheta_{\mathrm{n}} f_{ij} \mathrm{e}^{-\beta(E_{\mathrm{F}}-E_{\mathrm{C}}^{\mathrm{s}})} \tag{3.38}$$

$$k_{ji}^{\mathrm{C}} = nv_{\mathrm{th,n}}\sigma_{0,\mathrm{n}}\vartheta_{\mathrm{n}} f_{ji} \tag{3.39}$$

$$k_{ij}^{\mathrm{V}} = pv_{\mathrm{th,p}}\sigma_{0,\mathrm{p}}\vartheta_{\mathrm{p}} f_{ij} \tag{3.40}$$

$$k_{ji}^{\mathrm{V}} = pv_{\mathrm{th,p}}\sigma_{0,\mathrm{p}}\vartheta_{\mathrm{p}} f_{ji} \mathrm{e}^{-\beta(-E_{\mathrm{F}}+E_{\mathrm{V}}^{\mathrm{s}})}. \tag{3.41}$$

- In the classical limit, the lineshape function f_{ij} contributes only at the intersection points of the adiabatic potential energies [29]. Thus, only the transitions at the intersection point must be considered. Assuming the system energy $V_{i,\mathrm{min}}$, the probability $P(V_{\mathrm{IP}})$, that the energy at the intersection point V_{IP} is occupied, can be derived from the Boltzmann factors and one obtains

$$\frac{P(V_{\mathrm{IP}})}{P(V_{i,\mathrm{min}})} = \frac{\mathrm{e}^{-\beta V_{\mathrm{IP}}}}{\mathrm{e}^{-\beta V_{i,\mathrm{min}}}} = \mathrm{e}^{-\beta\left(V_{\mathrm{IP}}-V_{i,\mathrm{min}}\right)}. \tag{3.42}$$

Together with the definition of the energy barrier

$$\varepsilon_{ij} = V_{\mathrm{IP}} - V_{i,\mathrm{min}} \tag{3.43}$$

the transition rates (3.38) and (3.41) can be further to

$$\begin{aligned}
k_{ij}^{\mathrm{C}} &= n v_{\mathrm{th,n}} \sigma_{0,\mathrm{n}} \vartheta_{\mathrm{n}} \mathrm{e}^{-\beta(\varepsilon_{ij}^{\mathrm{C}} + E_{\mathrm{F}} - E_{\mathrm{C}}^{\mathrm{s}})} && (3.44)\\
k_{ji}^{\mathrm{C}} &= n v_{\mathrm{th,n}} \sigma_{0,\mathrm{n}} \vartheta_{\mathrm{n}} \mathrm{e}^{-\beta\varepsilon_{ji}^{\mathrm{C}}} && (3.45)\\
k_{ij}^{\mathrm{V}} &= p v_{\mathrm{th,p}} \sigma_{0,\mathrm{p}} \vartheta_{\mathrm{p}} \mathrm{e}^{-\beta\varepsilon_{ij}^{\mathrm{V}}} && (3.46)\\
k_{ji}^{\mathrm{V}} &= p v_{\mathrm{th,p}} \sigma_{0,\mathrm{p}} \vartheta_{\mathrm{p}} \mathrm{e}^{-\beta(\varepsilon_{ji}^{\mathrm{V}} - E_{\mathrm{F}} + E_{\mathrm{V}}^{\mathrm{s}})}. && (3.47)
\end{aligned}$$

The relation between the barriers $\varepsilon_{ij}^{\mathrm{V/C}}$ and $\varepsilon_{ji}^{\mathrm{V/C}}$

$$\begin{aligned}
\varepsilon_{ij}^{\mathrm{V/C}} &= \varepsilon_{ji}^{\mathrm{V/C}} + V_{j,\mathrm{min}}^{\mathrm{V/C}} - V_{i,\mathrm{min}} && (3.48)\\
\varepsilon_{ij}^{\mathrm{V}} &= \varepsilon_{ji}^{\mathrm{V}} + \Delta E_{\mathrm{t}} = \varepsilon_{ji}^{\mathrm{V}} + E_{\mathrm{V}}^{\mathrm{s}} - E_{\mathrm{t}} && (3.49)\\
\varepsilon_{ij}^{\mathrm{C}} &= \varepsilon_{ji}^{\mathrm{C}} + \Delta E_{\mathrm{t}} + E_{\mathrm{C}}^{\mathrm{s}} - E_{\mathrm{V}}^{\mathrm{s}} = \varepsilon_{ji}^{\mathrm{C}} + E_{\mathrm{C}}^{\mathrm{s}} - E_{\mathrm{t}} && (3.50)
\end{aligned}$$

can be used to replace the barrier $\varepsilon_{ij}^{\mathrm{C}}$ and $\varepsilon_{ji}^{\mathrm{V}}$ in the rate equations, which then read

$$\begin{aligned}
k_{ij}^{\mathrm{C}} &= n v_{\mathrm{th,n}} \sigma_{0,\mathrm{n}} \vartheta_{\mathrm{n}} \mathrm{e}^{-\beta(\varepsilon_{ji}^{\mathrm{C}} + E_{\mathrm{F}} - E_{\mathrm{t}})} && (3.51)\\
k_{ji}^{\mathrm{C}} &= n v_{\mathrm{th,n}} \sigma_{0,\mathrm{n}} \vartheta_{\mathrm{n}} \mathrm{e}^{-\beta\varepsilon_{ji}^{\mathrm{C}}} && (3.52)\\
k_{ij}^{\mathrm{V}} &= p v_{\mathrm{th,p}} \sigma_{0,\mathrm{p}} \vartheta_{\mathrm{p}} \mathrm{e}^{-\beta\varepsilon_{ij}^{\mathrm{V}}} && (3.53)\\
k_{ji}^{\mathrm{V}} &= p v_{\mathrm{th,p}} \sigma_{0,\mathrm{p}} \vartheta_{\mathrm{p}} \mathrm{e}^{-\beta(\varepsilon_{ij}^{\mathrm{V}} - E_{\mathrm{F}} + E_{\mathrm{t}})}. && (3.54)
\end{aligned}$$

3.1.6 Energy Barriers

The energy barrier ε_{ij} from state i to j depends on the respective parabolas, which are given by equation (3.1). With the curvatures c_i and c_j, the energy mimima $V_{i,\mathrm{min}}$ and $V_{j,\mathrm{min}}$, and the location of the mimima along the configuration coordinate q_i and q_j, the general solution for the energy barrier reads [29]

$$\varepsilon_{ij} = \frac{c_i(q_j - q_i)^2}{\left(\frac{c_i}{c_j} - 1\right)^2} \left(1 \pm \sqrt{\frac{c_i}{c_j} + \frac{(V_{j,\mathrm{min}} - V_{i,\mathrm{min}})(\frac{c_i}{c_j} - 1)}{c_j(q_j - q_i)^2}}\right)^2. \tag{3.55}$$

If the involved parabolas have two intersection points, two energy barrier will be obtained due to the "±" sign this equation. In the following only the lower energy barrier will be considered, and therefore the solution with "+" for "±" will be dropped. The Huang-Rhys factor S_{ij} [27], the curvature relation R_{ij}, and the energy difference ΔE_{ji} between $V_{i,\mathrm{min}}$ and $V_{j,\mathrm{min}}$, are defined as

$$\begin{aligned}
S_{ij}\hbar\omega &= c_i(q_j - q_i)^2 && (3.56)\\
R_{ij}^2 &= \frac{c_i}{c_j} && (3.57)\\
\Delta E_{ji} &= V_{j,\mathrm{min}} - V_{i,\mathrm{min}}. && (3.58)
\end{aligned}$$

Using these definitions, equation (3.55) can be rewritten as

$$\varepsilon_{ij} = \frac{S_{ij}\hbar\omega}{(R_{ij}^2-1)^2}\left(1 - R_{ij}\sqrt{\frac{S_{ij}\hbar\omega + \Delta E_{ji}(R_{ij}^2-1)}{S_{ij}\hbar\omega}}\right)^2. \tag{3.59}$$

For the general case of $R_{ij} \neq 1$, there are either two intersections or none. For $R_{ij} = 1$, there is always one intersection and the energy barrier evaluates to

$$\varepsilon_{ij} = \frac{(S_{ij}\hbar\omega + \Delta E_{ji})^2}{4S_{ij}\hbar\omega}. \tag{3.60}$$

The forward barrier ε_{ij} is related to the backward barrier ε_{ji} by

$$\varepsilon_{ji} = \varepsilon_{ij} - \Delta E_{ji} \tag{3.61}$$

and the system energy of the intersection point V_{IP} can be written as

$$V_{\mathrm{IP}} = \varepsilon_{ij} + V_{i,\mathrm{min}} \tag{3.62}$$

$$= \varepsilon_{ji} + V_{j,\mathrm{min}}. \tag{3.63}$$

3.1.7 Electron-Phonon Coupling Regimes

In the following, the commonly defined electron-phonon coupling regimes [9] will be slightly extended. These extensions are of importance for later discussions, especially in Chapter 6.

The energy barrier ε_{ij} obtained by equation (3.59), is determined by R_{ij}, S_{ij}, and ΔE_{ji}. An NMP transition has a fixed value for R_{ij} and S_{ij} whereas ΔE_{ji} depends on the electric field F in the oxide via

$$\Delta E_{ji}(F) = \Delta E_{ji}(F=0) - q_0 x_{\mathrm{t}} F. \tag{3.64}$$

Thus, an increase of F corresponds to an increase of $V_{i,\mathrm{min}}$. This is shown in Figure 3.3, together with the resulting regimes, which are separable by

$$\Delta E_{ji} = S_{ij}\hbar\omega \tag{3.65}$$

and

$$\Delta E_{ji} = -\frac{S_{ij}\hbar\omega}{R_{ij}^2}. \tag{3.66}$$

The dependence of energy barriers on ΔE_{ji} is shown in Figure 3.4 for an exemplary trap. The derivative $\mathrm{d}\varepsilon_{ij}/\mathrm{d}(\Delta E_{ji})$ is also depicted in this figure, as it will be important in later discussions. Taking the derivative of equation (3.59) with respect to ΔE_{ji} yields

$$\frac{\mathrm{d}\varepsilon_{ij}}{\mathrm{d}\Delta E_{ji}} = \frac{R_{ij}^2}{-1+R_{ij}^2} - \frac{R_{ij}\sqrt{S_{ij}}}{(R_{ij}^2-1)\sqrt{S_{ij} + (R_{ij}^2-1)\Delta E_{ji}}}. \tag{3.67}$$

The substitution of equations (3.65) and (3.66) yields

$$\left.\frac{\mathrm{d}\varepsilon_{ij}}{\mathrm{d}\Delta E_{ji}}\right|_{\Delta E_{ji}=S_{ij}\hbar\omega} = \frac{R_{ij}^3-\sqrt{R_{ij}^2}}{R_{ij}(R_{ij}^2-1)} \tag{3.68}$$

$$\left.\frac{\mathrm{d}\varepsilon_{ij}}{\mathrm{d}\Delta E_{ji}}\right|_{\Delta E_{ji}=-\frac{S_{ij}\hbar\omega}{R_{ij}^2}} = \frac{R_{ij}^2-\sqrt{R_{ij}^{-2}R_{ij}^3}}{R_{ij}^2-1}. \tag{3.69}$$

For valid curvature ratios ($R_{ij}>0$), these equations read

$$\left.\frac{\mathrm{d}\varepsilon_{ij}}{\mathrm{d}\Delta E_{ji}}\right|_{\Delta E_{ji}=S_{ij}\hbar\omega} = 1 \tag{3.70}$$

$$\left.\frac{\mathrm{d}\varepsilon_{ij}}{\mathrm{d}\Delta E_{ji}}\right|_{\Delta E_{ji}=-\frac{S_{ij}\hbar\omega}{R_{ij}^2}} = 0. \tag{3.71}$$

This is in agreement with $\mathrm{d}\varepsilon_{ij}/\mathrm{d}(\Delta E_{ji})$ of the exemplary trap shown in Figure 3.4. A similar derivation of equation (3.59), but with respect to F in equation (3.64) yields

$$\left.\frac{1}{q_0x_\mathrm{t}}\frac{\mathrm{d}\varepsilon_{ij}}{\mathrm{d}F}\right|_{\Delta E_{ji}=S_{ij}\hbar\omega} = -1 \tag{3.72}$$

$$\left.\frac{1}{q_0x_\mathrm{t}}\frac{\mathrm{d}\varepsilon_{ij}}{\mathrm{d}F}\right|_{\Delta E_{ji}=-\frac{S_{ij}\hbar\omega}{R_{ij}^2}} = 0. \tag{3.73}$$

Exemplary results for this derivatives are shown in Figure 3.5. The resulting properties of the three regimes can be described as follows.

- **Strong electron-phonon coupling** is defined by

$$-\frac{S_{ij}\hbar\omega}{R_{ij}^2} < \Delta E_{ji} < S_{ij}\hbar\omega. \tag{3.74}$$

The position of the intersection point lies in between q_i and q_j. The derivatives of the energy barrier are limited by

$$0 < \frac{\mathrm{d}\varepsilon_{ij}}{\mathrm{d}E_{ji}} < 1 \tag{3.75}$$

$$-1 < \frac{1}{q_0x_\mathrm{t}}\frac{\mathrm{d}\varepsilon_{ij}}{\mathrm{d}F} < 0. \tag{3.76}$$

The increase of ε_{ij} is always positive and smaller than the increase of E_{ji}. With regard to F, the increase of ε_{ij} is always negative and smaller than the increase of $q_0x_\mathrm{t}F$.

- **Positive weak electron-phonon coupling** is defined by

$$\Delta E_{ji} > S_{ij}\hbar\omega. \tag{3.77}$$

The system energy V_i is smaller than V_j and $q_{\mathrm{IP}} < q_i < q_j$ holds. The derivatives of the energy barrier are limited by

$$\frac{\mathrm{d}\varepsilon_{ij}}{\mathrm{d}E_{ji}} > 1 \tag{3.78}$$

$$\frac{1}{q_0 x_\mathrm{t}}\frac{\mathrm{d}\varepsilon_{ij}}{\mathrm{d}F} < -1. \tag{3.79}$$

The increase of ε_{ij} is always positive and larger than the increase of E_{ji}. With regard to F, the increase of ε_{ij} is always negative and larger than the increase of $-q_0 x_\mathrm{t} F$.

- **Negative weak electron-phonon coupling** is defined by

$$\Delta E_{ji} < -\frac{S_{ij}\hbar\omega}{R_{ij}^2}. \tag{3.80}$$

The system energy V_i is larger than V_j and $q_i < q_j < q_{\mathrm{IP}}$ holds. The derivatives of the energy barrier are limited by

$$\frac{\mathrm{d}\varepsilon_{ij}}{\mathrm{d}E_{ji}} < 0 \tag{3.81}$$

$$\frac{1}{q_0 x_\mathrm{t}}\frac{\mathrm{d}\varepsilon_{ij}}{\mathrm{d}F} > 0. \tag{3.82}$$

In this regime, the signs change, compared to the other two regimes, and ε_{ij} decreases for increasing E_{ji} and for decreasing F.

3.2 Pure Thermal Barriers

As discussed in Chapter 2, measurements of BTI defects indicated the existence of metastable states. These metastable states allow for transitions without a macroscopic charge exchange. As the corresponding transition rates are temperature activated, these transitions are termed "pure thermal barriers". They can be modeled according to the transition state theory [32] with two states i and j, both in the same charge state. The mimima $V_{i,\mathrm{min}}$ and $V_{j,\mathrm{min}}$ of these states are separated by the barriers ε_{ij} and ε_{ij}, as depicted in Figure 3.6. These energy barriers corresponds to an activation energy in a Arrhenius equation and therefore, the resulting rates depend on the temperature only. With the attempt frequency ν_0, the transition rates can be written as

$$k_{ij} = \nu_0 e^{-\beta\varepsilon_{ij}} k_{ji} = \nu_0 e^{-\beta\varepsilon_{ji}}. \tag{3.83}$$

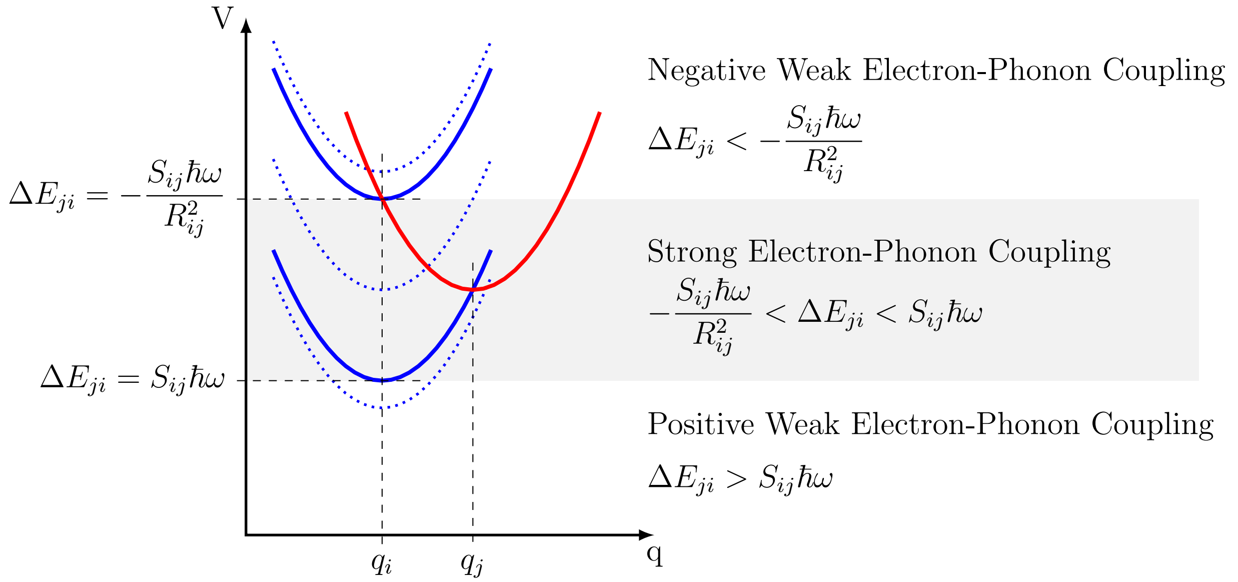

Figure 3.3: Configuration coordinate diagrams for two charge states. The system energy $V_{i,\min}$ increases with the electric field F in the oxide. The resulting ΔE_{ji} defines the regime of the transition. The solid blue lines indicate the limit between the regimes as described in Section 3.1.7. The dotted lines are exemplary configurations in the respective regimes.

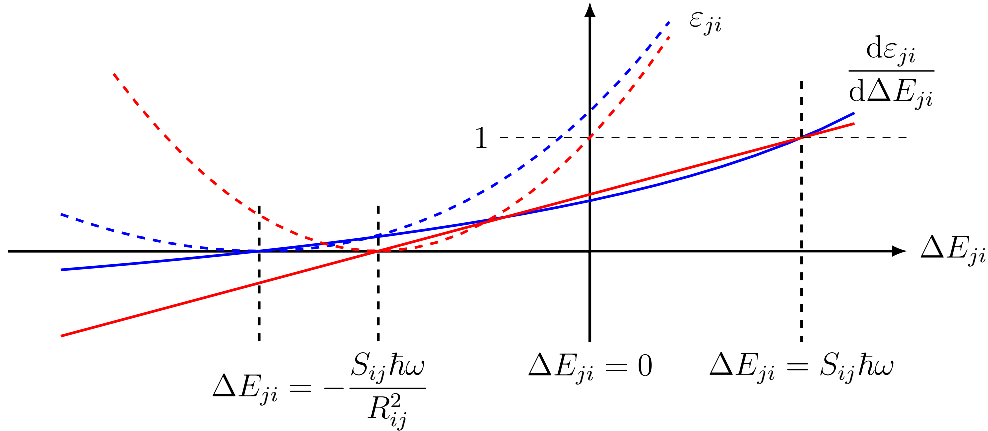

Figure 3.4: The height of the energy barriers ε_{ij} (dashed lines) and their derivatives with respect to ΔE_{ji} (solid lines) for $R_{ij} = 1$ (red) and $R_{ij} = 0.8$ (blue), both with $S_{ij}\hbar\omega = 4\,\mathrm{eV}$.

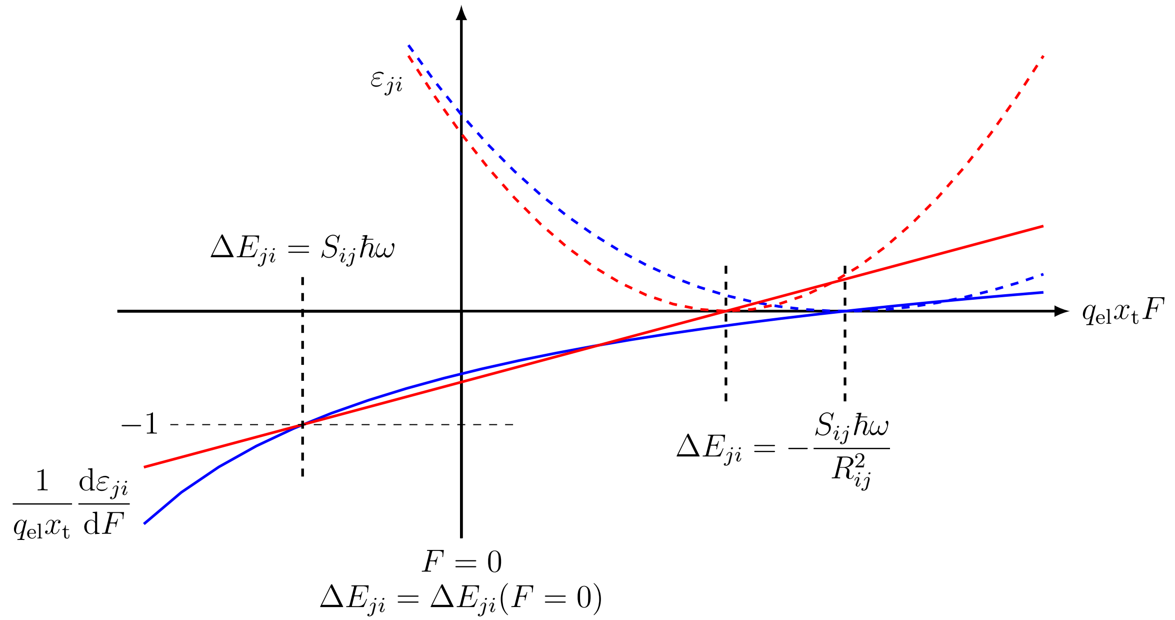

Figure 3.5: The height of the energy barriers ε_{ij} (dashed lines) and their derivatives with respect to F (solid lines) for $R_{ij} = 1$ (red) and $R_{ij} = 0.8$ (blue), both with $S_{ij}\hbar\omega = 4\,\mathrm{eV}$ and $E_{ji}(F = 0) = 1\,\mathrm{eV}$.

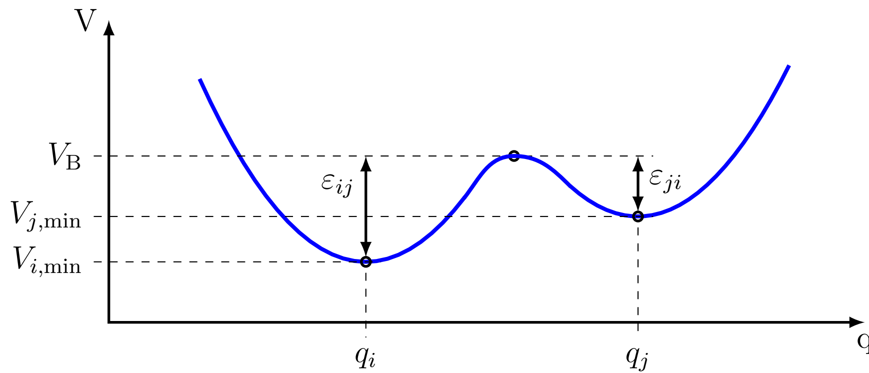

Figure 3.6: Schematic configuration coordinate diagram of a pure thermal transition with states i and j, and the respective thermal barriers ε_{ij} and ε_{ij}.

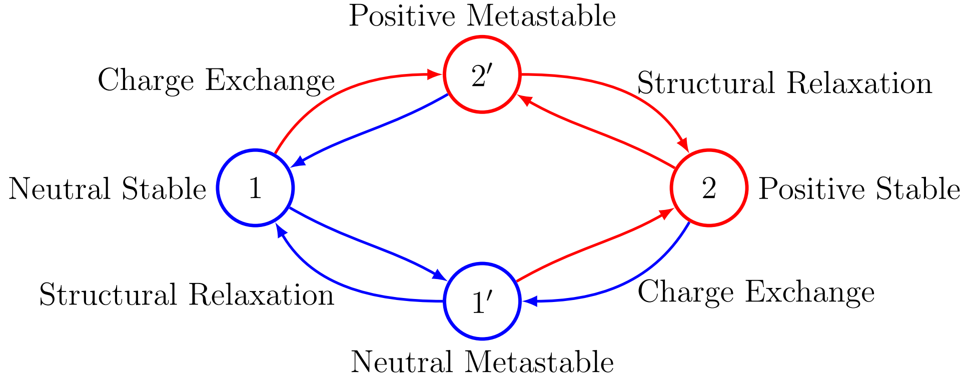

Figure 3.7: Full state diagram of the NMP four state model. If the system is in stable state 1 or in the metastable state 1′ the trap is neutral, and for the stable state 2 and the metastable state 2′ the trap is positively charged. Transitions, which involve charge exchange, are modeled as NMP transitions, and structural relaxations are described by pure thermal transitions.

3.3 NMP Four State Model

The NMP four state model [9] comprises four states with two NMP transitions and two pure thermal transitions. This model can describe the charging and the discharging of oxide defects, which contribute to the recoverable component of BTI. In the following, the main concept of the model will be explained.

3.3.1 States and Definitions

The NMP four state model is based on a neutral state 1 and a positively charged state 2. For each of these charge states an additional metastable state is considered. The existence of these metastable states was indicated by TDDS measurements [31]. Transitions involving a charge exchange between oxide defects and the semiconductor are considered as NMP transitions, whereas transitions without a charge exchange are modeled as pure thermal transitions. The four states and the corresponding transitions are depicted in Figure 3.7 and the configuration coordinate diagram of the NMP four state model is shown in Figure 3.8. In the latter, the energies V_1, V_2^{V} and V_2^{C} are shown, which correspond to the energy mimima $V_{i,\mathrm{min}}$, $V_{j,\mathrm{min}}^{\mathrm{V}}$ and $V_{j,\mathrm{min}}^{\mathrm{C}}$, introduced in Section 3.1.2. The energy V_1' can be linked to $V_{i,\mathrm{min}}$ as well, but its trap energy will be labeled $E_{\mathrm{t}'}$, as it differs from the trap level E_{t} which is associated with V_1. The energy levels $V_{2'}^{\mathrm{V}}$ and $V_{2'}^{\mathrm{C}}$ are defined by the energy difference $\varepsilon_{\mathrm{T2'}}$ between state 2 with the relations

$$\begin{aligned}\varepsilon_{\mathrm{T2'}} &= V_{2'}^{\mathrm{V}} - V_2^{\mathrm{V}} \\ &= V_{2'}^{\mathrm{C}} - V_2^{\mathrm{C}}.\end{aligned} \tag{3.84}$$

The value of $\varepsilon_{\mathrm{T2'}}$ must be larger than 0 eV, and V_1' must be larger than V_1, in order to ensure the metastable nature of state 1′ and 2′.

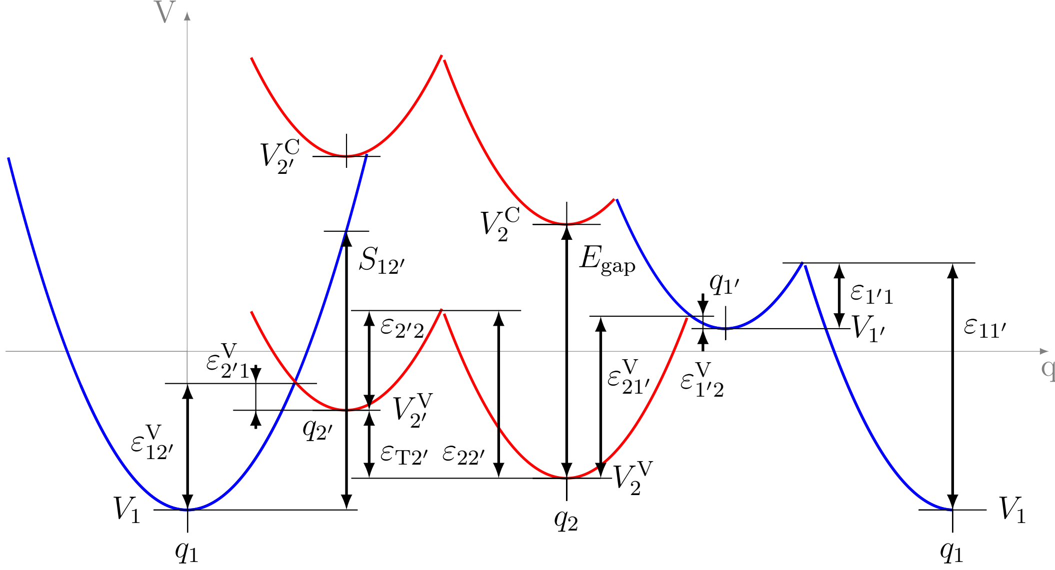

Figure 3.8: Schematic configuration coordinate diagram showing all states of the NMP four state model, including valence and conduction band transitions. For the valence band case, all important barriers and energy levels are shown.

3.3.2 Transition Rates

As shown in Figure 3.7, there are two NMP transitions per energy band. Additionally, there are two transitions governed by the height of pure thermal barriers. Using the rate equations (3.44) to (3.47) and (3.83) derived in sections 3.1.5 and 3.2 and the barriers shown in Figure 3.8, the full set of transition rates reads

$$
\begin{aligned}
k_{12'} &= k_{12'}^{\mathrm{C}} + k_{12'}^{\mathrm{V}} \\
&= n v_{\mathrm{th,n}} \sigma_{0,\mathrm{n}} \vartheta_{\mathrm{n}} \mathrm{e}^{-\beta(\varepsilon_{12'}^{\mathrm{C}} - E_{\mathrm{C}}^{\mathrm{s}} + E_{\mathrm{f}})} + p v_{\mathrm{th,p}} \sigma_{0,\mathrm{p}} \vartheta_{\mathrm{p}} \mathrm{e}^{-\beta \varepsilon_{12'}^{\mathrm{V}}} \qquad (3.85)\\
k_{2'1} &= k_{2'1}^{\mathrm{C}} + k_{2'1}^{\mathrm{V}} \\
&= n v_{\mathrm{th,n}} \sigma_{0,\mathrm{n}} \vartheta_{\mathrm{n}} \mathrm{e}^{-\beta \varepsilon_{2'1}^{\mathrm{C}}} + p v_{\mathrm{th,p}} \sigma_{0,\mathrm{p}} \vartheta_{\mathrm{p}} \mathrm{e}^{-\beta(\varepsilon_{2'1}^{\mathrm{V}} + E_{\mathrm{V}}^{\mathrm{s}} - E_{\mathrm{f}})} \qquad (3.86)\\
k_{21'} &= k_{21'}^{\mathrm{C}} + k_{21'}^{\mathrm{V}} \\
&= n v_{\mathrm{th,n}} \sigma_{0,\mathrm{n}} \vartheta_{\mathrm{n}} \mathrm{e}^{-\beta \varepsilon_{21'}^{\mathrm{C}}} + p v_{\mathrm{th,p}} \sigma_{0,\mathrm{p}} \vartheta_{\mathrm{p}} \mathrm{e}^{-\beta(\varepsilon_{21'}^{\mathrm{V}} + E_{\mathrm{V}}^{\mathrm{s}} - E_{\mathrm{f}})} \qquad (3.87)\\
k_{1'2} &= k_{1'2}^{\mathrm{C}} + k_{1'2}^{\mathrm{V}} \\
&= n v_{\mathrm{th,n}} \sigma_{0,\mathrm{n}} \vartheta_{\mathrm{n}} \mathrm{e}^{-\beta(\varepsilon_{1'2}^{\mathrm{C}} - E_{\mathrm{C}}^{\mathrm{s}} + E_{\mathrm{f}})} + p v_{\mathrm{th,p}} \sigma_{0,\mathrm{p}} \vartheta_{\mathrm{p}} \mathrm{e}^{-\beta \varepsilon_{1'2}^{\mathrm{V}}} \qquad (3.88)\\
k_{11'} &= \nu_0 e^{-\beta \varepsilon_{11'}} \qquad (3.89)\\
k_{1'1} &= \nu_0 e^{-\beta \varepsilon_{1'1}} \qquad (3.90)\\
k_{22'} &= \nu_0 e^{-\beta \varepsilon_{22'}} \qquad (3.91)\\
k_{2'2} &= \nu_0 e^{-\beta \varepsilon_{2'2}}. \qquad (3.92)
\end{aligned}
$$

3.3.3 Occupation Probabilities and Charges

A system with a single defect as introduced in Section 3.1.1 is in either state at any time. As a consequence, the occupation $X_\mathrm{i}(t)$ of the state i is equal to one, if the system is in state i or zero if it is in another state. The sum of the occupations reads

$$X_\mathrm{i}(t) + X_\mathrm{j}(t) = 1. \tag{3.93}$$

If the expectation value of the occupation of the single defect system is of interest, or if a multitude of defects, and therefore of this system, are considered, only the probability $P\{X_i(t) = 1\}$ is relevant. As we consider a memoryless system, that means $P\{X_i(t+h)\}$ at the time $t+h$ only depends on the information at time t, transitions can be described by first-order Markov chains [33]. Given $P\{X_i(t) = 1\}$, the probability of a transition to state j within the time $t + h$ depends on the transition rate k_{ij} [9].

$$P\{X_j(t + h) = 1|X_i(t) = 1\} = k_{ij}h + O(h). \tag{3.94}$$

For an infinitesimal time interval h and with the shorthand $p_i(t) = P\{X_i(t) = 1\}$ together with the rates (3.85) to (3.92), the set of differential equations for the time dependent occupation probabilities p_i of state i can be written as

$$\frac{\mathrm{d}p_1(t)}{\mathrm{d}t} = k_{1'1}p_{1'}(t) + k_{2'1}p_{2'}(t) - k_{11'}p_1(t) - k_{12'}p_1(t) \tag{3.95}$$

$$\frac{\mathrm{d}p_{1'}(t)}{\mathrm{d}t} = k_{11'}p_1(t) + k_{21'}p_2(t) - k_{1'1}p_{1'}(t) - k_{1'2}p_{1'}(t) \tag{3.96}$$

$$\frac{\mathrm{d}p_2(t)}{\mathrm{d}t} = k_{2'2}p_{2'}(t) + k_{1'2}p_{1'}(t) - k_{22'}p_2(t) - k_{21'}p_2(t) \tag{3.97}$$

$$\frac{\mathrm{d}p_{2'}(t)}{\mathrm{d}t} = k_{12'}p_1(t) + k_{22'}p_2(t) - k_{2'1}p_{2'}(t) - k_{2'2}p_{2'}(t). \tag{3.98}$$

Still the sum of all occupations has to be one at any time, so

$$p_1(t) + p_{1'}(t) + p_2(t) + p_{2'}(t) = 1. \tag{3.99}$$

For the equilibrium solution of the occupation probabilities with $t \to \infty$, the time derivatives $\mathrm{d}p_i(t)/\mathrm{d}t$ are set to zero. As the analytical solution gives lengthy expressions, it is not given here. The master equation, which describe the occupation probabilities as a function of time, can be obtained solving the same equation system without setting $\mathrm{d}p_i(t)/\mathrm{d}t$ to zero.

With regard to the charge of a trap, only the positive states 2 and $2'$ have to be considered. Following the concept of occupation probabilities, the charge q_t of a trap in the NMP four state model, can be defined as

$$q_\mathrm{NMP} = q_0(p_2 + p_{2'}). \tag{3.100}$$

3.3.4 Capture and Emission Times

Provided a system is in state i at a given time t_0, a transition to state j will occur after the first passage time τ_{ij} [9]. This time does not depend on the rate k_{ji}, as the system was not in the state j for $t_0 \leq t < t_0 + \tau_{ij}$. As the first passage times are stochastic quantities, the expectation value $\overline{\tau}_{ij}$ of τ_{ij} can be defined. The terms “capture” and “emission” refer to the trap behavior. For donor-like traps with a positive state j and a neutral state i, the capture time constant τ_c and the emission time constant τ_e are defined as

$$\tau_\mathrm{c} = \overline{\tau}_{ij} \tag{3.101}$$

$$\tau_\mathrm{e} = \overline{\tau}_{ji}. \tag{3.102}$$

The capture and emission time constants of a system with two states are the inverse of the corresponding rates, but for the NMP four state model, the rates of the metastable states have to be considered as well. As the positive state was denoted by “2” and the neutral state by “1”, the time constants are defined as

$$\tau_\mathrm{c} = \tau_{12} \tag{3.103}$$

$$\tau_\mathrm{e} = \tau_{21}. \tag{3.104}$$

Transitions between the stable states 1 and 2 are only possible via the metastable states $1'$ and $2'$ (compare Figure 3.7). Both transition paths can be assumed as an isolated three state chain and corresponding partial time constants can be approximated by [9]

$$\tau_\mathrm{c}{}^{1'} = \frac{k_{11'} + k_{1'1} + k_{1'2}}{k_{11'}k_{1'2}} \tag{3.105}$$

$$\tau_\mathrm{c}{}^{2'} = \frac{k_{12'} + k_{2'1} + k_{2'2}}{k_{12'}k_{2'2}} \tag{3.106}$$

$$\tau_\mathrm{e}{}^{1'} = \frac{k_{1'1} + k_{1'2} + k_{21'}}{k_{1'1}k_{21'}} \tag{3.107}$$

$$\tau_\mathrm{e}{}^{2'} = \frac{k_{2'1} + k_{2'2} + k_{22'}}{k_{2'1}k_{22'}}. \tag{3.108}$$

The overall capture and emission time constants are [9]

$$\tau_\mathrm{c} = \frac{1}{\dfrac{1}{\tau_\mathrm{c}{}^{1'}} + \dfrac{1}{\tau_\mathrm{c}{}^{2'}}} \tag{3.109}$$

$$\tau_\mathrm{e} = \frac{1}{\dfrac{1}{\tau_\mathrm{e}{}^{1'}} + \dfrac{1}{\tau_\mathrm{e}{}^{2'}}}. \tag{3.110}$$

3.4 Double Well Model

As the NMP four state model describes only the recoverable component of the BTI degradation, another model for the permanent component is necessary (compare Section 2.1). The details of the process which causes the permanent component, is not identified yet. A model whose results showed good agreement with measurements for different gate voltages and temperatures, is based on a double well [34] and will be described in the following.

3.4.1 Configuration Coordinate Diagram

The double well model [34] has a neutral state "A" and a positively charged state "B" with the system energies V_{A} and V_{B}, respectively. In the case of a $P_{\mathrm{b}}H$ defect, which is a likely defect candidate for permanent traps, the neutral state A would represent a interface silicon atom, saturated by a hydrogen. If the hydrogen atom moves away, it causes a dangling bond at the silicon atom (P_{b} center), whose trap level is occupied according to the Fermi level in the substrate. This atomic configuration can be associated with the positive state B in the double well model. Independent of the actual microscopic defect, the energies V_{B} and V_{AB}, shown in the configuration coordinate diagram in Figure 3.9, are assumed to be bias dependent proportional to the electric field F in the oxide. With the factor γ, which phenomenologically describes the bias dependence, and $V_{\mathrm{A}} = V_{\mathrm{ref}} = 0$, the energies in the configuration coordinate diagram can be expressed as

$$V_{\mathrm{A}}(F) = 0 \tag{3.111}$$

$$V_{\mathrm{B}}(F) = V_{\mathrm{B}}(F=0) - 2\gamma F \tag{3.112}$$

$$V_{\mathrm{AB}}(F) = V_{\mathrm{AB}}(F=0) - \gamma F. \tag{3.113}$$

The resulting barriers reads

$$\varepsilon_{\mathrm{AB}} = V_{\mathrm{AB}} - V_{\mathrm{A}} = V_{\mathrm{AB}}(F=0) - \gamma F \tag{3.114}$$

$$\varepsilon_{\mathrm{BA}} = V_{\mathrm{AB}} - V_{\mathrm{B}} = V_{\mathrm{AB}}(F=0) - V_{\mathrm{B}}(F=0) + \gamma F. \tag{3.115}$$

As depicted in Figure 3.9, an increasing electric field F in the oxide lowers the energy barrier $\varepsilon_{\mathrm{AB}}$ and increases the barrier $\varepsilon_{\mathrm{BA}}$.

3.4.2 Rates and Occupation Probabilities

The double well rates are similar to the rates of transitions via pure thermal barriers, but the bias dependence has to be considered as well. With the barriers in the equations (3.114) and (3.115) and the attempt frequency ν_0, the rates read

$$k_{\mathrm{AB}} = \nu_0 \mathrm{e}^{-\beta\varepsilon_{\mathrm{AB}}} \tag{3.116}$$

$$k_{\mathrm{BA}} = \nu_0 \mathrm{e}^{-\beta\varepsilon_{\mathrm{BA}}}. \tag{3.117}$$

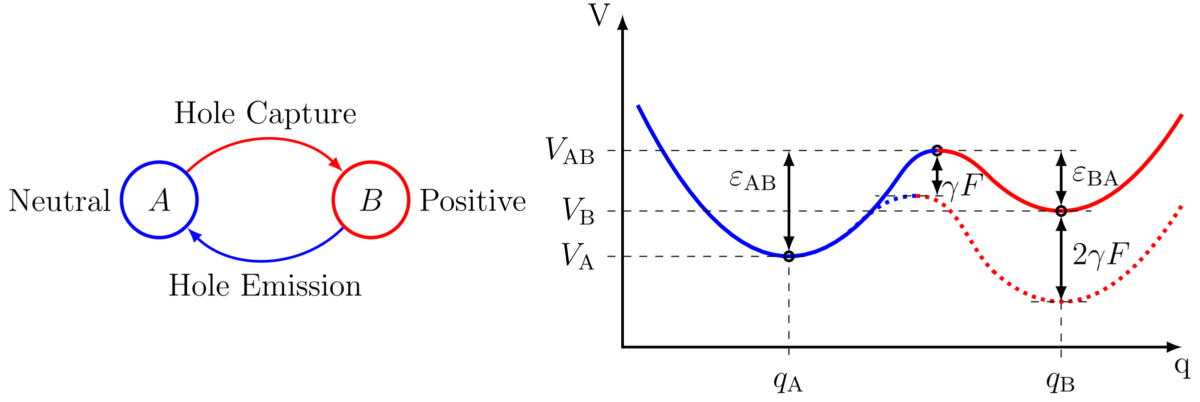

Figure 3.9: **Left**: State diagram of the double well model with the neutral state A and the positive state B. **Right**: The corresponding schematic configuration coordinate diagram at high (dotted line) and low (solid line) gate bias. A high gate bias is associated with a higher electric field F, which results in an decrease of the energy barrier ε_{AB} and increases the barrier ε_{BA}.

As shown in Section 3.3.3, the differential equations of the occupation probabilities p_A and p_B are

$$\frac{dp_A(t)}{dt} = k_{BA}p_B(t) - k_{AB}p_A(t) \tag{3.118}$$

$$\frac{dp_B(t)}{dt} = k_{AB}p_A(t) - k_{BA}p_B(t). \tag{3.119}$$

Setting the time derivatives $dp_i(t)/dt$ to zero, the equilibrium occupation probabilities evaluate to

$$p_A = \frac{k_{BA}}{k_{BA} + k_{AB}} \tag{3.120}$$

$$p_B = \frac{k_{AB}}{k_{BA} + k_{AB}}. \tag{3.121}$$

The solution for the occupation probabilities using the implicit Euler scheme with a time step h is given by

$$p_A(t+h) = \frac{k_{BA}h + p_A(t)}{1 + k_{AB}h + k_{BA}h} \tag{3.122}$$

$$p_B(t+h) = \frac{k_{AB}h + p_B(t)}{1 + k_{BA}h + k_{BA}h}. \tag{3.123}$$

These equations can be used to iteratively calculate the time evolutions of the double well model.

3.4.3 Charge and Time Constants

The double well model describes donor-like traps. The occupation probability p_{B} of the positive state B, given by equation (3.121) and (3.123), results in the charge q_{DW} of a double well trap as

$$q_{\mathrm{DW}} = q_0 p_{\mathrm{B}} f_{\mathrm{p}}(E_{\mathrm{t,DW}}) \tag{3.124}$$

with $E_{\mathrm{t,DW}}$ being the trap level of defect in state B. The obtained charge affects the channel region and thereby, contributes to BTI. The time constants τ_{c} and τ_{e} of the double well model are related to the rates via the equations

$$\tau_{\mathrm{c}} = \frac{1}{k_{\mathrm{AB}}} \tag{3.125}$$

$$\tau_{\mathrm{e}} = \frac{1}{k_{\mathrm{BA}}}. \tag{3.126}$$

In order to describe the permanent component of BTI with a large emission time constant, the parameters $V_{\mathrm{B}}(F=0)$, $V_{\mathrm{AB}}(F=0)$ and γ have to be chosen accordingly.

CHAPTER 4 Single Trap Simulation

Using TDDS, described in Section 2.2.3, the capture (τ_c) and emission (τ_e) time constants of single traps are accessible at different temperatures and gate voltages. Based on such measurement data the parameters of the NMP four state model will be extracted for two trap types. The corresponding simulation setup, the parameter optimization, and the obtained results will be discussed in this chapter.

4.1 Measurement Data

In Figure 4.1 the experimental results for two traps measured on small-area pMOSFET devices [2] are shown. The capture as well as the emission time constants of the traps are found to be temperature-activated. Furthermore, a curvature in the capture time constants can be observed in the logarithmic plot of Figure 4.1. This curvature can be mathematically described by relation [9]

$$\tau_e \approx \tau_0 e^{c_1 F + c_2 F^2} \tag{4.1}$$

where τ_0, c_1 and c_2 are constants. On the basis of the emission behavior, two types of traps can be distinguished:

- Switching traps: Their emission time constants show a drop at the relaxation voltage.
- Fixed positive charge traps: Their emission time constant is nearly bias independent within the range around and above the relaxation voltage.

The parameters of the NMP four state model have been extracted for the two trap types. The details of the extraction method will be given in Section 4.2. The extraction was carried out for the TDDS data, including two different temperatures (125°C, 175°C) for each trap. The emission time constants were measured in a gate voltage range of -0.2 to -1 V and the capture time constants were determined in the range between -0.7 and -2.5 V.

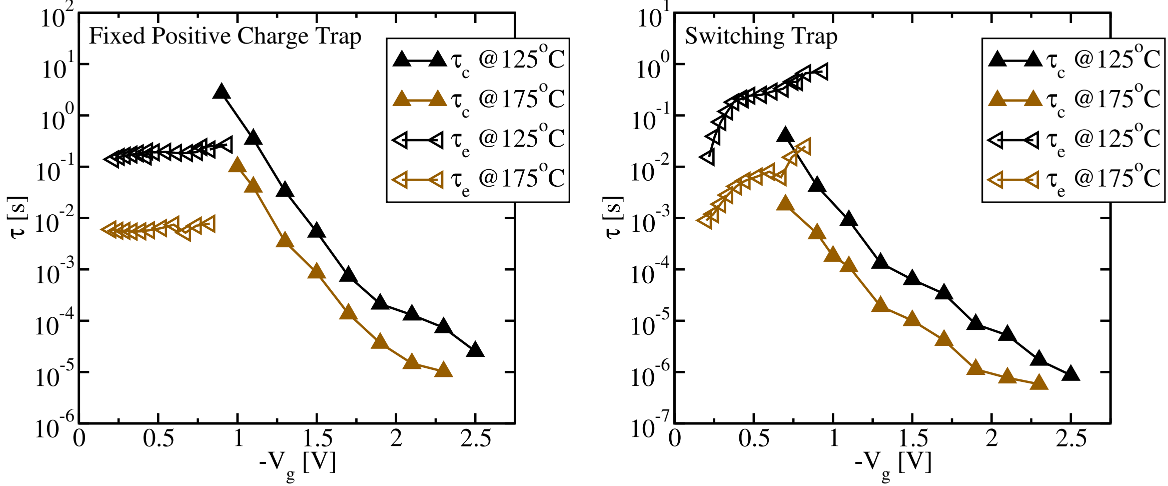

Figure 4.1: TDDS data of a fixed positive charge trap (left) and a switching trap (right) for $T = 125°\text{C}$ and $T = 175°\text{C}$ [31].

4.2 Simulation Setup

For each trap type, an optimizer was used to match the simulated time constants to the TDDS data. Thereby, the parameters of the NMP four state model were extracted for two exemplary traps. In this section the corresponding simulation setup will be described.

4.2.1 Device Generation

A device geometry for subsequent simulations was created using the device editor GTS Structure [35] of Global TCAD Solutions. The measured device is represented by a two-dimensional pMOSFET with a gate length (l) of 250 nm and an oxide thickness (t_{ox}) of 2.574 nm. The donor ($N_{\text{D,bulk}}$) and acceptor ($N_{\text{A,bulk}}$) concentration of the substrate and the workfunction difference (ΔE_{W}) between the metal gate and the substrate are $6 \times 10^{17}\,\text{cm}^{-3}$, $4 \times 10^{5}\,\text{cm}^{-3}$, and $-0.2\,\text{eV}$, respectively. The acceptor concentration in the source and drain segment ($N_{\text{A,S/D}} = 2 \times 10^{20}\,\text{cm}^{-3}$) should not affect the traps in the middle of the channel for sufficiently long gate lengths. The mesh of the device was chosen orthogonal with refinements in the channel region.

4.2.2 Device Simulation

The device simulator Minimos-NT [36] of Global TCAD Solutions was used to solve the Poisson and drift-diffusion equations, which are coupled by the quantities n, p and ψ. The quantities n, p, ψ, E_{C} and E_{V} are needed to evaluate the capture and emission time constants of the NMP four state model (compare Section 3.3.2). The carrier transport was simulated within the drift-diffusion model and Boltzmann statistics were considered. As a result, the rates (3.85) to (3.92) based on Boltzmann statistics must be used in

Parameter	Description
x_t	Trap distance from the interface
y_t	Trap position along the channel direction
E_t	Trap level of the stable state 1
$E_{\mathrm{t}'}$	Trap level of the metastable state 1′
$\varepsilon_{\mathrm{T}2'}$	Energy difference between states 2 and 2′
$R_{12'}$	Curvature ratio between states 1 and 2′
$S_{12'}\hbar\omega$	Huang-Rhys factor times $\hbar\omega$ between states 1 and 2′
$R_{1'2}$	Curvature ratio between states 1′ and 2
$S_{1'2}\hbar\omega$	Huang-Rhys factor times $\hbar\omega$ between states 1′ and 2
$\varepsilon_{1'1}$	Barrier from state 1′ to 1
$\varepsilon_{2'2}$	Barrier from state 2′ to 2
σ_0	Capture cross section

Table 4.1: Parameters of an NMP four state trap.

the simulation. The bulk and source voltages were set to $V_{\mathrm{B/S}} = 0\,\mathrm{V}$ and a small drain voltage V_D of $50\,\mathrm{mV}$ was applied. The gate voltage was stepped within the gate voltage range applied in the TDDS measurements. These simulations were done for the two temperatures chosen in the measurements. Steady state simulations were carried out as the time constants τ_c and τ_e are time independent.

4.2.3 NMP Four State Model

A single trap was added to the oxide segment. Its time constants τ_c and τ_e were obtained using the expressions (3.109) and (3.110), which were implemented in Minimos-NT [36, 37]. The trap parameters of the NMP four state model are listed in Table 4.1. For a low drain voltage the time constants are nearly independent of the trap position along the channel direction y_t. Therefore y_t was set to the value of the middle of the gate segment and neglected in the optimization.

4.2.4 Parameter Optimization

The optimization of the parameter set of the NMP four state model (compare Section 4.2.3) was done with the optimizer tool of Global TCAD Solutions [38]. The flowchart of the optimization scheme is shown in Figure 4.2 and is described below. First, a reasonable initial guess $S_\mathrm{init} = \{P_1, P_2, ...P_N\}$ for the N trap parameters $P_1, P_2, ...P_N$ was assumed. A simulation based on these parameters with the simulation setup as explained above, yielded simulation values of the time constants $\tau_\mathrm{c}(V_\mathrm{G}, T)$ and $\tau_\mathrm{e}(V_\mathrm{G}, T)$. Together with the time constants of the measurement data $\tau_\mathrm{c,real}(V_\mathrm{G}, T)$ and $\tau_\mathrm{e,real}(V_\mathrm{G}, T)$ for K

gate voltages and M temperatures a score τ_s was calculated as

$$\tau_\mathrm{s} = \tau_\mathrm{s}^{\tau_\mathrm{c}} + \tau_\mathrm{s}^{\tau_\mathrm{e}} \quad (4.2)$$

$$\tau_\mathrm{s}^{\tau_\mathrm{c}} = \sum_{n=1}^{K}\sum_{m=1}^{M} \left|\log\big(\tau_\mathrm{c,real}(V_{\mathrm{G},n},T_m)\big) - \log\big(\tau_\mathrm{c}(V_{\mathrm{G},n},T_m)\big)\right| \quad (4.3)$$

$$\tau_\mathrm{s}^{\tau_\mathrm{e}} = \sum_{n=1}^{K}\sum_{m=1}^{M} \left|\log\big(\tau_\mathrm{e,real}(V_{\mathrm{G},n},T_m)\big) - \log\big(\tau_\mathrm{e}(V_{\mathrm{G},n},T_m)\big)\right|. \quad (4.4)$$

If the score value was too large, the optimizer created N new sets of parameters $S_1, S_2, ...S_N$. In each set S_i one parameter P_i was varied by adding a small value ΔP_i, while the other parameters remained the same.

$$S_i = \{P_1, P_2, ..., P_{i-1}, P_i + \Delta P_i, P_{i+1}, ..., P_N\},\ i\epsilon\{1, 2, ...N\} \quad (4.5)$$

For each of these parameter sets, a simulation was carried out and a score was calculated in the same way as for the initial guess. Based on the resulting N score values $\tau_{\mathrm{s},1}, \tau_{\mathrm{s},2}, ...\tau_{\mathrm{s},N}$, a constrained nonlinear optimization algorithm [39] determined a new set of parameters S_new which is expected to yield an improved score value. A new iteration was started by continuing with this set of parameters S_new and calculating the new time constants $\tau_\mathrm{c}(V_\mathrm{G}, T)$ and $\tau_\mathrm{e}(V_\mathrm{G}, T)$. Usually, the progress of the score and of the corresponding simulation results is monitored during the optimization. Optimizations with undesired trends can be avoided with a correction of the parameter constraints.

4.3 Results

4.3.1 Fixed Positive Charge Trap

A trap whose emission time constant is nearly bias independent within the range around and above the relaxation voltage, is termed "fixed positive charge trap". As transitions of fixed positive charge traps between the states 1 and 2 are assumed to be governed by transitions via the metastable state $2'$, only the parameters which correspond to this transition path were optimized. Using the setup described in Section 4.2, this optimization yielded the parameters as listed in Table 4.2. The corresponding time constants are shown in Figure 4.3. These time constants are mainly governed by transitions between the valence band and the oxide trap because the electron concentration in the conduction band is too low for the given gate voltage range. The configuration coordinate diagram in Figure 4.4 shows the relevant transition path via the metastable state $2'$. At this path the bias dependent barrier $\varepsilon_{2'1}$ is small compared to the bias independent barrier $\varepsilon_{22'}$. This results in a bias independent emission time constant, as expected for a fixed positive charge trap.

4.3.2 Switching Trap

A trap which emission time constant shows a drop at the relaxation voltage, is termed "switching trap". The optimization of a switching trap, using the setup described in Sec-

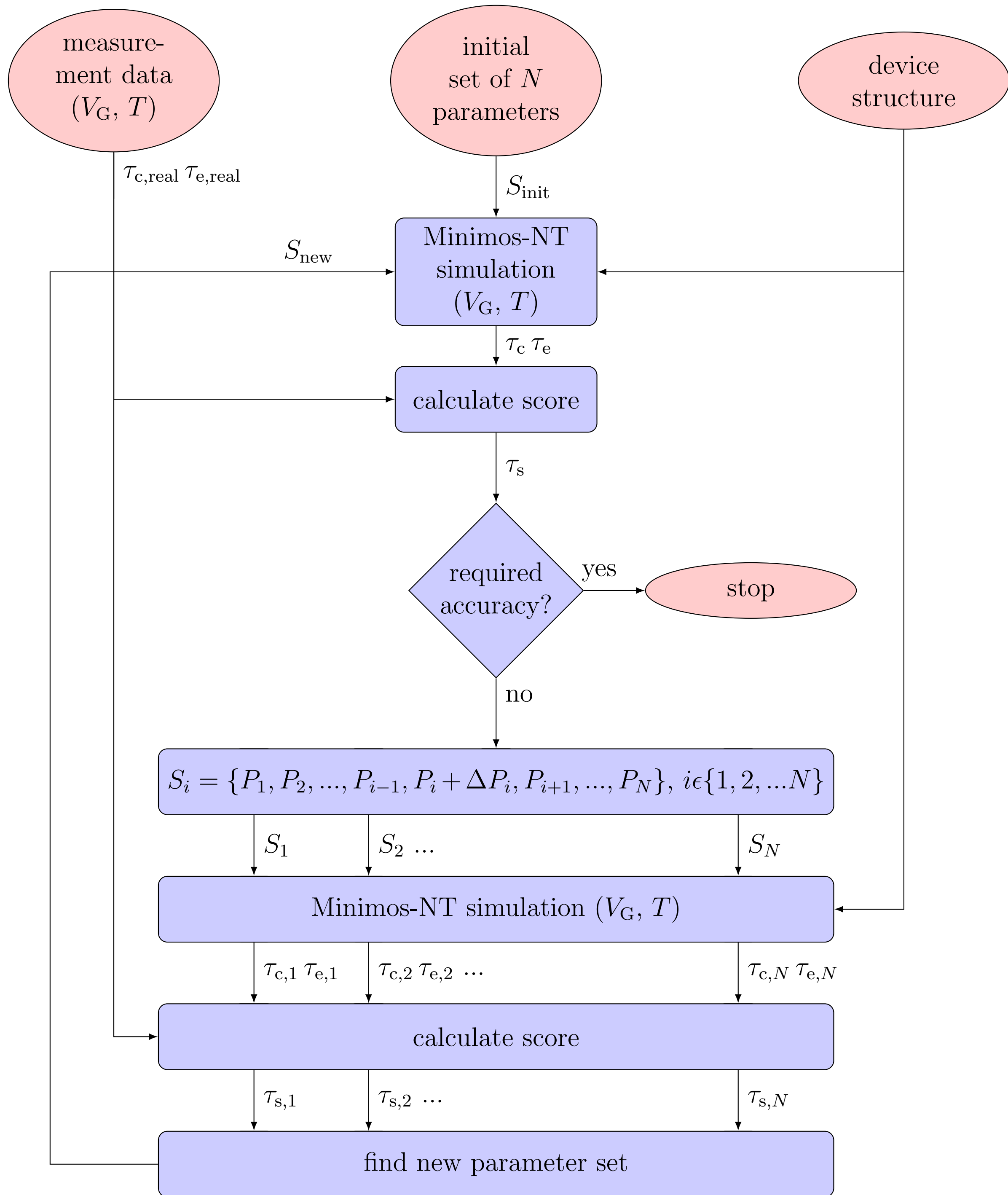

Figure 4.2: Optimization scheme as described in Section 4.2.4.

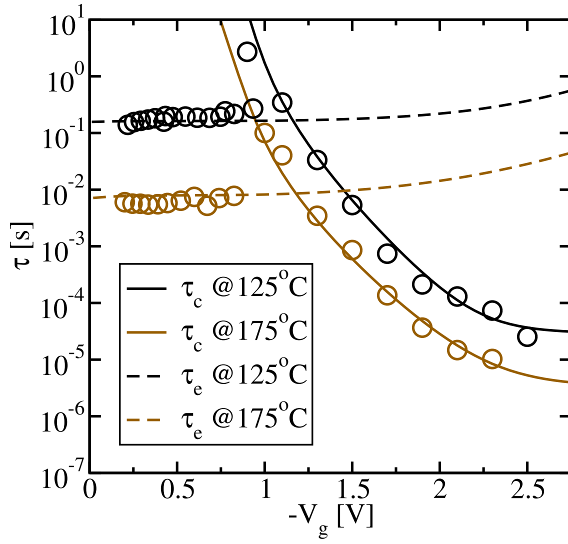

Figure 4.3: Result of the parameter optimization of a fixed positive charge trap. Measurement data is indicated with circles, the lines represent simulation results.

Parameter	Value	Unit
x_t	0.3	nm
E_t	-0.607	eV
$\varepsilon_{\mathrm{T}2'}$	0.294	eV
$R_{12'}$	1.363	1
$S_{12'}\hbar\omega$	1.9	eV
$\varepsilon_{2'2}$	0.668	eV
σ_0	10^{-15}	cm^2

Table 4.2: NMP four state parameters of the fixed positive charge trap.

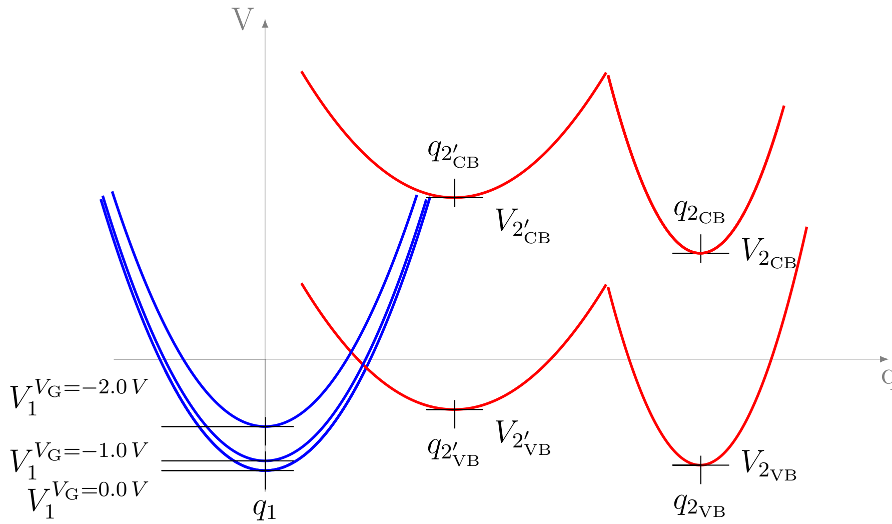

Figure 4.4: Configuration coordinate diagram of the fixed positive charge trap. The configuration is plotted for three different gate voltages to show the bias dependence of τ_e.

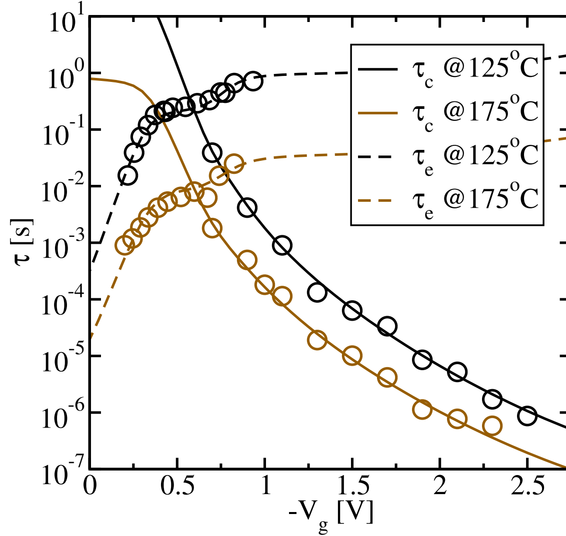

Figure 4.5: Result of the parameter optimization of a switching trap. Measurement data is indicated with circles, the lines represent simulation results.

Parameter	Value	Unit
x_t	0.191	nm
E_t	-0.336	eV
$E_{\mathrm{t}'}$	-0.289	eV
$\varepsilon_{\mathrm{T}2'}$	0.54	eV
$R_{12'}$	0.67	1
$S_{12'}\hbar\omega$	1.334	eV
$R_{1'2}$	0.584	1
$S_{1'2}\hbar\omega$	1.661	eV
$\varepsilon_{1'1}$	0.794	eV
$\varepsilon_{2'2}$	0.484	eV
σ_0	1.386×10^{-13}	cm^2

Table 4.3: NMP four state parameters of the switching trap.

tion 4.2, yielded the parameters as listed in Table 4.3. The corresponding time constants are shown in Figure 4.5. Again, the time constants are mainly governed by transitions between the valence band and the oxide trap because the electron concentration in the conduction band is too low for the given gate voltages. Considering valance band transitions only, the configuration coordinate diagram (compare Figure 4.6) shows a strong bias dependence of the barrier $\varepsilon_{21'}$, whereas $\varepsilon_{22'}$ is bias independent. As hole emission from state 2 to 1 via the metastable state $2'$ is determined by the large barrier $\varepsilon_{22'}$, the emission time constant is bias independent for this path. For hole emission via the metastable state $1'$, the bias dependent barrier $\varepsilon_{21'}$ dominates. Therefore, the emission time constant for this path is bias dependent as well. Now at low gate voltages the barrier $\varepsilon_{22'}$ is large compared to $\varepsilon_{21'}$ and emissions will be governed by the bias dependent path via $1'$. Approaching higher gate voltages, hole emission proceeds via $2'$, because the overall barrier from state 2 to 1 is lower for the pathway via $2'$ than that via $1'$. The two transition paths show different emission time constants and therefore, the bias dependent change of the principal path induces a strong bias dependence of the emission time constant.

4.4 Regimes

The bias dependence of capture and emission time constants can be split in regimes, which are dominated by different transitions [29, 40]. The time constants $\tau_\mathrm{c}(F)$ and $\tau_\mathrm{e}(F)$ can be split in a field dependent part $\tau_{\mathrm{c,F}}(F)$ and $\tau_{\mathrm{e,F}}(F)$ and a field independent

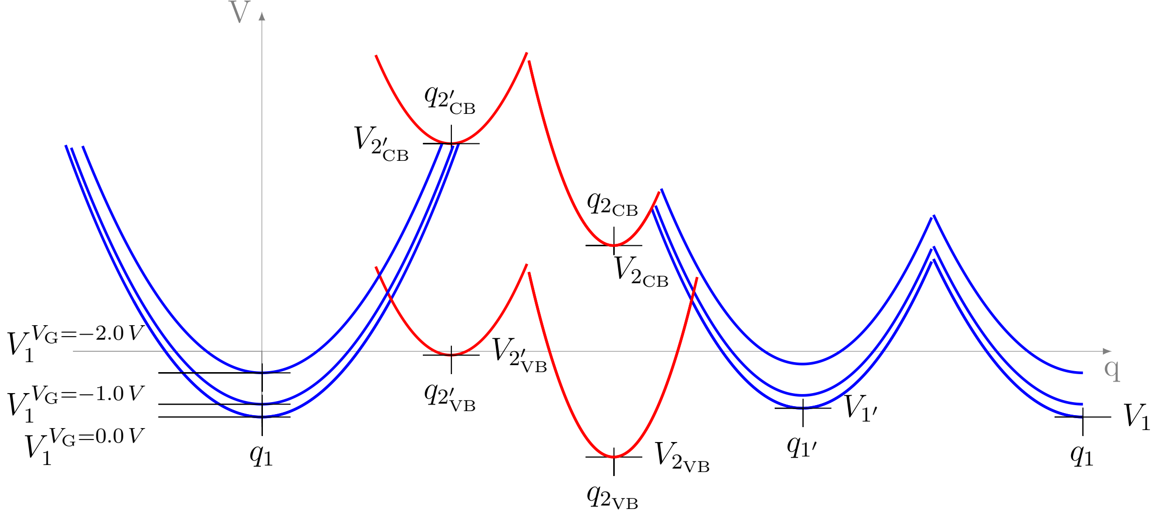

Figure 4.6: Configuration coordinate diagram of the switching trap. The configuration is plotted for three different gate voltages to show bias dependence of τ_{e}. Depending on the gate voltage, transitions between state 1 and 2 are possible via both states $1'$ and $2'$. The parameters are discussed in detail in Section 4.4.

part $\tau_{\mathrm{c},0}$ and $\tau_{\mathrm{e},0}$, respectively.

$$\tau_{\mathrm{c}}(F) = \tau_{\mathrm{c},0} + \tau_{\mathrm{c,F}}(F) \tag{4.6}$$

$$\tau_{\mathrm{e}}(F) = \tau_{\mathrm{e},0} + \tau_{\mathrm{e,F}}(F) \tag{4.7}$$

In the following the different regimes and their slopes in Figure 4.7 will be separately discussed for τ_{c} and τ_{e}.

4.4.1 Capture Time Constant

The capture time constant introduced in Section 3.3.4 can be rewritten as

$$\tau_{\mathrm{c}} = \frac{1}{\frac{1}{{\tau_{\mathrm{c}}}^{1'}} + \frac{1}{{\tau_{\mathrm{c}}}^{2'}}} \tag{4.8}$$

$${\tau_{\mathrm{c}}}^{1'} = \frac{1}{k_{11'}} + \frac{1}{k_{1'2}} + \frac{k_{1'1}}{k_{1'2}k_{11'}} \tag{4.9}$$

$${\tau_{\mathrm{c}}}^{2'} = \frac{1}{k_{12'}} + \frac{1}{k_{2'2}} + \frac{k_{2'1}}{k_{2'2}k_{12'}}. \tag{4.10}$$

In the NMP four state model, hole capture is expected to be governed by the transitions via the metastable state $2'$, so only ${\tau_{\mathrm{c}}}^{2'}$ will be considered in the following. In the relevant range of gate voltages, roughly from -0.5 to $-2\,\mathrm{V}$, the Fermi level is usually close to the valance band edge, which results in a high hole concentration and a low electron

concentration at the interface. Therefore it is reasonable to consider transitions between the valence band and the oxide trap only and the transition rates (3.85) to (3.88) can be approximated by

$$k_{12'} = k_{12'}^{\mathrm{C}} + k_{12'}^{\mathrm{V}} \approx k_{12'}^{\mathrm{V}} \quad (4.11)$$

$$k_{2'1} = k_{2'1}^{\mathrm{C}} + k_{2'1}^{\mathrm{V}} \approx k_{2'1}^{\mathrm{V}}. \quad (4.12)$$

For these two assumptions following regimes (compare Figure 4.7) can be identified:

- In the regime "A" the rate $k_{2'1}$ is assumed to be large compared to the rate $k_{12'}$ and $k_{2'2}$. Therefore the capture time constant (4.8) can be approximated by

$$\tau_{\mathrm{c}} \approx \frac{k_{2'1}}{k_{12'}k_{2'2}}. \quad (4.13)$$

  Therein the bias dependence is governed by the ratio of $k_{2'1}$ and $k_{12'}$. By substituting the rate equation (4.11) and (4.12) in the above equation, one obtains the following dependence

$$\tau_{\mathrm{c,F}}(F) \propto \mathrm{e}^{\beta q_0 x_{\mathrm{t}} F} \quad (4.14)$$

  which defines the slope as shown in figure (4.7).

- In the regime "B" the rate $k_{2'2}$ is assumed to be large compared to the rate $k_{12'}$ and $k_{2'1}$. Therefore the capture time constant (4.8) can be approximated by

$$\tau_{\mathrm{c}} \approx \frac{1}{k_{12'}}. \quad (4.15)$$

  Evaluating this expression with the rate equation (4.11), the slope as shown in Figure 4.7, is given by the dependence

$$\tau_{\mathrm{c,F}}(F) \propto \mathrm{e}^{-\beta \frac{R_{12'} q_0 x_{\mathrm{t}} F}{1+R_{12'}}}. \quad (4.16)$$

- In the regime "C" the rate $k_{12'}$ is assumed to be large compared to the rate $k_{2'1}$ and $k_{2'2}$. Therefore the capture time constant (4.8) can be approximated by

$$\tau_{\mathrm{c}} \approx \frac{1}{k_{22'}}. \quad (4.17)$$

  As the transition rate $k_{22'}$ is bias independent also the capture time constant is bias independent in this regime.

With the different slopes of the regimes "A", "B" and "C", a curvature of τ_{c} can be described as shown in Figure 4.7. As such, the four NMP four state model can reproduce the observed curvatures approximated by equation (4.1).

4.4.2 Emission Time Constant

The emission time constant introduced in Section 3.3.4 can be rewritten as

$$\tau_\mathrm{e} = \frac{1}{\dfrac{1}{\tau_\mathrm{e}{}^{1'}} + \dfrac{1}{\tau_\mathrm{e}{}^{2'}}} \tag{4.18}$$

$$\tau_\mathrm{e}{}^{1'} = \frac{1}{k_{21'}} + \frac{1}{k_{1'1}} + \frac{k_{1'2}}{k_{1'1}k_{21'}} \tag{4.19}$$

$$\tau_\mathrm{e}{}^{2'} = \frac{1}{k_{22'}} + \frac{1}{k_{2'1}} + \frac{k_{2'2}}{k_{2'1}k_{22'}}. \tag{4.20}$$

For the general case of switching traps, hole emission is possible by transitions via the metastable states $2'$ and $1'$. As metastable states have higher energy mimima than stable states ($V_{2'} > V_2$), the barrier $\varepsilon_{22'}$ is higher than $\varepsilon_{2'2}$. Therefore the rate $k_{2'2}$ is higher than $k_{22'}$ and equation (4.20) can be approximated by

$$\tau_\mathrm{e}{}^{2'} \approx \frac{1}{k_{22'}} + \frac{k_{2'2}}{k_{2'1}k_{22'}}. \tag{4.21}$$

With the same argument as in Section 4.4.1, only transitions between the valence band and the oxide trap are considered. Therefore the transition rates (3.85) to (3.88) can be approximated by

$$k_{21'} = k^\mathrm{C}_{21'} + k^\mathrm{V}_{21'} \approx k^\mathrm{V}_{21'} \tag{4.22}$$

$$k_{1'2} = k^\mathrm{C}_{1'2} + k^\mathrm{V}_{1'2} \approx k^\mathrm{V}_{1'2}. \tag{4.23}$$

For these assumptions, the following regimes (compare Figure 4.7) can be identified:

- In the regime “D” hole emission is governed by transitions via $1'$. Furthermore one of the rates $k_{1'2}$ and $k_{21'}$ is assumed to be large compared to the rate $k_{1'1}$. Therefore the emission time constant (4.18) can be approximated by

  $$\tau_\mathrm{e} \approx \frac{1}{k_{1'1}} + \frac{k_{1'2}}{k_{1'1}k_{21'}}. \tag{4.24}$$

  The second term of this equation can be rewritten as

  $$\frac{k_{1'2}}{k_{1'1}k_{21'}} = \frac{1}{k_{1'1}}\mathrm{e}^{-\beta(E_\mathrm{F}-E_\mathrm{t}{}'(F))}. \tag{4.25}$$

  At low gate voltages, the electric field in the oxide F becomes small which results in $E_\mathrm{t}{}'(F) < E_\mathrm{F}$. In this case, τ_e is dominated by the first term of equation (4.24).

  $$\tau_\mathrm{e} \approx \frac{1}{k_{1'1}} \tag{4.26}$$

  As the transition rate $k_{1'1}$ is bias independent also the emission time constant is bias independent in this regime.

For higher gate voltages, F becomes larger which results in $E_t{}'(F) > E_F$. Thereby, the first term in equation (4.24) can be neglected and the emission time constant can be approximated by

$$\tau_e \approx \frac{k_{1'2}}{k_{1'1}k_{21'}} \propto e^{-\beta(E_F - E_t{}'(F))}. \tag{4.27}$$

- In the regime "E", hole emission is governed by transitions via 2′ and the rate $k_{2'1}$ is large compared to the rate $k_{22'}$. Therefore, the emission time constant (4.21) can be approximated by

$$\tau_e \approx \frac{1}{k_{22'}}. \tag{4.28}$$

  As the transition rate $k_{22'}$ is bias independent, also the emission time constant is bias independent in this regime.

- In the regime "F", the rate $k_{22'}$ is large compared to the rate $k_{2'1}$ and the emission time constant (4.21) can be approximated by

$$\tau_e \approx \frac{k_{2'2}}{k_{22'}k_{2'1}}. \tag{4.29}$$

  Therein the bias dependence is governed by $k_{2'1}$. By substituting the rate equation (4.22) in the above equation, one obtains [29] the dependence

$$\tau_{e,F}(F) \propto e^{-\beta \frac{R_{12'} q_0 x_t F}{1+R_{12'}}} \tag{4.30}$$

  which defines the slope as shown in Figure 4.7.

The examinations above reveal that the reason for the step of the emission time from regime "D" to "E" is because τ_e is governed by the transition via 1′ at low gate voltages and the transition via 2′ is dominant at higher gate voltages.

4.5 Conclusions

Parameters of the NMP four state model were extracted for a fixed positive charge trap and a switching trap. The resulting time constants are in good agreement with the experimental data from TDDS. The comparison of the results and the analysis of the NMP four state model showed that:

1. The temperature dependence of the capture and emission time constants, found in the measurement data, can be reproduced by the NMP four state model.
2. Making use of the three different regimes in the NMP four state model, the experimentally observed curvature can be reproduced.
3. The different behavior of fixed positive charge traps and switching traps can be modeled by two different transition pathways in the NMP four state model.

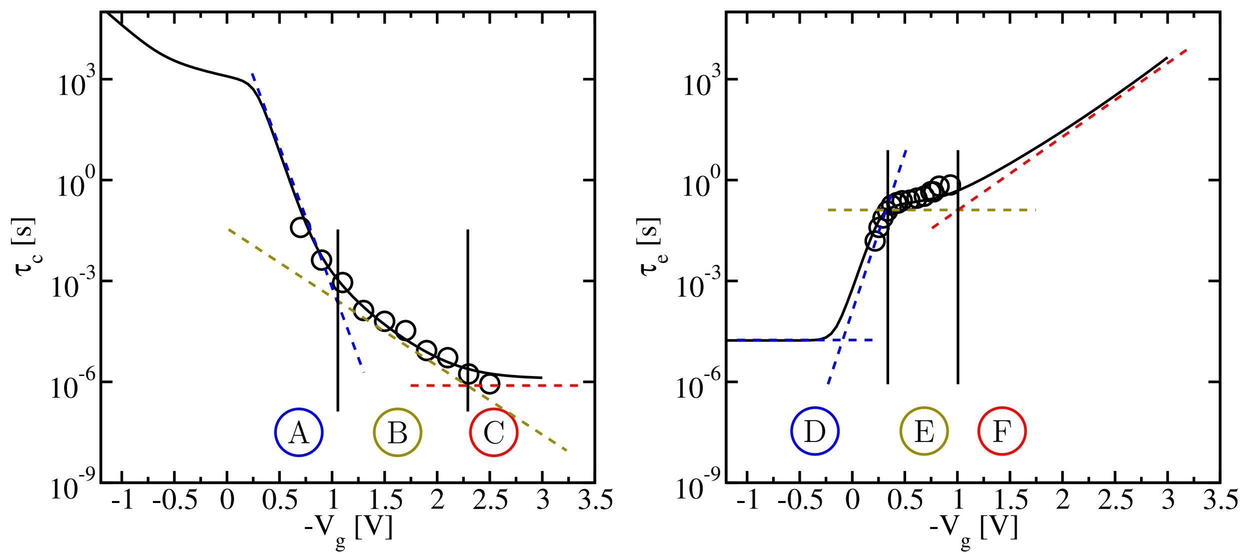

Figure 4.7: Typical capture and emission times of a switching trap at $T = 125°C$. The circles indicate measurement data, the lines represent simulation results. The regimes, separated by vertical lines, are labeled according to the explanations of Section 4.4. The dotted lines indicate the approximated slope of the time constants in the corresponding regimes.

CHAPTER 5 Simulation of Degradation

With OTF measurements, described in Section 2.2.2, the threshold voltage shift (ΔV_{th}) of MOSFETs is accessible at different temperatures and gate voltages. Based on such measurement data, the distributions of the parameters of the NMP four state model will be extracted. The measurement data and its preparation, the simulation setup, the parameter optimization, and the obtained results will be discussed in this chapter.

5.1 Measurement Data

In order to extract model parameters for device degradation, the measured threshold voltage shift can be compared to simulation results. For this, the measured device must be accurately reproduced by the simulation device. This can be achieved by an optimization of the simulated C(V)-curve, based on the known geometry of the device. Both, the the C(V)-curve and measurement data of the threshold voltage shift were provided for reproducing the simulation device and the extraction of the model parameters [25].

5.1.1 Threshold Voltage Shift

OTF measurements provide the threshold voltage shift of MOSFETs during the stress and the recovery phases. Figure 5.1 shows the experimental results for different gate voltages and temperatures on a large pMOSFET device [25]. The stress voltages $V_{\mathrm{G}}^{\mathrm{H}}$ are -1 and $-2\,\mathrm{V}$. The recovery voltages $V_{\mathrm{G}}^{\mathrm{L}}$ are $-0.34\,\mathrm{V}$ and $-0.28\,\mathrm{V}$ for the temperatures $T = 50°\mathrm{C}$ and $T = 150°\mathrm{C}$, respectively. The threshold voltage shift increases for higher gate voltages and higher temperatures. Furthermore, the threshold voltage shifts considerably faster during stress ($t_{\mathrm{s}} = 2.296\,\mathrm{s}$) than it does during recovery ($t_{\mathrm{r}} = 2832\,\mathrm{s}$). In the given measurement period, no saturation of the ΔV_{th} can be observed. This is in accordance with the findinges of recent studies [41].

In order to cope with the noise in the measurement data, especially at the beginning of the stress phase, the measurement data was filtered with a low pass. The time points for the parameter extraction, described below, were separately chosen on a logarithmic

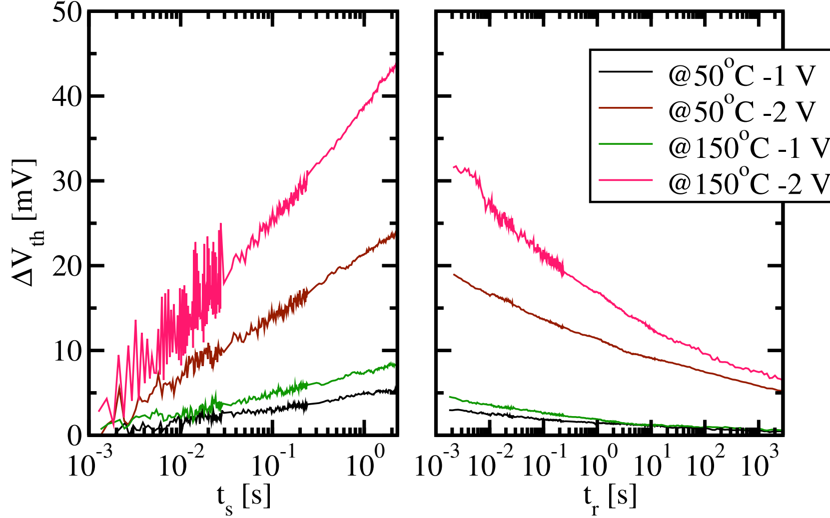

Figure 5.1: Threshold voltage shift obtained by OTF measurements during stress (left) and recovery (right) [25]. At the beginning of the stress phase, the data is too noisy for a direct comparison with simulation results.

scale for the stress and the recovery phase. The result of the filtered threshold voltage shift is shown in Figure 5.2.

5.1.2 CV Curve

For device characterization, a C(V)-curve was employed. The measured C(V)-curve for low frequency [25] is shown in Figure 5.3. The threshold voltage is found to be around 0.75 V and the effect of tunneling through the gate is observed for large gate voltages $|V_{\mathrm{G}}|$.

5.2 Device Generation

The generation of the simulation device was done in two steps. First, the basic geometry of the device was chosen to match that of the measurement device. Second, the doping and the workfunction difference were optimized to achieve a good match of the measured and the simulated C(V)-curve. These two steps are explained in the following.

5.2.1 Geometry

A device geometry for subsequent simulations was created using the device editor GTS Structure [35] of Global TCAD Solutions. The measured device is represented by a two-dimensional pMOSFET with a gate length (l) of 500 nm, a width (W) of 10 μm and an oxide thickness (t_{ox}) of 1.4 nm. A metal gate was used and the mesh of the device was chosen to be orthogonal with refinements in the channel region.

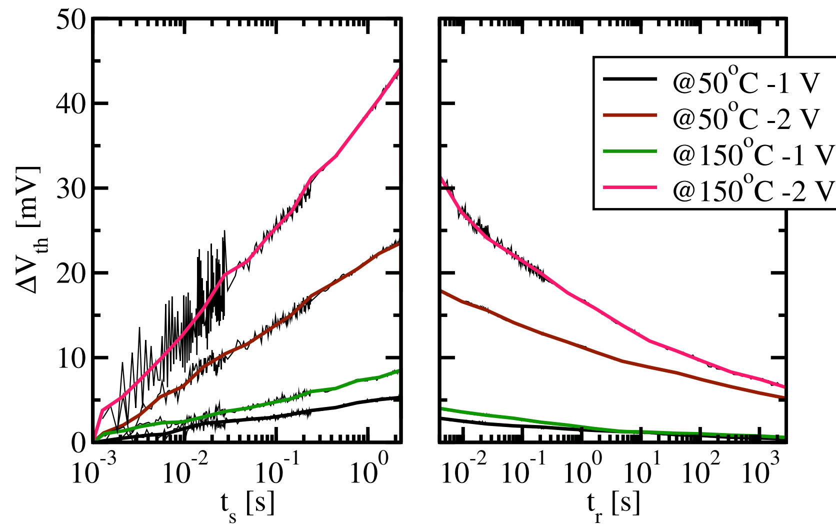

Figure 5.2: Threshold voltage shift obtained by OTF measurements (thin lines) [25] and the same data processed by a low pass filter (bold lines).

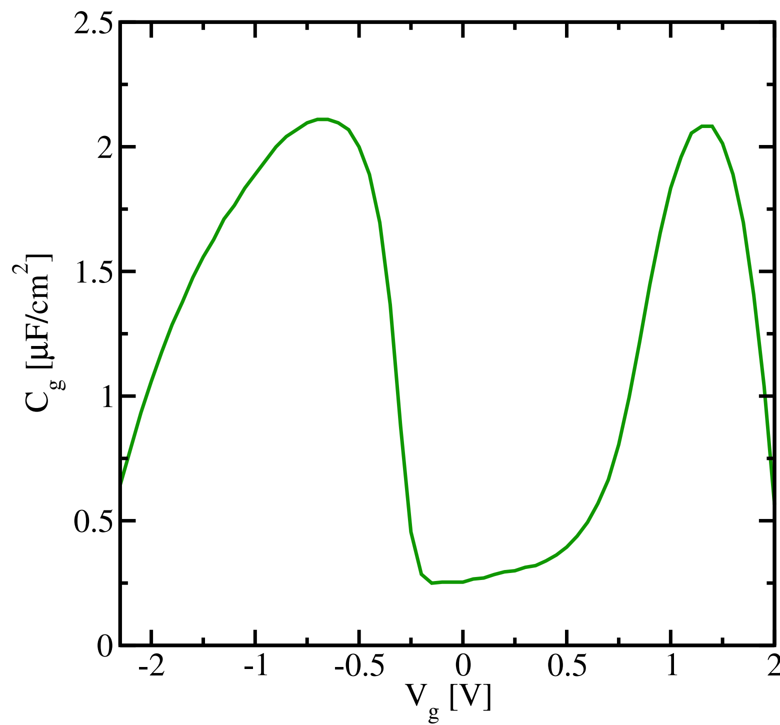

Figure 5.3: Measured C(V)-curve of the device whose threshold voltage shift was simulated [25].

5.2.2 Device Optimization

The rough doping concentration and distributions of the measurement device were known, but the match of the resulting C(V)-curve with the measurement was not satisfying. In order to improve the match of the C(V)-curves, the optimizer tool of Global TCAD Solutions [38] was used with the input parameters listed in Table 5.1. The flowchart of the optimization scheme is shown in Figure 5.4 and will be described below. First, a reasonable initial guess $S_{\mathrm{init}} = \{P_1, P_2, ...P_N\}$ for the N parameters $P_1, P_2, ...P_N$ was assumed. Together with the given device geometry, a simulation device D was generated. Based on this device, a $C_{\mathrm{g}}(V_{\mathrm{G}})$-curve was simulated using Minimos-NT. Together with the measured $C_{\mathrm{g,real}}(V_{\mathrm{G}})$-curve for K gate voltages, a score C_{s} was calculated as

$$C_{\mathrm{s}} = \sum_{n=1}^{K} |C_{\mathrm{g,real}}(V_{\mathrm{G},n}) - C_{\mathrm{g}}(V_{\mathrm{G},n})|. \tag{5.1}$$

If the score value was too large, the optimizer created N new sets of parameters $S_1, S_2, ...S_N$. In each set S_i, one parameter P_i was varied by adding a small value ΔP_i while the other parameters remained unchanged.

$$S_i = \{P_1, P_2, ..., P_{i-1}, P_i + \Delta P_i, P_{i+1}, ..., P_N\},\ i\epsilon\{1, 2, ...N\} \tag{5.2}$$

For each of these parameter sets, a simulation was carried out and a score was calculated in the same way as for the initial guess. Based on the resulting N score values $C_{\mathrm{s},1}, C_{\mathrm{s},2}, ...C_{\mathrm{s},N}$, a constrained nonlinear optimization algorithm [39] determined a new set of parameters S_{new} which is expected to yield an improved score value. A new iteration was started by continuing with this set S_{new} and calculating the new device D. Usually, the progress of the score and of the corresponding simulation results is monitored during the optimization. Optimizations with undesired trends were avoided by a modification of the parameter constraints. As the source and the drain doping of MOSFETs are done with the same processing steps, their distributions were assumed to be similar. Therefore the distribution of their doping shared the same parameters in the optimization. The resulting parameter set of the optimization is listed in Table 5.2. The corresponding $C_{\mathrm{g}}(V_{\mathrm{G}})$-curve is shown in Figure 5.5. As the simulation did not consider tunneling through the thin gate segment, the capacity for higher absolute gate voltages differ from the measurement result.

5.3 Device Simulation

5.3.1 General Simulation Setup

The device simulator Minimos-NT [36] of Global TCAD Solutions was used to solve the Poisson equation and the drift-diffusion equation, which are coupled by the quantities n, p and ψ. The quantities n, p, ψ, E_{C}, and E_{V} are needed to evaluate the transition rates of the NMP four state model (compare Section 3.3.2). Since the carrier transport was

Parameter	Description
ΔE_{w}	Workfunction difference between the substrate and the gate
$N_{\mathrm{D,subs}}$	Donor concentration of the substrate (constant)
$N_{\mathrm{A,S}}$	Acceptor concentration of the source (normal distributed)
$\sigma_{\mathrm{y,S}}$	Variance of the source doping perpendicular to the interface
$\sigma_{\mathrm{x,S}}$	Variance of the source doping longitudinal to the interface
$N_{\mathrm{A,D}}$	Acceptor concentration of the drain (normal distributed)
$\sigma_{\mathrm{y,D}}$	Variance of the drain doping perpendicular to the interface
$\sigma_{\mathrm{x,D}}$	Variance of the drain doping longitudinal to the interface

Table 5.1: Parameters of the device optimization.

Parameter	Value	Unit
ΔE_{w}	0.328	eV
$N_{\mathrm{D,subs}}$	3.08×10^{17}	cm^{-3}
$N_{\mathrm{A,S}}$	1.014×10^{20}	cm^{-3}
$\sigma_{\mathrm{y,S}}$	1.14	nm
$\sigma_{\mathrm{x,S}}$	0.0	nm
$N_{\mathrm{A,D}}$	1.014×10^{20}	cm^{-3}
$\sigma_{\mathrm{y,D}}$	1.14	nm
$\sigma_{\mathrm{x,D}}$	0.0	nm

Table 5.2: Resulting parameters obtained by an optimization of the C(V)-curve. The parameters are explained in Table 5.1 and the resulting C(V)-curve is shown in Figure 5.5.

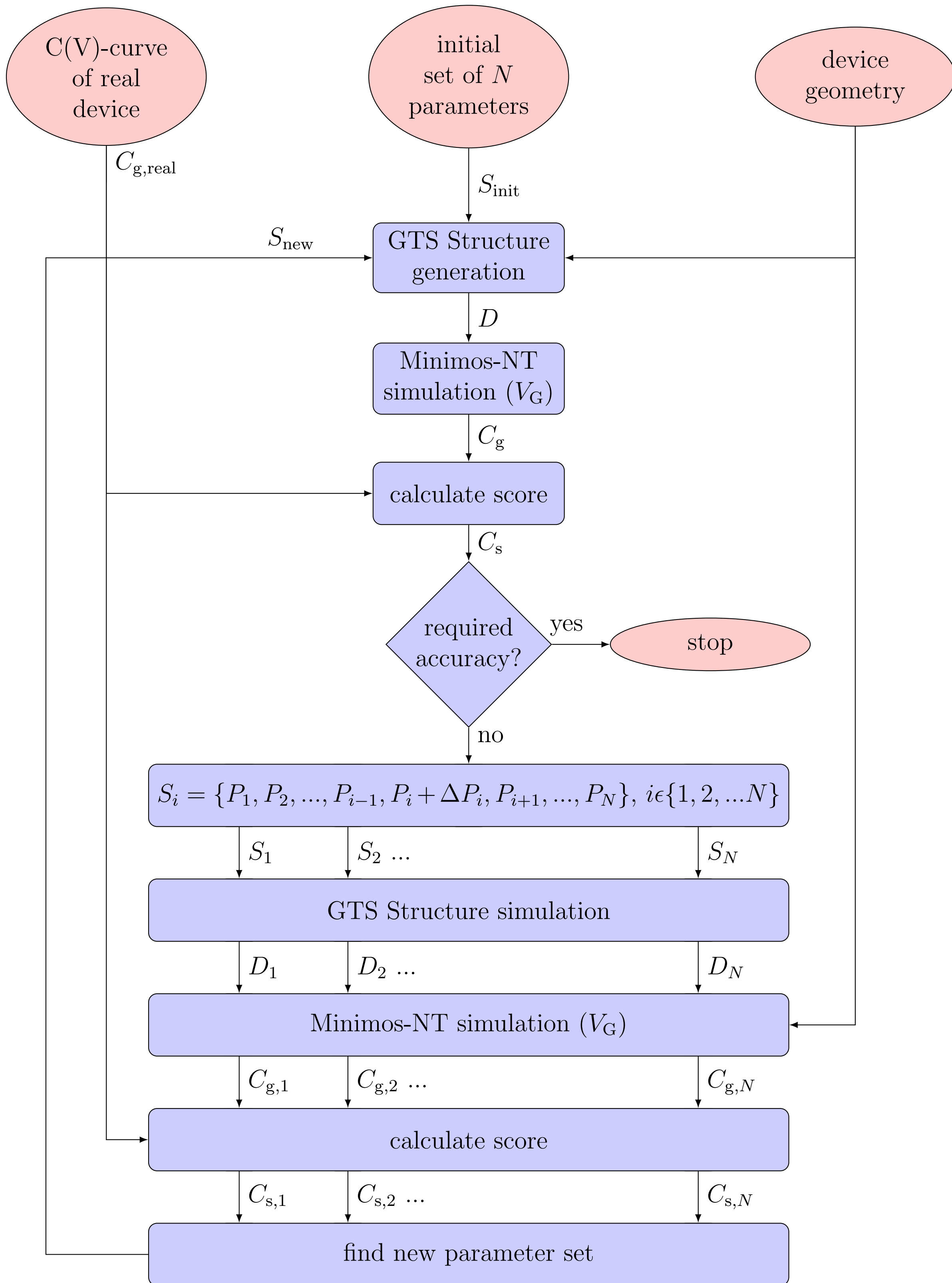

Figure 5.4: Scheme of the device optimization as described in Section 5.2.2.

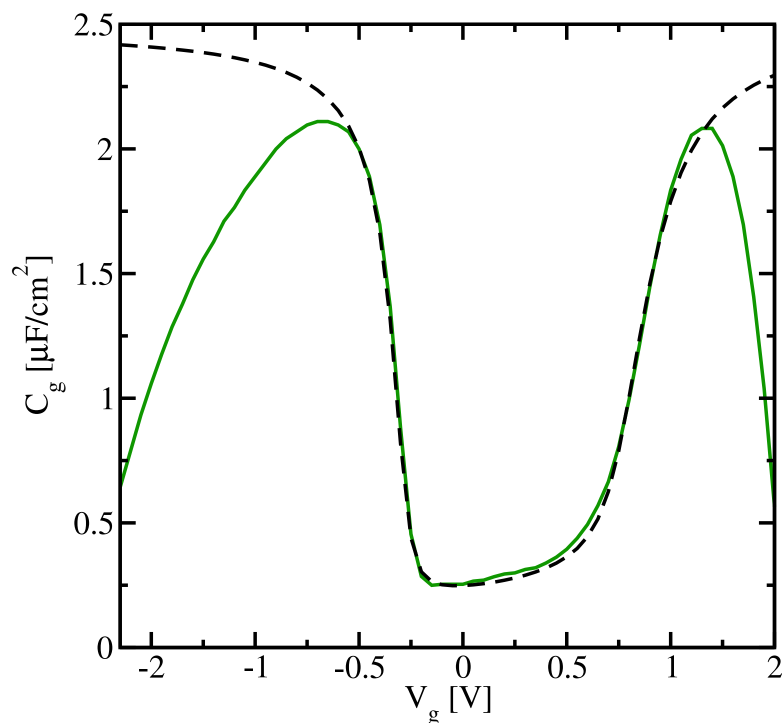

Figure 5.5: Simulated (dashed) and measured (solid) C(V)-curve. The curves show a good agreement in the relevant voltage range between −0.5 V and 1 V. The simulation data deviates for larger gate voltages, as tunneling through the gate was not considered in the simulations.

simulated within the drift-diffusion model, Boltzmann statistics were implicitly assumed. A transient simulation was carried out using a time stepping which included the time points of the processed measurement data as described in Section 5.1.1. The constant bulk and source voltages were set to $V_{\mathrm{B/S}} = 0\,\mathrm{V}$ and a small constant drain voltage V_{D} of $50\,\mathrm{mV}$ was applied. For the initial equilibrium solution at $t = 1\,\mathrm{ps}$, the gate voltage was set to the recovery voltage $V_{\mathrm{G}}^{\mathrm{L}}$. At the next time step at $t = 2\,\mathrm{ps}$, stress was simulated with a gate voltage of $V_{\mathrm{G}}^{\mathrm{H}}$. After a stress time t_{s}, the gate voltage was set to $V_{\mathrm{G}}^{\mathrm{L}}$ until the end of the simulation at $t = t_{\mathrm{s}} + t_{\mathrm{r}}$. These simulations were performed for the two temperatures chosen in the measurements and for two different combination of stress and recovery voltages.

5.3.2 NMP Four State Model

The recoverable component of the threshold voltage shift was simulated with the NMP four state model described in Section 3.3. Based on a distribution of parameters, discrete traps were generated. The charges of those traps resulted in a threshold voltage shift, which was calculated with the charge sheet approximation. In the following the traps and their contribution to the threshold voltage shift will be discussed.

As the microscopic nature of the defects are uncertain (compare Section 2.3), also the spatial distribution of the traps in the oxide is not known. Facing this lack of evidence, a uniform trap distribution appeared to be the most reasonable choice. The implementation of the NMP four state model in Minimos-NT accounts only for charge exchange between the oxide and the substrate. Because of the tunneling distances, it is reasonable to assume that only the traps in the half of the oxide next to the substrate, are controlled by charge exchange with the substrate [9]. Therefore, the traps were uniformly distributed in this half of the oxide, with the density D_{NMP}. Research, based on DFT calculations, should provide estimations for possible distributions of the trap parameters of the NMP four state model [6]. But, as there are no fully established results available yet, most parameters of the traps were assumed to be Gaussian distributed. The distributions had to respect the valid range of the parameters. Therefore, random values outside of this range were dropped and replaced by a newly generated value. This results in N_{NMP} discrete traps, each with a unique set of parameters. The parameters of the traps, their distributions, and their valid ranges are listed in Table 5.3. Based on these parameters, the transition rates of the corresponding trap can be obtained using the equations (3.85) to (3.92). At the first time step of the simulation, the equilibrium solution of the occupation probabilities was calculated as described in Section 3.3.3. The resulting charge $q_{\mathrm{NMP}}(t)$ of the trap were obtained from these occupation probabilities using the expression (3.100). For all subsequent time steps the change of the occupation probabilities was determined by the solution of their master equations as discussed in Section 3.3.3. Again, the charge is obtained by equation (3.100).

Parameter	Description	Distribution	Lower limit
x_{t}	Trap distance from the interface	Uniform	
y_{t}	Trap position along the channel direction	Uniform	
E_{t}	Trap level of the stable state 1	Gaussian	$-\infty$
$E_{\mathrm{t'}}$	Trap level of the metastable state 1′	Gaussian	$-\infty$
$\varepsilon_{\mathrm{T2'}}$	Energy difference between states 2 and 2′	Gaussian	0 eV
$R_{12'}$	Curvature ratio between states 1 and 2′	Gaussian	0
$S_{12'}$	Huang-Rhys factor between states 1 and 2′	Gaussian	0
$R_{1'2}$	Curvature ratio between states 1′ and 2	Gaussian	0
$S_{1'2}$	Huang-Rhys factor between states 1′ and 2	Gaussian	0
$\varepsilon_{1'1}$	Barrier from state 1′ to 1	Gaussian	0 eV
$\varepsilon_{2'2}$	Barrier from state 2′ to 2	Gaussian	0 eV
σ_0	Capture cross section	Constant	
ν_0	Attempt frequency	Constant	

Table 5.3: Parameters of an NMP four state trap and the distribution of these parameters, which were assumed for the generation of a multitude of traps. The lower limits have to be considered for a proper simulation result.

5.3.3 Double Well Model

The permanent component of the threshold voltage shift was simulated with the double well model described in Section 3.4. Defects which contribute to the permanent component have different time constants compared to defects of to the recoverable component. But, regarding the microscopic nature, the two types of defects cannot be distinguished as they are both not identified yet. For this reason the same consideration apply as for the traps of the NMP four state model in Section 5.3.2. Only, the traps of the permanent component were assumed to be at the interface between the oxide and the substrate. Along the interface, they were uniformly distributed, with the density D_{DW}. The distributions of the other trap parameters were assumed to be Gaussian, limited by a range of valid values. So, each of the N_{DW} discrete traps have a unique set of parameters as listed in Table 5.4. With those parameters, the transition rates of the traps can be obtained using equations (3.116) and (3.117). The equilibrium solution of the occupation probabilities for the first time step is given by the equations (3.120) and (3.121). The charge $q_{\mathrm{DW}}(t)$ of the trap can be calculated based on the occupation probabilities using the equation (3.124). The trap level $E_{\mathrm{t,DW}}$ was assumed to be distributed around the middle of the band gap and because the E_{F} was found to be close to the valence band edge for the considered gate voltages, f_{p} was equal 1 for all traps of the double well model. For all subsequent time steps the change of the occupation probabilities was determined by the solution of their master equations (3.122) and (3.123).

Parameter	Description	Distribution	Lower limit
x_t	Trap distance from the interface	Uniform	
y_t	Trap position along the channel direction	Uniform	
V_B	System energy of state B	Gaussian	$-\infty$
V_AB	System energy at the barrier	Gaussian	$0\,\mathrm{eV}$
γ	Factor defining the bias dependence	Gaussian	$-\infty$
ν_0	Attempt frequency	Constant	

Table 5.4: The same as in Table 5.3 but for the double well model.

5.3.4 Threshold Voltage Shift

The charges of the traps, obtained from the simulation of the NMP four state model and the double well model, induce a threshold voltage shift. If these charges are considered in the Poisson equation, the corresponding threshold voltage shift can be obtained. Thereby, the effect of the trap charges on the transition rates is considered as well. This results in a self-consistent solution regarding the traps charges. But, for large devices with many traps, this can be time-consuming. As simulation time is crucial for optimization processes with many parameters and a lot of iterations, the effect of the trap charges on the threshold voltage shift was obtained using the charge sheet approximation [42]. This approximation is based on the assumption that a trap charge q_t in the oxide can be described as a homogeneous charge sheet with the charge sheet density

$$\sigma_\mathrm{t} = \frac{q_\mathrm{t}}{WL}. \tag{5.3}$$

The electric flux, obtained by the Gaussian law applied to the volume $\mathcal{V}$ shown in Figure 5.6, evaluates to

$$\Psi(\partial\mathcal{V}) = Q(\mathcal{V}) = q_\mathrm{t}, \quad x_\mathrm{t} < x < t_\mathrm{ox}. \tag{5.4}$$

Therefore, the electric displacement field can be written as

$$D = \frac{q_\mathrm{t}}{WL}, \quad x_\mathrm{t} < x < t_\mathrm{ox} \tag{5.5}$$

and the corresponding electric flied is

$$E = \frac{q_\mathrm{t}}{\epsilon_0\epsilon_\mathrm{r}WL}, \quad x_\mathrm{t} < x < t_\mathrm{ox}. \tag{5.6}$$

Then the voltage V_t evaluates to

$$V_\mathrm{t} = -q_\mathrm{t}\frac{t_\mathrm{ox}\left(1 - \frac{x_\mathrm{t}}{t_\mathrm{ox}}\right)}{\epsilon_0\epsilon_\mathrm{r}WL}. \tag{5.7}$$

The actual impact of a trap charge on the threshold voltage can be higher than the estimation by (5.7), due to the distribution of the traps and inhomogeneous current

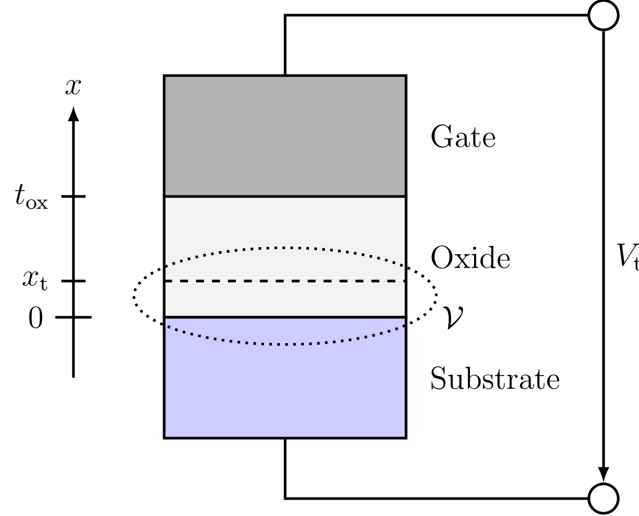

Figure 5.6: Schematic stack of a gate, oxide and substrate segment. For the charge sheet approximation, the trap charge at position x_{t} is described by a charge sheet, indicated by a dashed line. The resulting value of the voltage V_{t} can be calculated by applying Gauss' law to the volume $\mathcal{V}$.

density in the channel [43]. To account for this effect the parameter η_{r} was introduced [44]. When the charges $q_{\mathrm{t},1}, q_{\mathrm{t},2}, ...q_{\mathrm{t,N_t}}$ of the N_{t} traps are considered, their contribution $V_{\mathrm{t}}(i)$ to the threshold voltage at time step i is

$$V_{\mathrm{t}}(i) = \sum_{n}^{N_{\mathrm{t}}} \left(-q_{\mathrm{t},n}(i) \frac{t_{\mathrm{ox}} \left(1 - \frac{x_{\mathrm{t}}}{t_{\mathrm{ox}}}\right)}{\epsilon_0 \epsilon_{\mathrm{r}} W L} \eta_{\mathrm{r,n}} \right). \tag{5.8}$$

Finally, the threshold voltage shift $\Delta V_{\mathrm{th}}^{i,j}$ is obtained as

$$\Delta V_{\mathrm{th}}^{i,j} = V_{\mathrm{t}}(j) - V_{\mathrm{t}}(i). \tag{5.9}$$

The values of η_{r} were found to be exponentially distributed with a mean value $\overline{\eta_{\mathrm{r}}}$ [44]. As a large number of defect were considered, the distribution of η_{r} was replaced by its mean value $\overline{\eta_{\mathrm{r}}}$. For the device described in Section 5.2, $\overline{\eta_{\mathrm{r}}}$ was found to be 2.182 by matching the degradation curves based on the charge sheet approximation and the self-consistent solution.

5.4 Optimization of the Model Parameters

The parameters which where used to optimize the threshold voltage shift, are listed in Table 5.5. The flowchart of the optimization scheme is shown in Figure 5.7 and is described below. First, a reasonable initial guess $S_{\mathrm{init}} = \{P_1, P_2, ...P_N\}$ for the N parameters $P_1, P_2, ...P_N$ was assumed. A simulation based on these parameters, with the simulation setup as explained above, yielded simulation values for the threshold voltage

Parameter	Description	Model
D_{NMP}	Constant trap density	NMP
$\overline{E}_{\mathrm{t}}$, $\sigma_{E_{\mathrm{t}}}$	Trap level of the stable state 1	NMP
$\overline{E}'_{\mathrm{t}}$, $\sigma_{E_{\mathrm{t}'}}$	Trap level of the metastable state 1′	NMP
$\overline{\varepsilon}_{\mathrm{T2}'}$, $\sigma_{\varepsilon_{\mathrm{T2}'}}$	Energy difference between states 2 and 2′	NMP
$\overline{R}_{12'}$, $\sigma_{R_{12'}}$	Curvature ratio between states 1 and 2′	NMP
$\overline{S}_{12'}$, $\sigma_{S_{12'}}$	Huang-Rhys factor between states 1 and 2′	NMP
$\overline{R}_{1'2}$, $\sigma_{R_{1'2}}$	Curvature ratio between states 1′ and 2	NMP
$\overline{S}_{1'2}$, $\sigma_{S_{1'2}}$	Huang-Rhys factor between states 1′ and 2	NMP
$\overline{\varepsilon}_{1'1}$, $\sigma_{\varepsilon_{1'1}}$	Barrier from state 1′ to 1	NMP
$\overline{\varepsilon}_{2'2}$, $\sigma_{\varepsilon_{2'2}}$	Barrier from state 2′ to 2	NMP
σ_0	Capture cross section	NMP
D_{DW}	Constant trap density	DW
$\overline{V}_{\mathrm{B}}$, σV_{B}	System energy of state B	DW
$\overline{V}_{\mathrm{AB}}$, $\sigma_{V_{\mathrm{AB}}}$	System energy at the barrier	DW
$\overline{\gamma}$, σ_{γ}	Factor defining the bias dependence	DW
ν_0	Attempt frequency	Both

Table 5.5: Parameters of the NMP four state model (NMP) and of the double well model (DW), which were both used to simulate the threshold voltage shift.

shift $\Delta V_{\mathrm{th}}(V_{\mathrm{G}}^{\mathrm{H}}, V_{\mathrm{G}}^{\mathrm{L}}, T)$. Together with the threshold voltage shift of the measurement data $\Delta V_{\mathrm{th,real}}(V_{\mathrm{G}}^{\mathrm{H}}, V_{\mathrm{G}}^{\mathrm{L}}, T)$ for K combinations of the voltages $V_{\mathrm{G}}^{\mathrm{H}}$ and $V_{\mathrm{G}}^{\mathrm{L}}$, for M temperatures, and for J time steps, a score V_{s} was calculated as

$$V_{\mathrm{s}} = \sum_{n=1}^{K} \sum_{m=1}^{M} \sum_{j=1}^{J} |\Delta V_{\mathrm{th,real}}(V_{\mathrm{G},n}^{\mathrm{H}}, V_{\mathrm{G},n}^{\mathrm{L}}, T_m, t_j) - \Delta V_{\mathrm{th}}(V_{\mathrm{G},n}^{\mathrm{H}}, V_{\mathrm{G},n}^{\mathrm{L}}, T_m, t_j)|. \quad (5.10)$$

If the score value was too large, the optimizer created N new sets of parameters $S_1, S_2, ...S_N$. In each set S_i one parameter P_i was varied by adding a small value ΔP_i, while the other parameters remained unchanged.

$$S_i = \{P_1, P_2, ..., P_{i-1}, P_i + \Delta P_i, P_{i+1}, ..., P_N\},\ i\epsilon\{1, 2, ...N\} \quad (5.11)$$

For each of these parameter sets, a simulation was carried out and a score value was calculated in the same way as for the initial guess. Based on the resulting N score values $V_{\mathrm{s},1}, V_{\mathrm{s},2}, ...V_{\mathrm{s},N}$, a constrained nonlinear optimization algorithm [39] determined a new set of parameters S_{new} which is expected to yield an improved score value. A new iteration was started by continuing with this set of parameters S_{new} and calculating the new threshold voltage shift $\Delta V_{\mathrm{th}}(V_{\mathrm{G}}^{\mathrm{H}}, V_{\mathrm{G}}^{\mathrm{L}}, T)$. Usually, the progress of the score and of the corresponding simulation results is monitored during the optimization. Optimizations with undesired trends can be avoided with a modification of the parameter constraints.

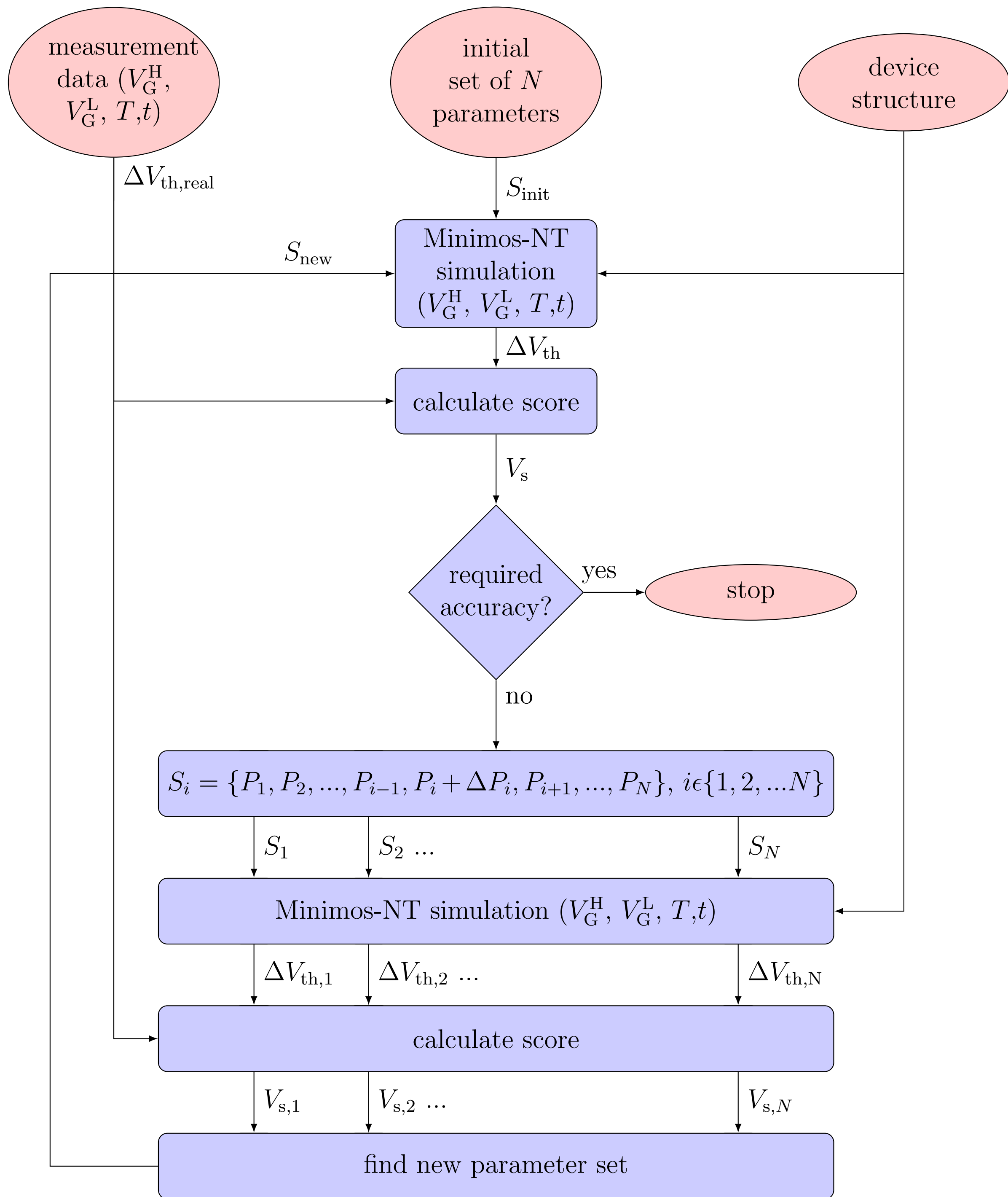

Figure 5.7: Scheme of the threshold voltage optimization described in Section 5.4.

Parameter	Value	Unit	Parameter	Value	Unit
D_{NMP}	1×10^{20}	cm^{-3}			
$\overline{E}_{\mathrm{t}}$	-1.0436	eV	$\sigma_{E_{\mathrm{t}}}$	0.1564	eV
$\overline{E}_{\mathrm{t}}'$	-0.3440	eV	$\sigma_{E_{\mathrm{t}'}}$	0.4248	eV
$\overline{\varepsilon}_{\mathrm{T2}'}$	0.6992	eV	$\sigma_{\varepsilon_{\mathrm{T2}'}}$	0.2622	eV
$\overline{R}_{12'}$	0.6048	1	$\sigma_{R_{12'}}$	0.4724	1
$\overline{S}_{12'}\hbar\omega$	2.3007	eV	$\sigma_{S_{12'}\hbar\omega}$	1.8024	eV
$\overline{R}_{1'2}$	0.5004	1	$\sigma_{R_{1'2}}$	0.3388	1
$\overline{S}_{1'2}\hbar\omega$	0.7197	eV	$\sigma_{S_{1'2}\hbar\omega}$	0.8035	eV
$\overline{\varepsilon}_{1'1}$	0.4042	eV	$\sigma_{\varepsilon_{1'1}}$	0.1972	eV
$\overline{\varepsilon}_{2'2}$	0.4047	eV	$\sigma_{\varepsilon_{2'2}}$	0.3064	eV
σ_0	2.6886×10^{-19}	m^2			
D_{DW}	5.2466×10^{12}	cm^{-2}			
$\overline{V}_{\mathrm{B}}$	0.0183	eV	$\sigma_{V_{\mathrm{B}}}$	0.2674	eV
$\overline{V}_{\mathrm{AB}}$	2.4128	eV	$\sigma_{V_{\mathrm{AB}}}$	0.8158	eV
$\overline{\gamma}$	6.4928×10^{-10}	m	σ_{γ}	9.7171×10^{-11}	m
ν_0	1×10^{13}	s^{-1}			

Table 5.6: Parameters of the NMP four state model and of the double well model, which were obtained by the optimization of the threshold voltage shift described in Section 5.4.

5.5 Results

The optimization described in Section 5.4, sought for the best match between the simulated and the measured threshold voltage shift. The resulting parameters of this optimization are listed in Table 5.6. In addition to the threshold voltage shift, the energy distribution of the traps in the band diagram and the CET map of this device are discussed in this section.

5.5.1 Threshold Voltage

The optimization result of the threshold voltage is shown in Figure 5.8. In accordance to the measurement data, no saturation of ΔV_{th} can be observed for the given stress time. Both, the temperature as well as the bias dependence are well reproduced. Due to the permanent component, which is described by the double well model, the recovery takes place at much larger time scales, compared to the threshold voltage shift during stress. This is in good agreement with the measurement data.

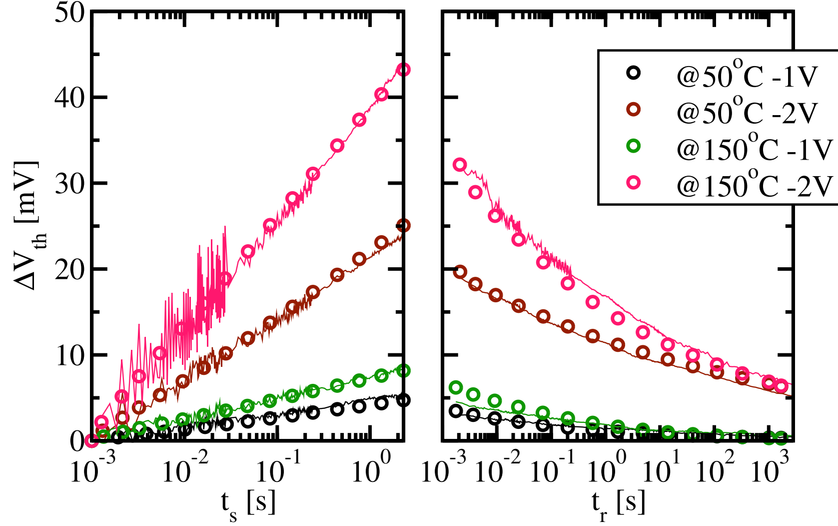

Figure 5.8: Threshold voltage degradation obtained by OTF measurements (lines) and the simulation result of the threshold voltage degradation (circles) modeled with the NMP four state model and the double well model. The parameters of the simulation are listed in Table 5.6. The results are in good agreement for all bias and temperature conditions.

5.5.2 Band Diagram

The charge of a trap of the NMP four state model is related to the trap level E_{t}, the Fermi level E_{F}, and the band edge energies E_{C} and E_{V} via the transitions rates (3.85) to (3.92). The involved effects will be discussed, based on the simulated band diagrams for $V_{\mathrm{G}}^{\mathrm{H}} = -2\,\mathrm{V}$, $V_{\mathrm{G}}^{\mathrm{H}} = -0.34\,\mathrm{V}$, and $T = 50°\mathrm{C}$ at different times. The double well model is not linked to the quantities of band diagrams and will not be considered in this context. Figure 5.9 shows the band diagram for $V_{\mathrm{G}}^{\mathrm{H}}$ and $V_{\mathrm{G}}^{\mathrm{L}}$ without any traps. The interface between the substrate and the oxide is at $x = 0\,\mathrm{nm}$ and, the interface between the oxide and the gate is at $x = 1.4\,\mathrm{nm}$. Significant times, at which the band diagram together with 600 randomly selected traps of the NMP four state model are shown, will be discussed below.

1. The start of the simulation at $t = 1\,\mathrm{ps}$ represents the time point right before a stress is applied to the device (compare Figure 5.10 (left)). As explained in Section 2.2, it is assumed that $V_{\mathrm{G}}^{\mathrm{L}}$ was applied for a sufficiently long time, before the stress phase starts. Therefore, the equilibrium solution of the trap occupancies for $V_{\mathrm{G}}^{\mathrm{L}}$ was calculated initially. The resulting charges, are barrier independent and solely defined by E_{t}, E_{F}, and T. This is in agreement with the observed relation between charges and trap levels. According to the parameters of the Gaussian distribution of the trap levels (compare Table 5.6), most traps are located below the Fermi level and are initially in their neutral state. Traps which are substantially above the Fermi are already positively charged and therefore, can not capture a hole during the stress phase. As a consequence, they will not contributed to ΔV_{th}.

2. At $t = 2\,\text{ps}$, the first time point of the stress phase is simulated. The corresponding band profile is shown in Figure 5.10 (right). The applied gate voltage V_G^H changes the potential $\psi(x)$ and increases the electric field in the oxide substantially. The increased oxide field causes an increased of the trap levels, as described in Section 3.1.2. The new time constants of the traps are above 1 ps, and no change of the charges is observed.

3. The last time step of the stress phase is at $t = t_\text{s} = 2.296479\,s$. Those traps, which were shifted close to or above the Fermi level at $t = 2\,\text{ps}$, remained there during the whole stress phase. Depending on their energy barriers, their charge was increased, which has resulted in a threshold voltage shift. As shown in Figure 5.11 (left), there are still many neutral traps, even above E_F. For larger stress times t_s they can be charged, depending on their time constants and would cause further degradation. This agrees well with the measurement data, as ΔV_th does not saturate during the stress time t_r due to the wide spread distribution of the time constants.

4. The first time step of the recovery phase can only be measured with a minimum delay Δt_delay after $t = t_\text{r}$. Figure 5.11 (right), shows the first recovery time point at $t = 2.298589\,\text{s}$, which corresponds to $\Delta t_\text{delay} \approx 2.11\,\text{ms}$. At this time point the gate voltage is switched back to V_G^L and the initial energy levels are obtained again. Due to the delay, all traps with emission time constants smaller than Δt_delay have already recovered.

5. The stress/recovery phase ends at $t = t_\text{s} + t_\text{r} = 2833\,\text{s}$. During the recovery phase the conditions remained constant, and almost all traps with $E_\text{t} < E_\text{F}$ are discharged, according to their emission time constants. As shown in Figure 5.12, there are still positively charged traps, even substantially below E_F. Obviously, their capture time constants during stress were much shorter than their emission time constants during the recovery phase.

5.5.3 CET Map

CET maps, described in Section 2.2.4, comprise the capture and emission time constants of traps, weighted by their charge difference between V_G^L and V_G^H for equilibrium. This difference is described by the equilibrium occupancy difference a, which is defined using the occupation probability p_2 (compare Section 3.3.3) as [9]

$$a = p_2^\text{H}(t \to \infty) - p_2^\text{L}(t \to \infty). \tag{5.12}$$

The occupation probabilities for equilibrium at stress voltage ($p_2^\text{H}(t \to \infty)$) and at recovery voltage ($p_2^\text{L}(t \to \infty)$) can be expressed using the capture and emission time constants

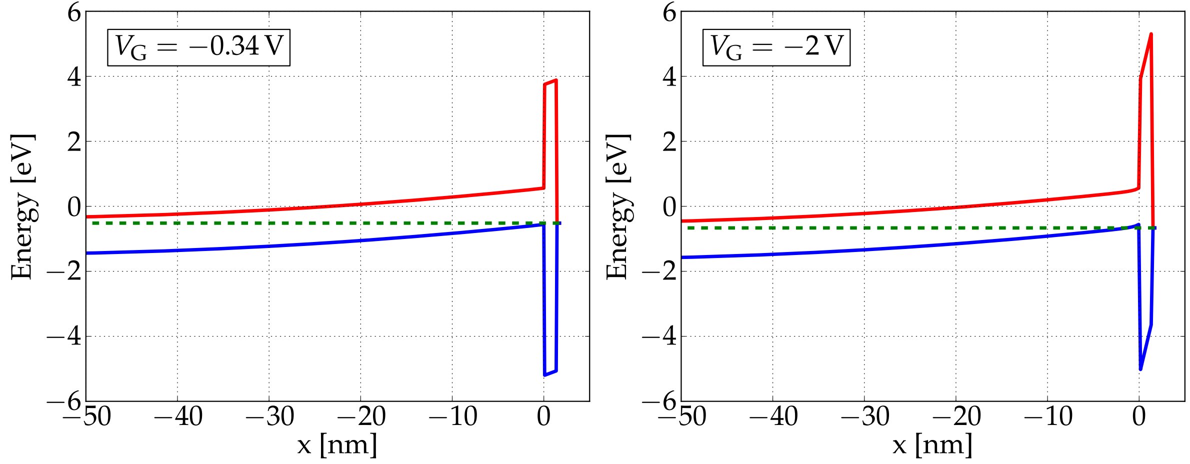

Figure 5.9: Band diagram for $V_G = -0.34$ V (left) and $V_G = -2$ V (right). The valance band edge (blue line), the conduction band edge (red line), and the Fermi level (dashed green line) are shown. As the Fermi level is already close to the valence band edge for V_G^L, a further increase of the gate voltage results in a strong increase of the electric field in the oxide but only in a small change of the surface potential.

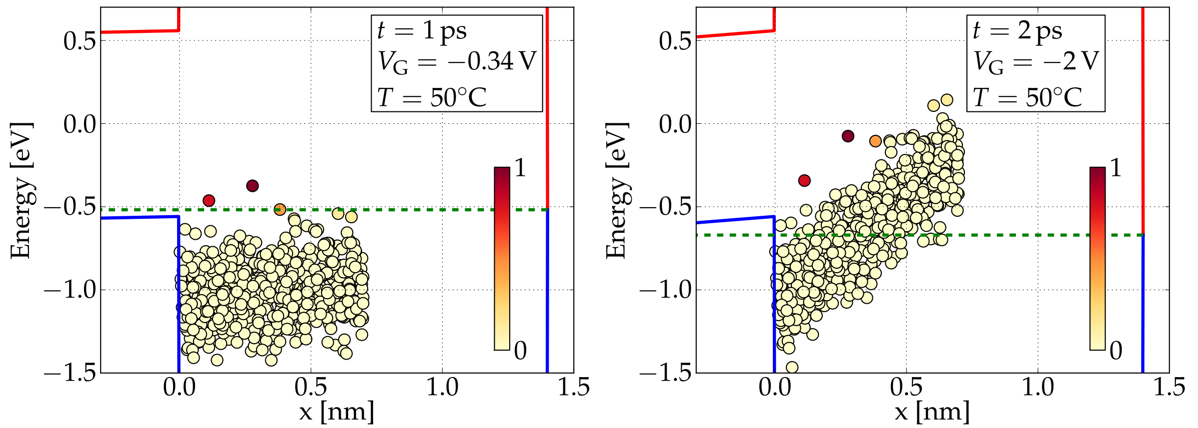

Figure 5.10: The same band diagrams as in Figure 5.9 but focused on the oxide. Additionally randomly selected traps of the NMP four state model are shown. The circles represent traps according to their position x_t and their trap level E_t. The color of the traps indicates their charge at the given time. Neutral traps are yellow (0) and charged traps are dark red (1). The charge of the traps at the initial equilibrium solution at $t = 1$ ps and $V_G = -0.34$ V (left) is solely determined by E_t, E_F, and T. At the next time step at $t = 2$ ps and $V_G = -2$ V (right), the increase of the gate voltage causes an increase of the electric field in the oxide, which results in an upward shift of the trap levels.

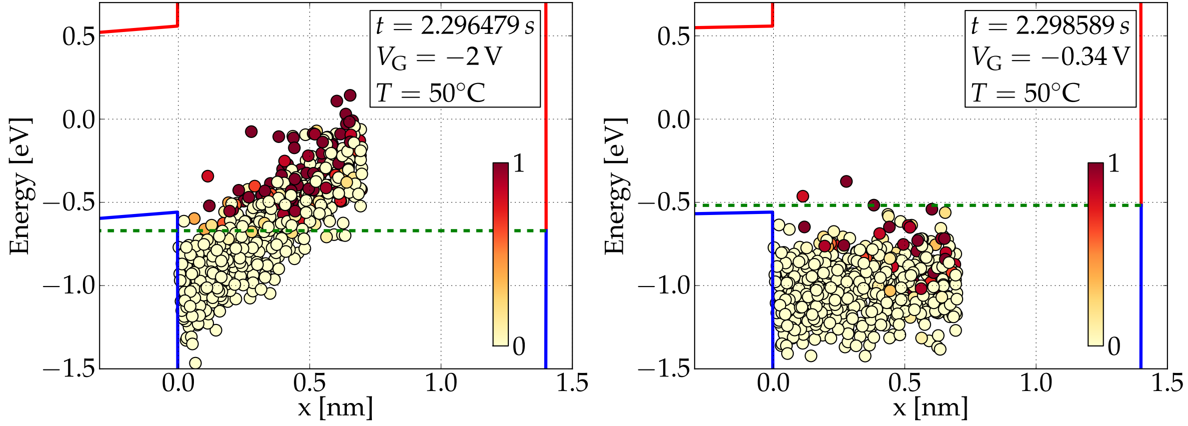

Figure 5.11: The same as in Figure 5.10 but for $t = t_s = 2.296479\,s$ and $V_G = -2\,V$ (left) and the next time step about 2.11 ms later with $V_G = -0.34\,V$ (right). At the end of the stress phase at $t = t_s$, some traps above the Fermi level are positively charged, according to their capture time constants. The first time point of the recovery phase is recorded with a measurement delay $\Delta t_{delay} \approx 2.11\,ms$. Traps with $\tau_e < \Delta t_{delay}$ are already discharged at $t = t_r + \Delta t_{delay}$.

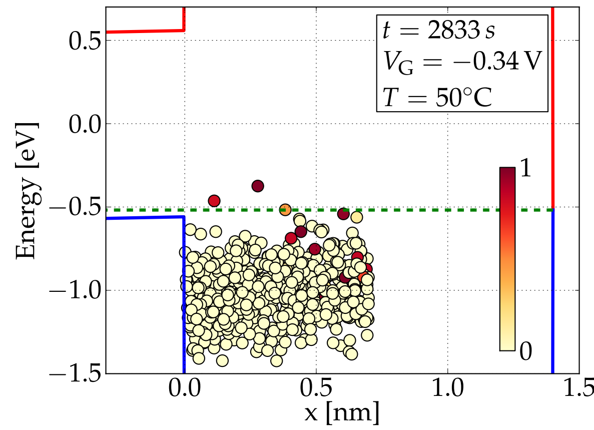

Figure 5.12: Same as in Figure 5.10 but with $t = t_s + t_r$ and $V_G = -0.34\,V$. Most traps with $E_t < E_F$ are in their neutral states, but those with $\tau_e > t_s + t_r$ are still positively charged.

at stress voltage ($\tau_\mathrm{c}^\mathrm{H}$, $\tau_\mathrm{e}^\mathrm{H}$) and at recovery voltage ($\tau_\mathrm{c}^\mathrm{L}$, $\tau_\mathrm{e}^\mathrm{L}$) [9],

$$p_2^\mathrm{L}(t \to \infty) = \frac{\tau_\mathrm{e}^\mathrm{L}}{\tau_\mathrm{e}^\mathrm{L} + \tau_\mathrm{c}^\mathrm{L}} \tag{5.13}$$

$$p_2^\mathrm{H}(t \to \infty) = \frac{\tau_\mathrm{e}^\mathrm{H}}{\tau_\mathrm{e}^\mathrm{H} + \tau_\mathrm{c}^\mathrm{H}}. \tag{5.14}$$

Thereby the resulting equilibrium occupancy difference [9]

$$a = \frac{\tau_\mathrm{e}^\mathrm{H}}{\tau_\mathrm{e}^\mathrm{H} + \tau_\mathrm{c}^\mathrm{H}} - \frac{\tau_\mathrm{e}^\mathrm{L}}{\tau_\mathrm{e}^\mathrm{L} + \tau_\mathrm{c}^\mathrm{L}} \tag{5.15}$$

accounts for the fact that a trap only contributes to the threshold voltage shift, if its charge can be different for V_G^H and V_G^L. The equilibrium occupation difference of each of these traps can be convoluted with a small two-dimensional Gaussian distribution. The normalized sum of the resulting Gaussian distributions, plotted as a function of $\tau_\mathrm{c}^\mathrm{H}$ and $\tau_\mathrm{e}^\mathrm{L}$ yields the CET map for V_G^H and V_G^L.

Figures 5.13 and 5.14 show CET maps, which were generated based on the traps of the NMP four state model with the parameters as listed in Table 5.6. The CET maps reveal a large distribution of time constants for different temperatures and stress voltages. For increasing stress voltages the distribution of the capture time constants broadens towards lower and higher $\tau_\mathrm{c}^\mathrm{H}$ equally. Both, the distribution of $\tau_\mathrm{c}^\mathrm{L}$ and of $\tau_\mathrm{e}^\mathrm{H}$ appears to shift towards lower values for increasing temperatures. These dependences will be discussed in detail in Section 6.1.

5.6 Conclusions

A threshold voltage shift was simulated using the NMP four state model together with the double well model. The corresponding model parameters were optimized and the resulting degradation was in good agreement with the measured threshold voltage shift of a pMOSFET at different stress voltages and temperatures. Simulated band diagrams, together with the traps of the NMP four state model, confirmed the correct modeling of a non-saturating degradation. Finally, CET maps were simulated which revealed a large distribution of time constants. Again, this is in agreement with the non-saturating degradation.

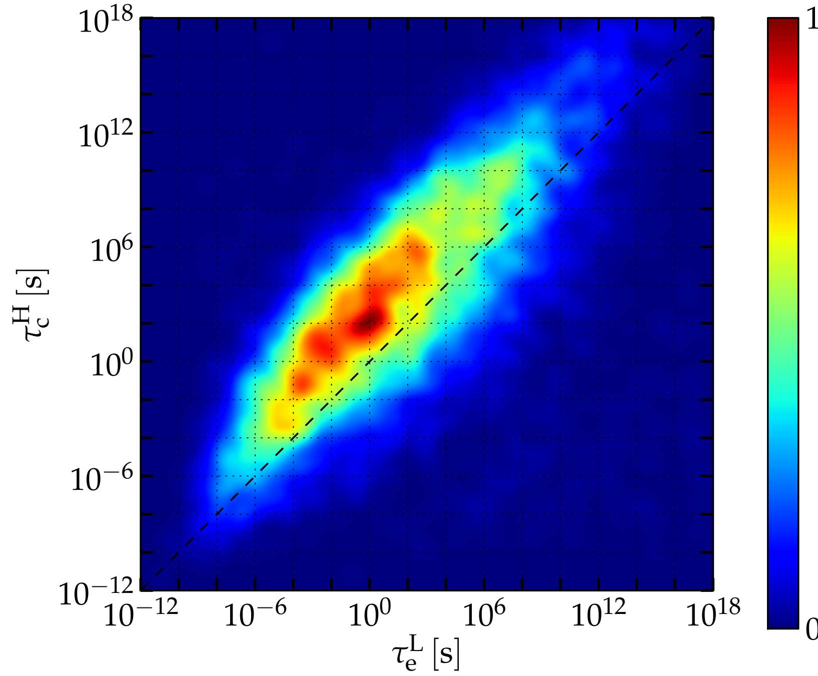

Figure 5.13: CET map simulated at $T = 50°C$, $V_G^L = -0.5\,V$ and $V_G^H = -2\,V$ considering all traps of the NMP four state model with the parameters of the threshold voltage optimization (compare Table 5.6).

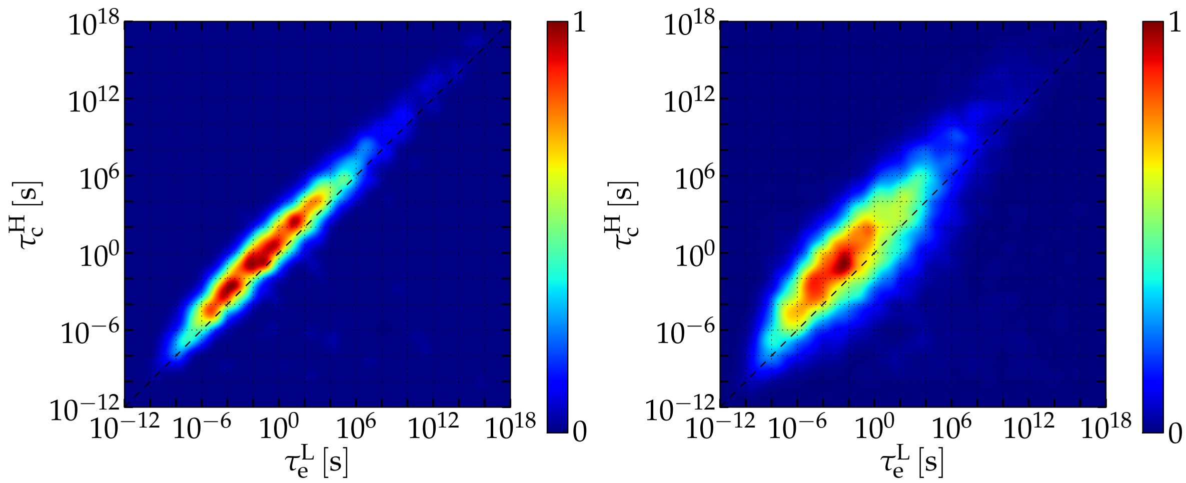

Figure 5.14: CET maps simulated with $V_G^H = -1\,V$ (left) and $V_G^H = -2\,V$ (right), both with $V_G^L = -0.5\,V$ and $T = 150°C$. For increasing stress voltages the distribution of the capture time constants broadens towards lower and higher τ_c^H equally. Both, the distribution of τ_c^H and of τ_e^L appears to shift towards lower values for increasing temperatures.

CHAPTER 6 CET Map Considerations

In this chapter simulated CET maps will be analyzed with regard to their bias and temperature dependence and the electron-phonon coupling regimes of the transitions involved. Furthermore, a discussion about the equilibrium occupancy difference of simple NMP transitions and the consequences for CET maps will be presented.

6.1 NMP Four State Model

The simulation of CET maps allows for a detailed study of the contributing traps and their equilibrium occupancy difference. In the following this will be done based on the trap parameters obtained in Section 5.5.

6.1.1 Bias Dependence

In order to investigate the bias dependence, CET maps are simulated for two different stress voltages $V_{\mathrm{G},1}^{\mathrm{H}}$ and $V_{\mathrm{G},2}^{\mathrm{H}}$. The resulting CET maps are shown in Figure 6.1, together with 400 randomly selected traps of the NMP four state model. Nearly all traps show smaller capture time constants at higher gate voltages. Their emission time constants remain the same for both CET maps, as they both were simulated with the same $V_{\mathrm{G}}^{\mathrm{L}}$. Therefore, the trap density is shifted towards lower τ_{c} for increasing $V_{\mathrm{G}}^{\mathrm{H}}$ and one might expect the CET map to follow this trend. But, the density $g(\tau_{\mathrm{c}}^{\mathrm{H}}, \tau_{\mathrm{e}}^{\mathrm{L}})$ of the simulated CET maps (compare Figure 5.14) equally broadens towards lower and higher $\tau_{\mathrm{c}}^{\mathrm{H}}$ for increasing gate voltages. Differences between a trap density and the density $g(\tau_{\mathrm{c}}^{\mathrm{H}}, \tau_{\mathrm{e}}^{\mathrm{L}})$ of a CET map can only be induced by the equilibrium occupancy difference a, described in Section 5.5.3. For verification, the randomly selected traps in Figure 6.1 are colored according to their equilibrium occupancy difference. The above observations indicate that the bias dependence of CET maps is mainly governed by the equilibrium occupancy difference. As it will be shown in Section 6.2.5, an equal broadening of the equilibrium occupancy difference towards lower and higher $\tau_{\mathrm{c}}^{\mathrm{H}}$ is inherent to NMP transitions. The shift of capture time constants and the relation to the regime of electron-phonon coupling

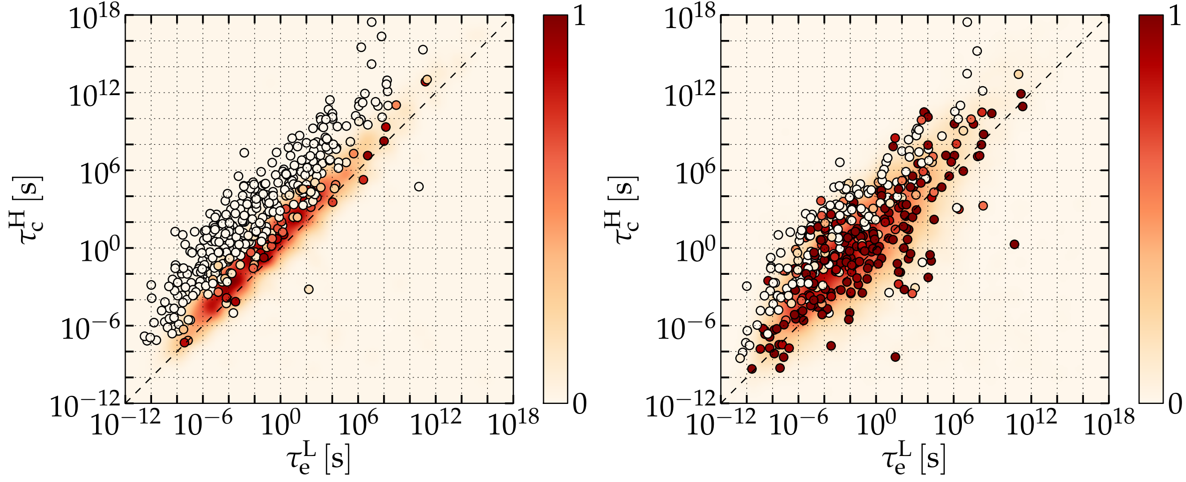

Figure 6.1: CET maps simulated with $V_G^H = -1\,V$ (left), and with $V_G^H = -2\,V$ (right), both at $V_G^L = -0.5\,V$ and $T = 150°C$. The color of the 400 randomly selected traps indicates their equilibrium occupancy difference. The color bar applies to both, the normalized density of the CET map and to the equilibrium occupancy difference of the traps. Nearly all traps are shifted towards lower τ_c^H for increasing V_G, but the equilibrium occupancy difference broadens towards higher and lower τ_c^H.

will be discussed in Section 6.1.3.

The threshold voltage shift $\Delta V_{th}(t_s, t_r)$ can be calculated from $g(\tau_c^H, \tau_e^L)$ using equation (2.5). The area of the integral is defined by t_s and t_r as shown in Figure 6.2. The number of traps with a high equilibrium occupancy difference increases in this area for higher gate voltages, which results in a larger threshold voltage shift, as expected.

6.1.2 Temperature Dependence

Similar to the previous section, the investigation of the temperature dependence of CET maps will be based on the simulation results of Section 5.5. Figure 6.3 shows two simulated CET maps for different temperatures, together with 400 randomly selected traps of the NMP four state model. All time constants decrease with increasing temperature. This can be explained with the help of the transitions rates given by equation (3.44) to (3.47). The temperature enters these rates via β in the Boltzmann factor. Thus, increasing temperatures cause increasing transitions rates, which results in decreasing time constants. The number of traps with a high equilibrium occupancy difference show an increase in the integral area defined by t_s and t_r (compare Section 6.1.1) for higher temperatures, and the resulting increase of ΔV_{th} is in agreement with measurements.

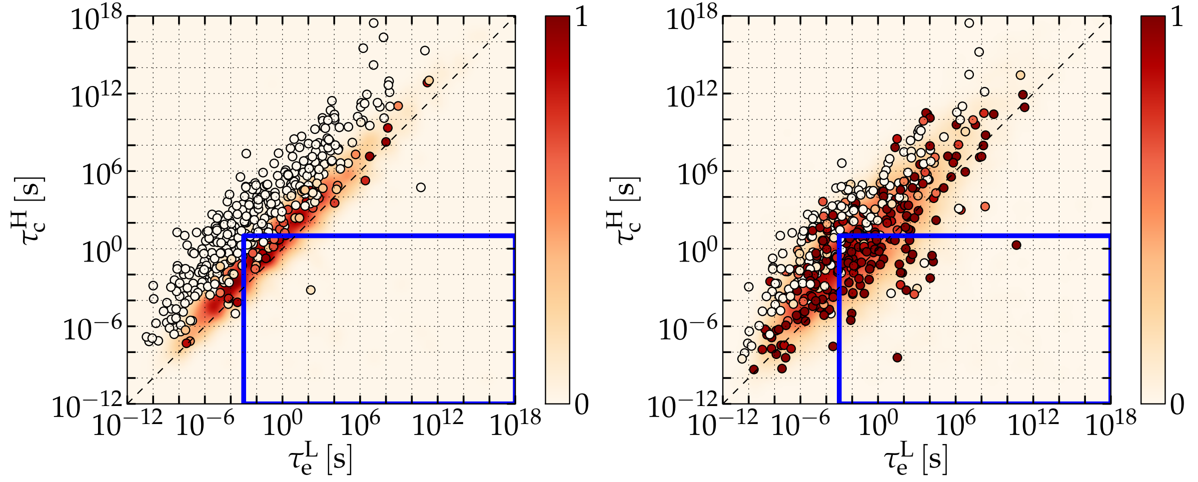

Figure 6.2: Same as in Figure 6.1. Additionally the blue rectangle indicates the area of CET maps, which enters the integral to calculate ΔV_{th}. The case of $t_s = 10\,s$ and $t_r = 1\,ms$ is shown. The number of traps with a high equilibrium occupancy difference in the area which defines ΔV_{th} increases for higher V_G.

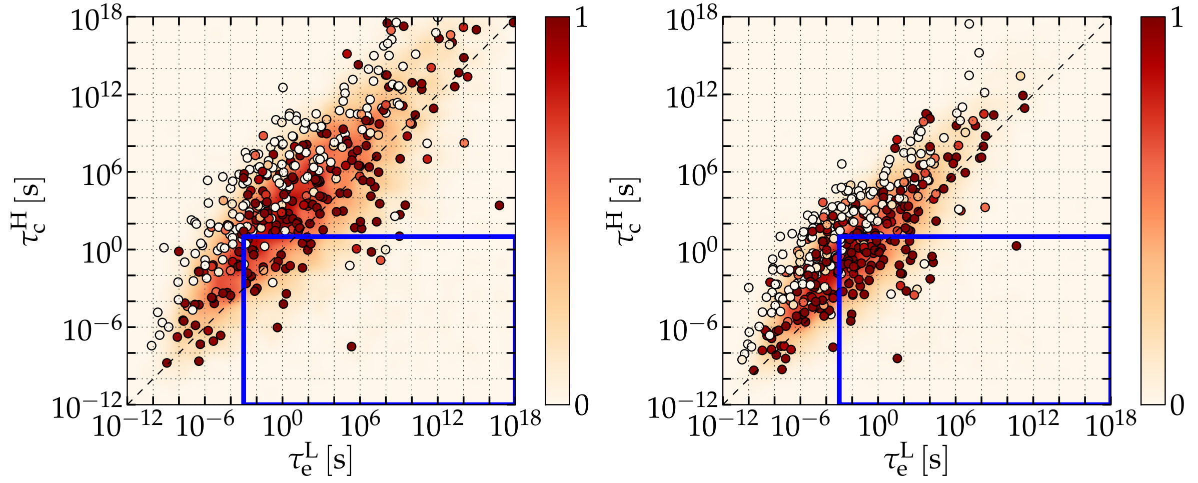

Figure 6.3: Same as in Figure 6.1 but with $T = 50°C$ (left), and with $T = 150°C$ (right) and $V_G^L = -0.5\,V$ and $V_G^H = -2\,V$. A decrease of all time constants of the traps can be observed for higher temperatures. The blue rectangle indicates the area of CET maps, which enters the integral to calculate ΔV_{th}. The case of $t_s = 10\,s$ and $t_r = 1\,ms$ is shown. The number of traps with a high equilibrium occupancy difference in the area which defines ΔV_{th}, increases for higher temperatures.

6.1.3 Negative Weak Electron-Phonon Coupling

As explained in Section 3.1.7, the energy barrier ε_{ij} decreases with an increasing electric field F in the oxide, if the trap is in the regime of strong or positive weak electron-phonon coupling. The resulting decrease of the capture time constants was observed for the majority of traps in the simulated CET maps (compare Section 6.1.1). However, the simulations revealed a few traps whose τ_c^H increase for increasing F. Apparently they are in the regime of negative weak electron-phonon coupling for the observed voltages V_G^L and V_G^H. The region in CET maps, where such traps can be found, is analyzed based on the parameters of Section 5.5. Figure 6.4 shows the density of traps in the negative weak electron-phonon coupling regime, weighted by $\tau_c^H - \tau_c^L$. Apparently all of them fulfill the condition $\tau_c^H > \tau_e^L$, a fact which will be discussed later in Section 6.2.4.

For an exemplary trap, which is marked with a white circle in Figure 6.4, the time constants are shown in Figure 6.5 (left), while the configuration coordinate diagram is depicted in Figure 6.6. The dominant transition path for a hole capture of this trap is found to be from state 1 to 2 via 1′. The rates which are involved in the transition from state 1′ to 2 are shown in Figure 6.4 (right). In accordance with the configuration coordinate diagram, the rate $k_{1'2}^{VB}$ has a reversal point at $V_G \approx -0.8\,V$. For higher gate voltages the rate $k_{1'2}^{VB}$ shows a strong decrease. This reversal point can be identified with the limit between strong electron-phonon coupling and negative weak electron-phonon coupling, as described in Section 3.1.7. The consequence is an increasing capture time for increasing gate voltages, which makes traps move "upwards" in CET maps (compare Figure 6.4). For the exemplary trap, this trend stops above $V_G \approx -1.8\,V$. At such large voltages, the transition from state 1′ to 2 is governed by transitions between the conduction band and the oxide trap, instead of the valence band and the oxide band (compare transition rate $k_{1'2}$ in Figure 6.5 (right)).

In the regions where traps with transitions in the regime of negative weak electron-phonon coupling are observed, the corresponding CET maps show a low density $g(\tau_c^H, \tau_e^L)$ (compare Figures 6.4 and 5.14). Therefore such traps give a minor contribution to the threshold voltage shift. In addition to the low density of such traps, this can be traced back to a correlation of the ratio of their time constants and the equilibrium occupancy difference, as will be discussed in the following section.

6.2 Equilibrium Occupancy Difference

The contribution of a trap with the time constants τ_c^H and τ_e^L to a CET map depends on its equilibrium occupancy difference a, as described in Section 5.5.3. Due to the relations of the time constants in equations (5.13) and (5.14), it is difficult to make general statements about the equilibrium occupancy difference for traps of the NMP four state model. Therefore, the following discussion about the equilibrium occupancy difference will be limited to simple NMP transitions.

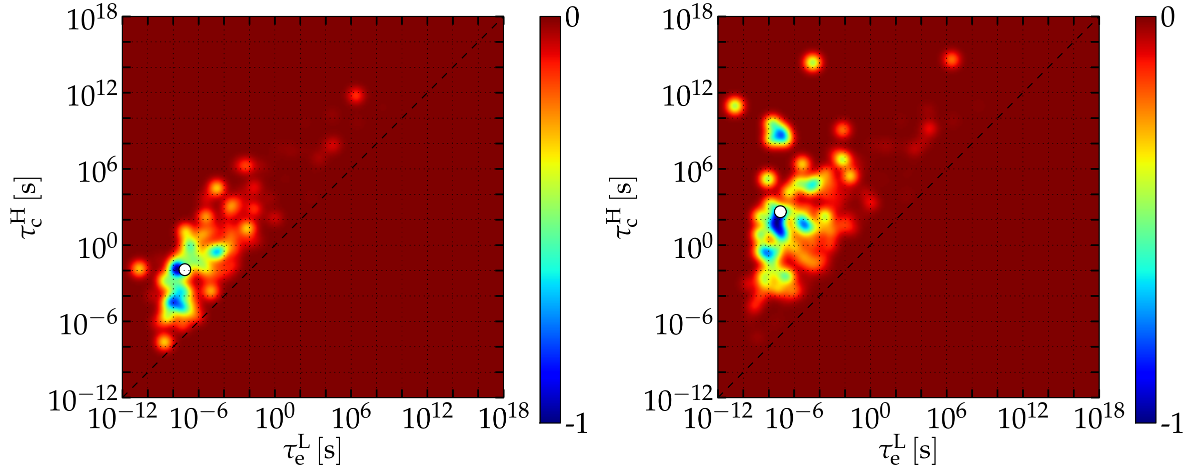

Figure 6.4: Density of traps whose transitions are in the regime of weak electron-phonon coupling between $V_G^L = -1\,\mathrm{V}$ and $V_G^H = -2\,\mathrm{V}$, weighted by $\tau_c^H - \tau_c^L$. The situation is shown for $V_G^H = -1\,\mathrm{V}$ (left) and $V_G^H = -2\,\mathrm{V}$ (right), both at $T = 150°\mathrm{C}$ and $V_G^L = -0.5\,\mathrm{V}$. The white circle marks an exemplary trap, which is discussed in Section 6.1.3.

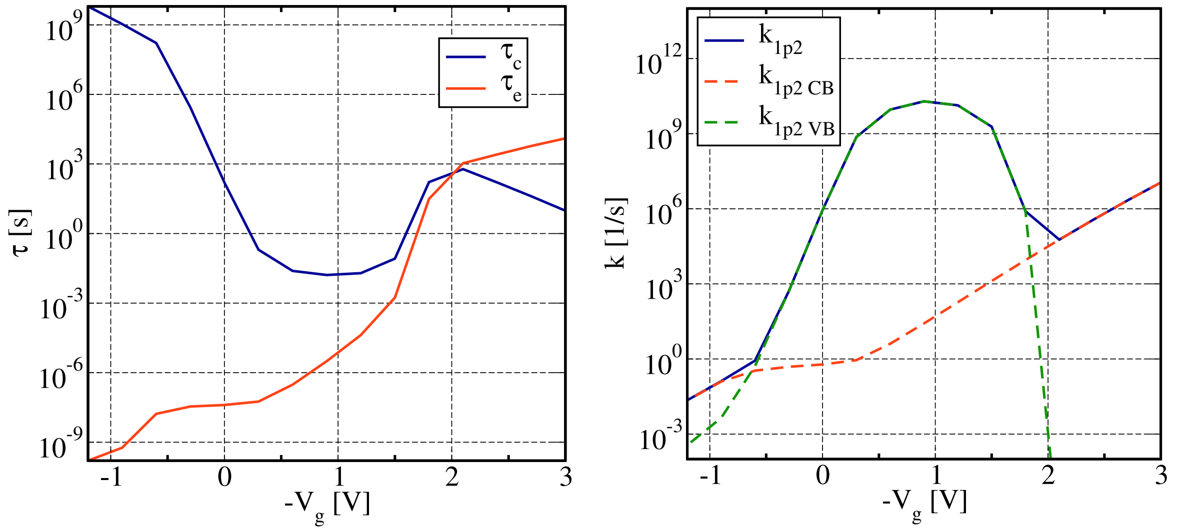

Figure 6.5: The bias dependence of the capture and emission time constants of a trap which shows weak electron-phonon coupling (right) and the corresponding rates from state 1′ to 2 (right).

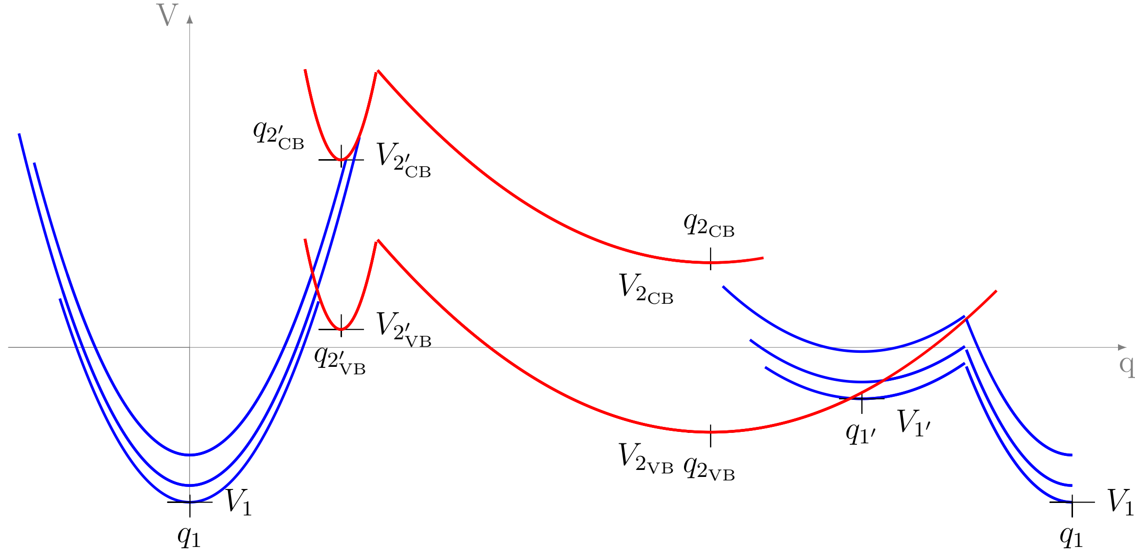

Figure 6.6: Configuration coordinate diagram of an exemplary trap, as described in Section 6.1.3. The configuration is plotted for $V_{\mathrm{G}} = -0.3$ (lower), -0.9 (middle), and $-1.8\,\mathrm{V}$ (upper blue line). In this voltage range, weak electron-phonon coupling can be observed between states $1'$ and 2.

6.2.1 General Expression for NMP Transitions

In the following, an NMP transition (compare Section 3.1) with a neutral state 1 and a positive state 2 is assumed. For simplicity, only transitions between the valance band of the substrate and the oxide trap will be considered. With the transition rates of equation (3.53) and (3.54), and the hole concentrations p^{H} and p^{L} for $V_{\mathrm{G}}^{\mathrm{H}}$ and $V_{\mathrm{G}}^{\mathrm{L}}$, respectively, the time constants for this system are given by

$$\tau_{\mathrm{c}}^{\mathrm{L}} = \frac{1}{p^{\mathrm{L}} v_{\mathrm{th,p}} \sigma_{0,\mathrm{p}} \vartheta_{\mathrm{p}}} \mathrm{e}^{\beta \varepsilon_{12}^{\mathrm{L}}} \tag{6.1}$$

$$\tau_{\mathrm{c}}^{\mathrm{H}} = \frac{1}{p^{\mathrm{H}} v_{\mathrm{th,p}} \sigma_{0,\mathrm{p}} \vartheta_{\mathrm{p}}} \mathrm{e}^{\beta \varepsilon_{12}^{\mathrm{H}}} \tag{6.2}$$

$$\tau_{\mathrm{e}}^{\mathrm{L}} = \frac{1}{p^{\mathrm{L}} v_{\mathrm{th,p}} \sigma_{0,\mathrm{p}} \vartheta_{\mathrm{p}}} \mathrm{e}^{\beta (\varepsilon_{12}^{\mathrm{L}} - E_{\mathrm{F}} + E_{\mathrm{t}})} \tag{6.3}$$

$$\tau_{\mathrm{e}}^{\mathrm{H}} = \frac{1}{p^{\mathrm{H}} v_{\mathrm{th,p}} \sigma_{0,\mathrm{p}} \vartheta_{\mathrm{p}}} \mathrm{e}^{\beta (\varepsilon_{12}^{\mathrm{H}} - E_{\mathrm{F}} + E_{\mathrm{t}})}. \tag{6.4}$$

Using these expressions, the equilibrium occupancy difference, which was defined in Section 5.5.3, can be written as

$$a = \frac{1}{1 + \mathrm{e}^{-\beta\left(-E_{\mathrm{F}}^{\mathrm{H}} + E_{\mathrm{t}}^{\mathrm{H}}\right)}} - \frac{1}{1 + \mathrm{e}^{-\beta\left(-E_{\mathrm{F}}^{\mathrm{L}} + E_{\mathrm{t}}^{\mathrm{L}}\right)}}. \tag{6.5}$$

This equation reveals that the equilibrium occupancy difference is determined by the Fermi levels $E_{\mathrm{F}}^{\mathrm{H}}$ and $E_{\mathrm{F}}^{\mathrm{L}}$ and the trap energies $E_{\mathrm{t}}^{\mathrm{H}}$ and $E_{\mathrm{t}}^{\mathrm{L}}$ at the gate voltages $V_{\mathrm{G}}^{\mathrm{L}}$ and $V_{\mathrm{G}}^{\mathrm{H}}$, respectively, as well as by the temperature T.

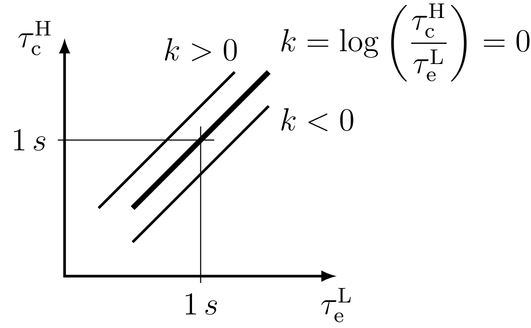

Figure 6.7: A schematic CET map. Traps with the same k factor share the same lines.

6.2.2 Relation to Time Constants

The discussion of this chapter can be motivated by the following considerations. The equilibrium occupancy difference of an NMP transition is mainly governed by E_t^H, E_t^L, and $E_F^H \approx E_F^L$, where the difference $E_t^H - E_t^L$ is determined by the shift of the oxide field F and the trap position x_t. Clearly, the equilibrium occupancy difference has its maximum for

$$\overline{E_t} = \frac{E_t^H + E_t^L}{2} \approx E_F^H \approx E_F^L. \tag{6.6}$$

For a certain energy difference $E_t^H - E_t^L$, a shift of $\overline{E_t}$ away from the Fermi levels causes a decrease of the equilibrium occupancy difference. Furthermore, the values of $\overline{E_t}$ and the Fermi levels are strongly related to the time constants. The larger the difference between the capture and emission time constants gets, the smaller will be the resulting equilibrium occupancy difference. The energy barriers ε_{12} and ε_{21} are unimportant for these considerations. For example, all NMP transitions with $\tau_c^H = \tau_e^L$ will have the same equilibrium occupancy difference, and will contribute along the same line on a CET map. The corresponding barriers $\varepsilon_{12}^H = \varepsilon_{21}^L$ will only define the location along this line. This suggests a strong correlation of the time constants and the equilibrium occupancy difference, which in the following will be expressed on the basis of equation (6.5).

The factor k, which relates the time constants will turn out to be useful in this context. This factor is defined as

$$k = \log\left(\frac{\tau_c^H}{\tau_e^L}\right). \tag{6.7}$$

Traps with the same k are found along the same line on CET maps, as shown in Figure 6.7. In the following, the surface potential $\psi(x = 0)$ is assumed to be the same for V_G^L and V_G^H. This crude approximation can be justified because the considered gate voltages are near or above the threshold voltage. Using this "inversion approximation" the hole concentrations p^H and p^L are equal. Therefore, substituting the expressions for the time constants (6.2) and (6.3), the above equation yields

$$k = \beta(\varepsilon_{12}^H - \varepsilon_{12}^L + E_F^L - E_t^L). \tag{6.8}$$

With the intersection point difference ΔV_{IP} (compare Figure 6.8)

$$\Delta V_{\mathrm{IP}} = \varepsilon_{12}^{\mathrm{H}} + V_1^{\mathrm{H}} - V_1^{\mathrm{L}} - \varepsilon_{12}^{\mathrm{L}} \tag{6.9}$$

the factor k reads

$$k = \beta(\Delta V_{\mathrm{IP}} - V_1^{\mathrm{H}} + V_1^{\mathrm{L}} + E_{\mathrm{F}}^{\mathrm{L}} - E_{\mathrm{t}}^{\mathrm{L}}). \tag{6.10}$$

The discussion of Section 3.1.2 relates the gate voltage dependence of V_1 and E_{t}. An increase of E_{t} leads to an increase of V_1 by the same value, which results in

$$V_1^{\mathrm{H}} - V_1^{\mathrm{L}} = E_{\mathrm{t}}^{\mathrm{H}} - E_{\mathrm{t}}^{\mathrm{L}}. \tag{6.11}$$

Thus, the factor k can be rewritten as

$$k = \beta(\Delta V_{\mathrm{IP}} - E_{\mathrm{t}}^{\mathrm{H}} + E_{\mathrm{F}}^{\mathrm{L}}). \tag{6.12}$$

Using the inversion approximation, the Fermi levels can be expressed as

$$E_{\mathrm{F}}^{\mathrm{H}} \approx E_{\mathrm{F}}^{\mathrm{L}} = k\beta - \Delta V_{\mathrm{IP}} + E_{\mathrm{t}}^{\mathrm{H}} \tag{6.13}$$

and substituted in equation (6.5) to obtain

$$a = \frac{1}{1 + \mathrm{e}^{k - \beta \Delta E_{\mathrm{IP}}}} - \frac{1}{1 + \mathrm{e}^{k - \beta\left(\Delta E_{\mathrm{IP}} - E_{\mathrm{t}}^{\mathrm{H}} + E_{\mathrm{t}}^{\mathrm{L}}\right)}}. \tag{6.14}$$

With the difference of the electric field $\Delta F = F(V_{\mathrm{G}}^{\mathrm{H}}) - F(V_{\mathrm{G}}^{\mathrm{L}})$, and the considerations made in Section 3.1.2, the difference of the trap levels can be written as

$$E_{\mathrm{t}}^{\mathrm{H}} - E_{\mathrm{t}}^{\mathrm{L}} = q_0 x_{\mathrm{t}} \Delta F. \tag{6.15}$$

Substituting this expression in equation (6.14), the equilibrium occupancy difference reads

$$a = \frac{1}{1 + \mathrm{e}^{k - \beta \Delta E_{\mathrm{IP}}}} - \frac{1}{1 + \mathrm{e}^{k - \beta(\Delta E_{\mathrm{IP}} - q_0 x_{\mathrm{t}} \Delta F)}}. \tag{6.16}$$

Compared to the previous expression of the equilibrium occupancy (6.5), the equation (6.16) shows a correlation between the equilibrium occupancy difference of traps with similar ratio of time constants. This trend was observed in CET maps, which were based on simulations of the NMP four state model (compare Figure 5.13). So, even though the results of equations (6.5) and (6.16) are essentially the same, the latter better reflects the nature of the equilibrium occupancy difference. Furthermore, it allows to link $\tau_{\mathrm{c}}^{\mathrm{H}}$ and $\tau_{\mathrm{e}}^{\mathrm{L}}$ of a trap to its equilibrium occupancy difference with the help of reasonable approximations as will be shown in Section 6.2.6. The temperature dependence, the effect of ΔV_{IP}, and the dependence on F and x_{t} of equation (6.16) will be discussed in Sections 6.2.3, 6.2.4, and 6.2.5, respectively.

Figure 6.9 shows the values of the first and the second term of equation (6.16) and the resulting equilibrium occupancy difference for different k factors and constant ΔE_{IP} and ΔF.

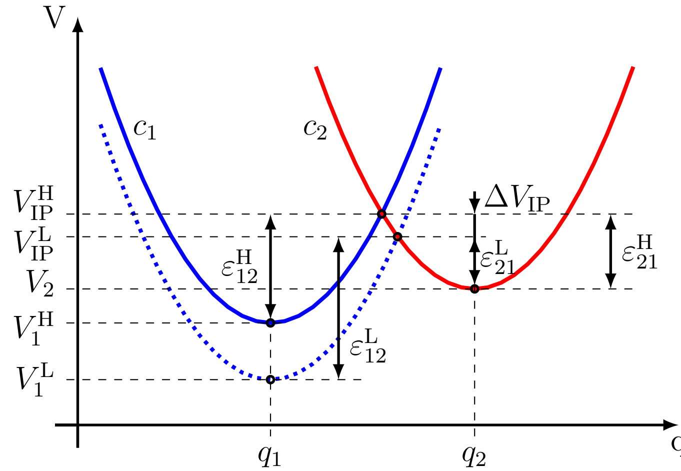

Figure 6.8: Configuration coordinate diagram of an NMP transition with a neutral state 1 and a positive state 2 for a low gate voltage $V_{\mathrm{G}}^{\mathrm{L}}$ (dotted blue line) and a hight gate voltage $V_{\mathrm{G}}^{\mathrm{H}}$ (solid blue line). The difference between the energy of the intersection points for those voltages can be identified as $\Delta V_{\mathrm{IP}} = \varepsilon_{12}^{\mathrm{H}} + V_1^{\mathrm{H}} - V_1^{\mathrm{L}} - \varepsilon_{12}^{\mathrm{L}}$.

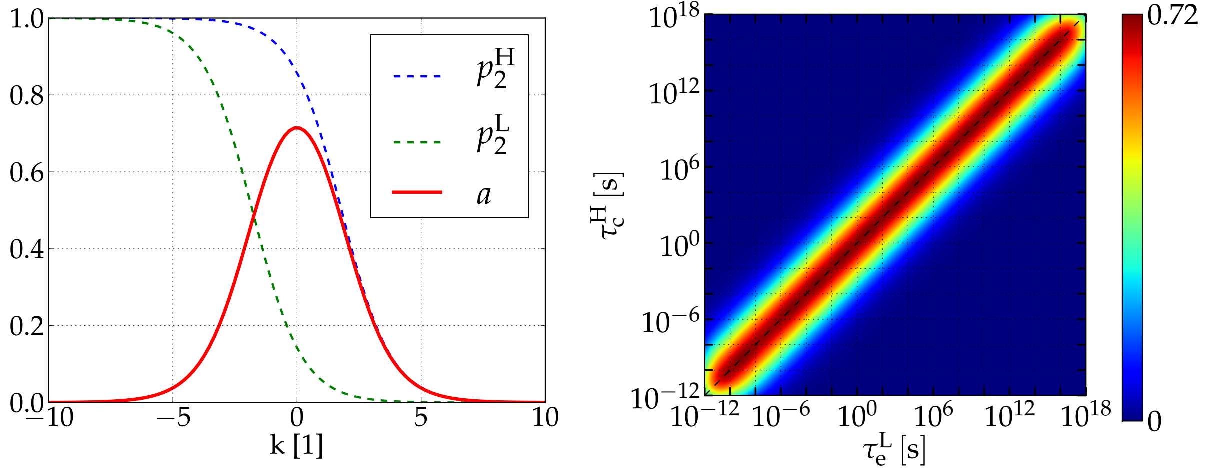

Figure 6.9: **Left**: The equilibrium occupancy difference a and the occupation probabilities p_2^{H} and p_2^{L} of state 2 for equilibrium as a function of k. The equation (6.16) was used with $\Delta V_{\mathrm{IP}} = 0.05\,\mathrm{eV}$, $q_0 x_{\mathrm{t}} \Delta F = 0.1\,\mathrm{eV}$, and $T = 50°\mathrm{C}$. **Right**: The equilibrium occupancy difference as a function of $\tau_{\mathrm{c}}^{\mathrm{H}}$ and $\tau_{\mathrm{e}}^{\mathrm{L}}$, calculated with equation (6.16) using $\Delta V_{\mathrm{IP}} = 0.05\,\mathrm{eV}$, $q_0 x_{\mathrm{t}} \Delta F = 0.1\,\mathrm{eV}$, and $T = 50°\mathrm{C}$. This figure corresponds to a CET map of traps whose time constants $\tau_{\mathrm{c}}^{\mathrm{H}}$ and $\tau_{\mathrm{e}}^{\mathrm{L}}$ are homogeneously distributed on a logarithmic scale.

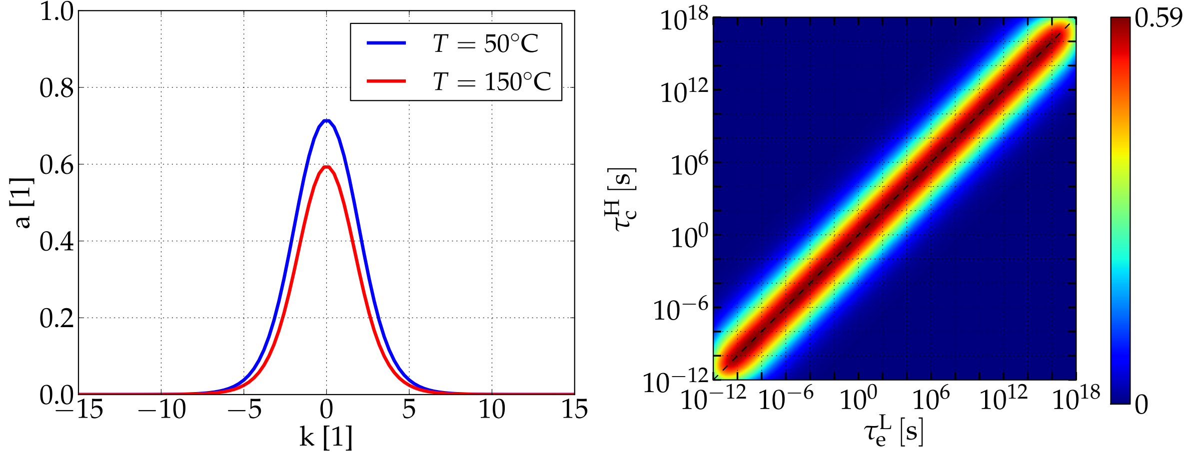

Figure 6.10: **Left**: The equilibrium occupancy difference a as a function of k for $T = 50°C$ (blue) and $T = 150°C$ (red). The equation (6.16) was used with $\Delta V_{IP} = 0.05\,eV$ and $q_0 x_t \Delta F = 0.1\,eV$. **Right**: The equilibrium occupancy difference as a function of τ_c^H and τ_e^L, calculated with equation (6.16) using $\Delta V_{IP} = 0.05\,eV$, $q_0 x_t \Delta F = 0.1\,eV$, and $T = 150°C$. The value range indicated by the color bar is lower, compared to the result for $T = 50°C$ in Figure 6.7. This figure corresponds to a CET map of traps whose time constants τ_c^H and τ_e^L are homogeneously distributed on a logarithmic scale.

6.2.3 Temperature Dependence

The temperature dependence enters equation (6.16) via $\beta = 1/(k_B T)$ in the Boltzmann factors. For increasing temperatures, the difference of the equilibrium occupancies $p_1 - p_2$ decreases, as higher temperature evens out the occupancies of the states. One has to keep in mind that for $T \to \infty$ the occupancies are $p_1 = p_2 = 0.5$, independent of the energies involved. Therefore, the resulting equilibrium occupancy becomes zero for $T \to \infty$. Calculations based on equation (6.16) for different temperatures confirm the expected temperature dependence (compare Figure 6.10).

6.2.4 Intersection Point Difference

The definition of the equilibrium occupancy difference implies two different gate voltages V_G^H and V_G^L, which results in two different electric fields in the oxide. The difference of these electric fields ΔF causes a difference of the intersection points ΔV_{IP}, depending of the trap position x_t. For a certain energy shift $q_0 x_t \Delta F$, the change of ΔV_{IP} depends on S_{12}, R_{12}, and E_{21}. This relation can be quantified by dV_{IP}/dF, where V_{IP} can be written as

$$V_{IP} = \varepsilon_{12} + V_1. \tag{6.17}$$

Based on the considerations in Section 3.1.2, the system energy of state 1 can be related to the oxide field by

$$V_1(F) = V_1(F=0) + q_0 x_\mathrm{t} F. \tag{6.18}$$

With the above expression, the derivative of (6.17) with respect to F reads

$$\frac{1}{q_0 x_\mathrm{t}} \frac{\mathrm{d}V_\mathrm{IP}}{\mathrm{d}F} = \frac{1}{q_0 x_\mathrm{t}} \frac{\mathrm{d}\varepsilon_{12}}{\mathrm{d}F} + 1. \tag{6.19}$$

As discussed in Section 3.1.7, the value of $\mathrm{d}\varepsilon_{12}/\mathrm{d}F$ is associated with the electron-phonon coupling regimes (compare equations (3.76), (3.79), and (3.82)). Therefore, the value of $\mathrm{d}V_\mathrm{IP}/\mathrm{d}F$ depends on the coupling regime of the NMP transition. The exact limits are listed below, together the limits obtained by the approximation

$$\frac{\mathrm{d}V_\mathrm{IP}}{\mathrm{d}F} \approx \frac{\Delta V_\mathrm{IP}}{\Delta F}. \tag{6.20}$$

- Strong electron-phonon coupling:

$$0 < \frac{1}{q_0 x_\mathrm{t}} \frac{\mathrm{d}V_\mathrm{IP}}{\mathrm{d}F} < 1 \tag{6.21}$$

$$0\,\mathrm{eV} < \Delta V_\mathrm{IP} < q_0 x_\mathrm{t} \Delta F \tag{6.22}$$

- Positive weak electron-phonon coupling:

$$\frac{1}{q_0 x_\mathrm{t}} \frac{\mathrm{d}V_\mathrm{IP}}{\mathrm{d}F} < 0 \tag{6.23}$$

$$\Delta V_\mathrm{IP} < 0\,\mathrm{eV} \tag{6.24}$$

- Negative weak electron-phonon coupling:

$$\frac{1}{q_0 x_\mathrm{t}} \frac{\mathrm{d}V_\mathrm{IP}}{\mathrm{d}F} > 1 \tag{6.25}$$

$$\Delta V_\mathrm{IP} > q_0 x_\mathrm{t} \Delta F \tag{6.26}$$

For a given trap distance x_t and ΔF, the value of ΔV_IP can be associated with a coupling regime, using the findings above. Inspection of equation (6.16) shows that for lower differences of the intersection points, the distribution of a shifts towards lower k, and for larger differences it shifts towards larger k. The Figures 6.11 and 6.12 show the results for the upper and the lower limit of the strong electron-phonon coupling regime, respectively. Additionally an example for positive weak electron-phonon coupling and negative weak electron-phonon coupling is depicted in Figures 6.13 and 6.14, respectively. For the case of $\Delta V_\mathrm{IP} = q_0 x_\mathrm{t} \Delta F/2$, the equation (6.16) shows a symmetry, which causes the resulting equilibrium occupancy difference to be centered around $k = 0$ (compare Figure 6.9).

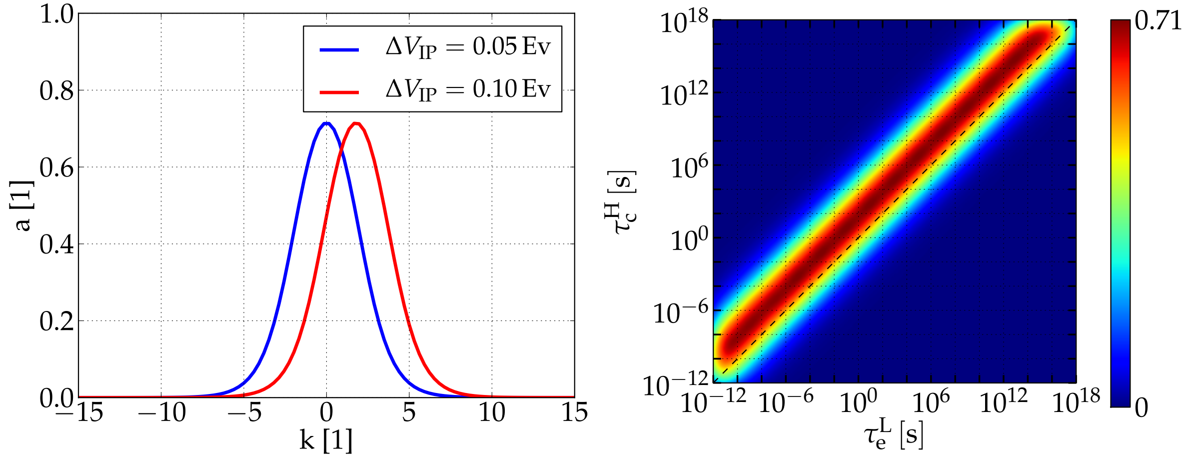

Figure 6.11: **Left**: Same as in Figure 6.10, but with $\Delta V_{IP} = 0.05\,\text{eV}$ (blue) and $\Delta V_{IP} = 0.1\,\text{eV}$ (red), both with $q_0 x_t \Delta F = 0.1\,\text{eV}$, and $T = 50°\text{C}$. **Right**: Same as in Figure 6.10, but with $\Delta V_{IP} = 0.1\,\text{eV}$, $q_0 x_t \Delta F = 0.1\,\text{eV}$, and $T = 50°\text{C}$. For this values, all NMP transitions are in the limit between strong electron-phonon coupling and negative weak electron-phonon coupling.

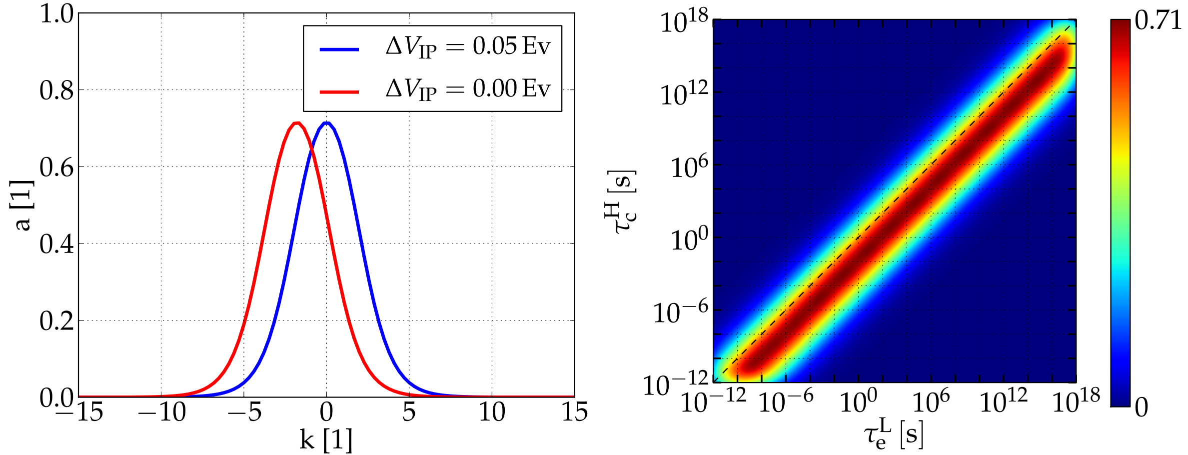

Figure 6.12: **Left**: Same as in Figure 6.10, but with $\Delta V_{IP} = 0.05\,\text{eV}$ (blue) and $\Delta V_{IP} = 0\,\text{eV}$ (red), both with $q_0 x_t \Delta F = 0.1\,\text{eV}$, and $T = 50°\text{C}$. **Right**: Same as in Figure 6.10, but with $\Delta V_{IP} = 0\,\text{eV}$, $q_0 x_t \Delta F = 0.1\,\text{eV}$, and $T = 50°\text{C}$. For this values, all NMP transitions are in the limit between strong electron-phonon coupling and positive weak electron-phonon coupling.

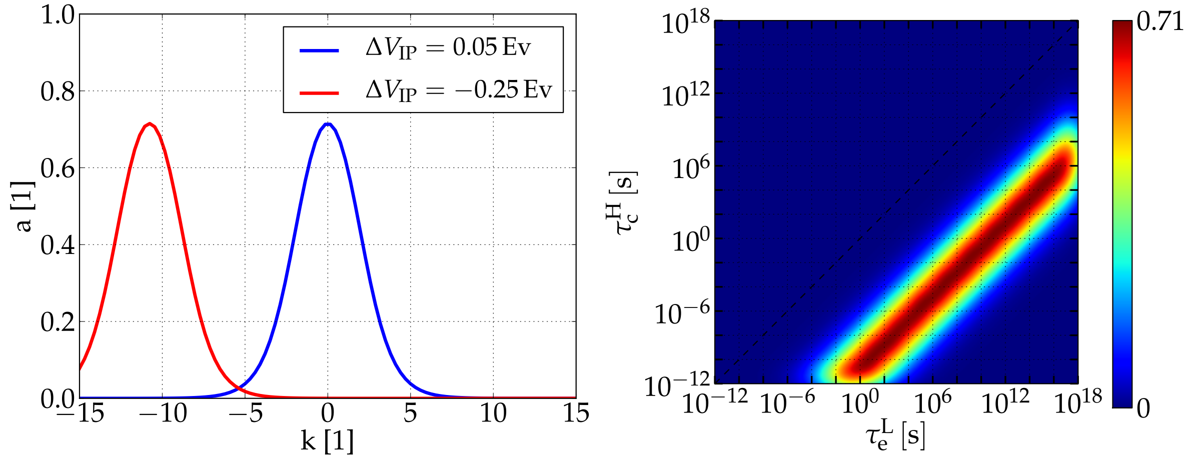

Figure 6.13: **Left**: Same as in Figure 6.10, but with $\Delta V_{IP} = 0.05\,\mathrm{eV}$ (blue) and $\Delta V_{IP} = -0.25\,\mathrm{eV}$ (red), both with $q_0 x_t \Delta F = 0.1\,\mathrm{eV}$, and $T = 50°\mathrm{C}$. **Right**: Same as in Figure 6.10, but with $\Delta V_{IP} = -0.25\,\mathrm{eV}$, $q_0 x_t \Delta F = 0.1\,\mathrm{eV}$, and $T = 50°\mathrm{C}$. For this values, all NMP transitions show positive weak electron-phonon coupling.

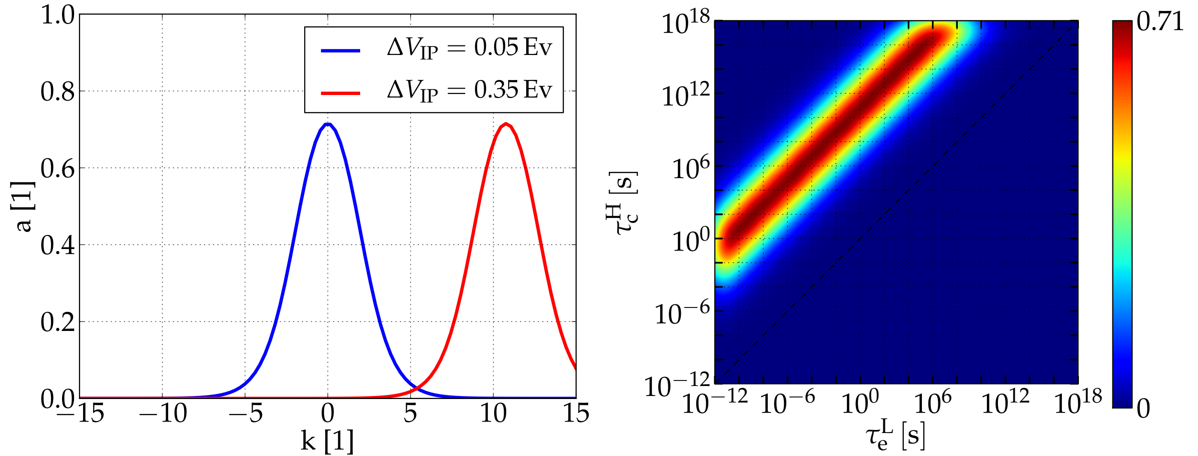

Figure 6.14: **Left**: Same as in Figure 6.10, but with $\Delta V_{IP} = 0.05\,\mathrm{eV}$ (blue) and $\Delta V_{IP} = 0.35\,\mathrm{eV}$ (red), both with $q_0 x_t \Delta F = 0.1\,\mathrm{eV}$, and $T = 50°\mathrm{C}$. **Right**: Same as in Figure 6.10, but with $\Delta V_{IP} = 0.35\,\mathrm{eV}$, $q_0 x_t \Delta F = 0.1\,\mathrm{eV}$, and $T = 50°\mathrm{C}$. For this values, all NMP transitions show negative weak electron-phonon coupling. The simulation results of the NMP four state model showed traps with negative weak electron-phonon coupling in similar regions (compare Figure 6.4).

6.2.5 Dependence on the Electric Field and the Trap Positions

In the previous section, ΔV_{IP} was investigated for certain values of $q_0 x_{\mathrm{t}} \Delta F$. Thereby, the region where traps can contribute to CET maps, was related to the coupling regime of the involved transitions. In the following, the effect of ΔF and x_{t} on the equilibrium occupancy difference (6.5) will be investigated. As a change of either ΔF or x_{t} implies a change of ΔV_{IP}, ΔV_{IP} cannot be considered independently of $q_0 x_{\mathrm{t}} \Delta F$. The resulting change of ΔV_{IP} for a change of $q_0 x_{\mathrm{t}} \Delta F$ can be quantified by $\mathrm{d}(\Delta V_{\mathrm{IP}})/\mathrm{d}(\Delta F)$, which strongly depends on the coupling regime (compare Section 3.1.7). In order to give an example for a simple case, $\Delta E_{21} = 0\,\mathrm{eV}$ and $R_{12} = 1$ will be assumed in the present subsection. For this case, $1/(q_0 x_{\mathrm{t}}) \mathrm{d}\varepsilon_{12}/\mathrm{d}F$ is found to be -0.5 (compare Figure 3.5) and thus ε_{12} can be written as

$$\varepsilon_{12} = \varepsilon_{12}(F = 0) - \frac{1}{2} q_0 x_{\mathrm{t}} F + O(F^2). \tag{6.27}$$

With the above expression, and the equations (6.18) and (6.9), one obtains

$$\begin{aligned} \Delta V_{\mathrm{IP}} &= \varepsilon_{12}^{\mathrm{H}} + V_1^{\mathrm{H}} - V_1^{\mathrm{L}} - \varepsilon_{12}^{\mathrm{L}} \\ &\approx -\frac{1}{2} q_0 x_{\mathrm{t}} F^{\mathrm{H}} + q_0 x_{\mathrm{t}} F^{\mathrm{H}} - q_0 x_{\mathrm{t}} F^{\mathrm{L}} + \frac{1}{2} q_0 x_{\mathrm{t}} F^{\mathrm{L}} \\ &\approx \frac{1}{2} q_0 x_{\mathrm{t}} \Delta F. \end{aligned} \tag{6.28}$$

The derivative of the above equation with respect to ΔF reads

$$\frac{1}{q_0 x_{\mathrm{t}}} \frac{\mathrm{d}\Delta V_{\mathrm{IP}}}{\mathrm{d}\Delta F} \approx \frac{1}{2}. \tag{6.29}$$

Figure 6.15 shows the equilibrium occupancy difference for two different values of ΔF. The corresponding values of ΔV_{IP} were chosen according to the above equation.

This results in an increase of the equilibrium occupancy difference, without shifting away from $k = 0$, which is in agreement with the observed bias dependence of simulated CET maps (compare Sections 5.14 and 6.1.1).

6.2.6 Estimated Distributions

In the previous sections a correlation between the equilibrium occupancy difference of a trap and its location in CET maps was found. This correlation depends on the difference of the intersection points ΔE_{IP}, the temperature T, and the difference of the the trap levels $q_0 x_{\mathrm{t}} \Delta F$. In the following, these quantities will be related to the trap parameters R_{12}, S_{12}, and ΔE_{21}. Thereby an expression for a will be obtained, which does not include any parameters of the NMP transition and CET maps will be estimated, based on $\tau_{\mathrm{c}}^{\mathrm{H}}$, $\tau_{\mathrm{e}}^{\mathrm{L}}$, and x_{t} of the contributing traps.

Using the inversion approximation (compare 6.2.2), the difference of the electric fields can be associated with the gate voltages $V_{\mathrm{G}}^{\mathrm{H}}$ and $V_{\mathrm{G}}^{\mathrm{L}}$. With the oxide thickness t_{ox}, this

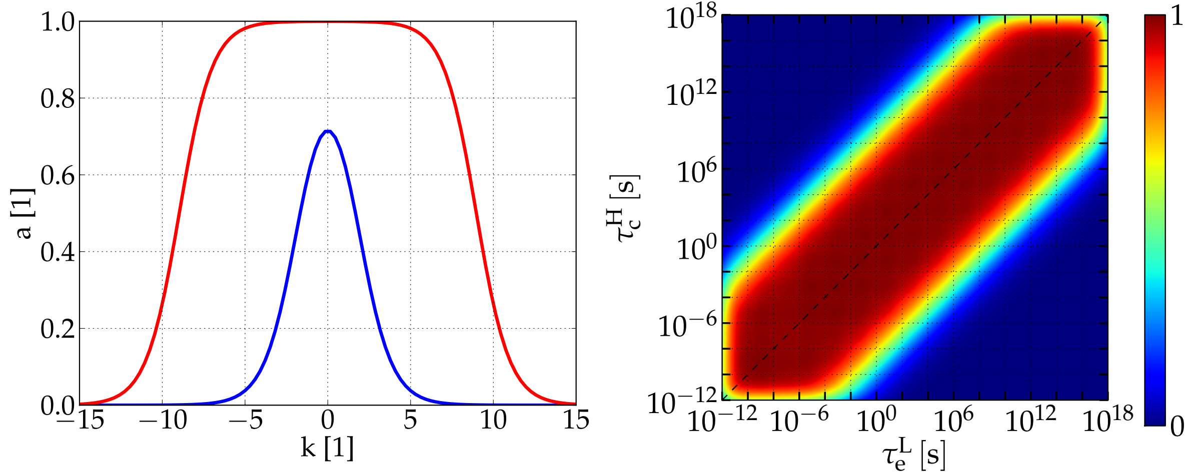

Figure 6.15: **Left**: Same as in Figure 6.10, but with $\Delta V_{\mathrm{IP}} = 0.05\,\mathrm{eV}$ and $q_0 x_{\mathrm{t}} \Delta F = 0.1\,\mathrm{eV}$ (blue) and $\Delta V_{\mathrm{IP}} = 0.25\,\mathrm{eV}$ and $q_0 x_{\mathrm{t}} \Delta F = 0.5\,\mathrm{eV}$ (red), both with $T = 50°\mathrm{C}$. **Right**: Same as in Figure 6.10, but with $\Delta V_{\mathrm{IP}} = 0.25\,\mathrm{eV}$, $q_0 x_{\mathrm{t}} \Delta F = 0.5\,\mathrm{eV}$, and $T = 50°\mathrm{C}$. Due to the increase of $q_0 x_{\mathrm{t}} \Delta F$, the equilibrium occupancy difference increases but the center of the distribution remains unchanged.

relation reads

$$\Delta F \approx \frac{V_{\mathrm{G}}^{\mathrm{H}} - V_{\mathrm{G}}^{\mathrm{L}}}{t_{\mathrm{ox}}}. \tag{6.30}$$

The difference of the intersection points depends on the time constants $\tau_{\mathrm{c}}^{\mathrm{H}}$ and $\tau_{\mathrm{e}}^{\mathrm{L}}$ via the equations (6.2) and (6.3), respectively. If the Fermi level is close to the valence band edge, the barriers are obtained as (compare equation (3.47))

$$\varepsilon_{12}^{\mathrm{H}} = \frac{1}{\beta} \ln(\tau_{\mathrm{c}}^{\mathrm{H}} p^{\mathrm{H}} v_{\mathrm{th}} \sigma_0 \vartheta) \tag{6.31}$$

$$\varepsilon_{21}^{\mathrm{L}} \approx \frac{1}{\beta} \ln(\tau_{\mathrm{e}}^{\mathrm{L}} p^{\mathrm{L}} v_{\mathrm{th}} \sigma_0 \vartheta). \tag{6.32}$$

The value of R_{12} depends on the bonding structure of the defect. Under the assumption that all traps which are described by NMP transitions have a similar bonding structure, the values of R_{12} are approximately the same for all traps. Therefore, a unique solution for S_{12} and ΔE_{21} can be found, for all combinations of ε_{12} and ε_{21}. For the case of $R = 1$, these solutions are obtained based on equation (3.60) as

$$\Delta E_{21} = \varepsilon_{12} - \varepsilon_{21} \tag{6.33}$$

$$S_{12} = 2\sqrt{\varepsilon_{12}\varepsilon_{21}} + \varepsilon_{21} + \varepsilon_{12}. \tag{6.34}$$

Based on equation (3.59), relations between these quantities can be obtained for arbitrary R_{12} as well. In order to solve the above equations, the energy barriers ε_{12} and ε_{21} have

to be evaluated at the same gate voltage. But, due to the equations (6.31) and (6.32) only $\varepsilon_{12}^{\mathrm{H}}$ and $\varepsilon_{21}^{\mathrm{L}}$ are available. Solving the above equations with $\varepsilon_{12} = \varepsilon_{12}^{\mathrm{H}}$ and $\varepsilon_{21} = \varepsilon_{21}^{\mathrm{L}}$ does not result in well defined quantities, but it yields some kind of "operating point", which will turn out to be quite suitable for reasonable values of ΔF. Now, with R_{12}, ΔE_{21}, and S_{12} at hand, substituting equation (3.64) into equation (3.59) and taking its derivative with respect to F yields

$$\frac{1}{q_0 x_{\mathrm{t}}}\frac{\mathrm{d}\varepsilon_{12}}{\mathrm{d}F} = -\frac{R_{12}\left(R_{12}\sqrt{\frac{(R_{12}^2-1)(\Delta E_{21}(F=0)-q_0 x_{\mathrm{t}}F)+S_{12}\hbar\omega}{S_{12}\hbar\omega}}-1\right)}{(R_{12}^2-1)\sqrt{\frac{(R_{12}^2-1)(\Delta E_{21}(F=0)-q_0 x_{\mathrm{t}}F)+S_{12}\hbar\omega}{S_{12}\hbar\omega}}}. \tag{6.35}$$

Therein, $\Delta E_{21}(F=0) - q_0 x_{\mathrm{t}} F$ can be approximated by ΔE_{21}, evaluated at the "operating point" via equation (6.33). The approximation

$$\frac{\mathrm{d}V_{\mathrm{IP}}}{\mathrm{d}F} \approx \frac{\Delta V_{\mathrm{IP}}}{\Delta F} \tag{6.36}$$

together with equation (6.19) yields

$$\Delta V_{\mathrm{IP}} \approx \left(\frac{1}{q_0 x_{\mathrm{t}}}\frac{\mathrm{d}\varepsilon_{12}}{\mathrm{d}F} + 1\right) q_0 x_{\mathrm{t}} \Delta F. \tag{6.37}$$

As ΔF can be obtained by equation (6.30) the substitution of equation (6.35) in the above expression yields the intersection point difference ΔV_{IP} of an NMP transition. Finally, for each combination of $\tau_{\mathrm{c}}^{\mathrm{H}}$ and $\tau_{\mathrm{e}}^{\mathrm{L}}$ the value of the equilibrium occupancy difference can be estimated using equation (6.16).

Figures 6.16, 6.17, 6.18, and 6.19 show the comparisons of the estimations of the equilibrium occupancy difference with regard to R_{12}, x_{t}, $V_{\mathrm{G}}^{\mathrm{H}}$, and T, respectively. All distributions were calculated for a device with $t_{\mathrm{ox}} = 1.4\,\mathrm{nm}$. The broadening of the distribution towards higher and lower $\tau_{\mathrm{c}}^{\mathrm{H}}$ for increasing $V_{\mathrm{G}}^{\mathrm{H}}$ is in agreement with the findings of Section 6.1.1. The effect of increasing x_{t} is similar to that of an increasing $V_{\mathrm{G}}^{\mathrm{H}}$. Furthermore, the estimations show the same temperature dependence, as it was observed in the simulations of the CET maps with the NMP four state traps (compare Figure 6.3).

6.3 Comparison of Results

The estimation of the distribution of the equilibrium occupancy difference in Section 6.2.6 allows an insight into the behavior of NMP transitions, but some crude approximations have been made. For a rough verification of the obtained results, the estimation of $a(\tau_{\mathrm{c}}^{\mathrm{H}}, \tau_{\mathrm{e}}^{\mathrm{L}})$ is applied to the trap distribution, listed in Table 5.6. Thereby a CET map is achieved, which can be compared to CET maps simulated in Section 5.5.3. Figures 6.20, 6.21, and 6.22 show the comparison of these CET maps for different temperatures and voltages. The results are in good agreement, which indicates, that the estimations are suitable.

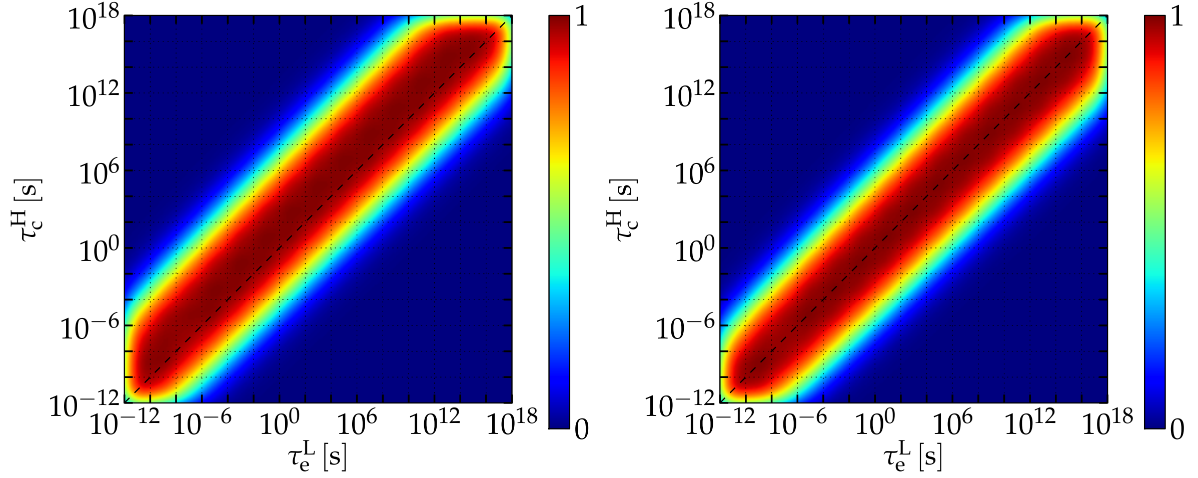

Figure 6.16: Estimation of the equilibrium occupancy difference of NMP transitions with $x_t = 0.4\,\mathrm{nm}$ and $T = 150°\mathrm{C}$ for $R_{12} = 0.6$ (left) and $R_{12} = 1$ (right). The oxide thickness of the device is 1.4 nm and the gate voltages are $V_G^H = -2\,\mathrm{V}$ and $V_G^L = -0.5\,\mathrm{V}$.

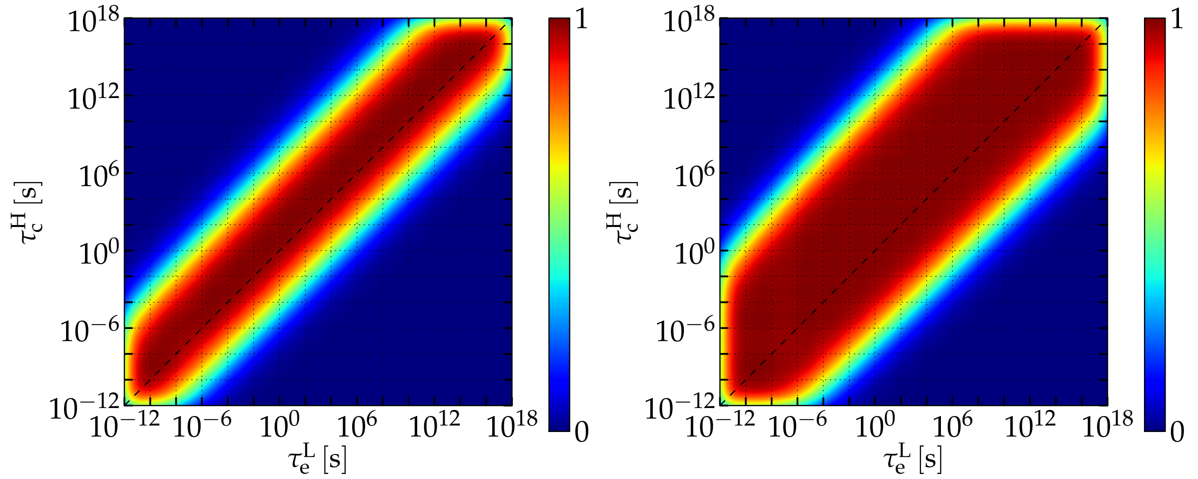

Figure 6.17: Estimation of the equilibrium occupancy difference of NMP transitions with $R_{12} = 0.6$ and $T = 150°\mathrm{C}$ for $x_t = 0.4\,\mathrm{nm}$ (left) and $x_t = 0.7\,\mathrm{nm}$ (right). The oxide thickness of the device is 1.4 nm and the gate voltages are $V_G^H = -2\,\mathrm{V}$ and $V_G^L = -0.5\,\mathrm{V}$.

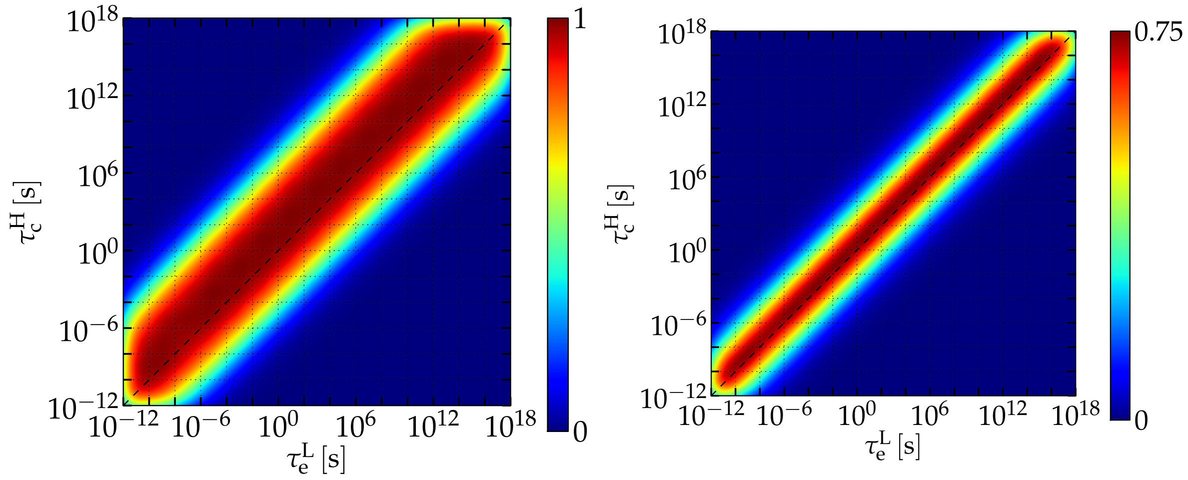

Figure 6.18: Estimation of the equilibrium occupancy difference of NMP transitions with $R_{12} = 0.6$, $T = 150°\mathrm{C}$, $x_t = 0.4\,\mathrm{nm}$, and $V_G^L = -0.5\,\mathrm{V}$ for $V_G^H = -2\,\mathrm{V}$ (left) and $V_G^H = -1\,\mathrm{V}$ (right). The oxide thickness of the device is 1.4 nm.

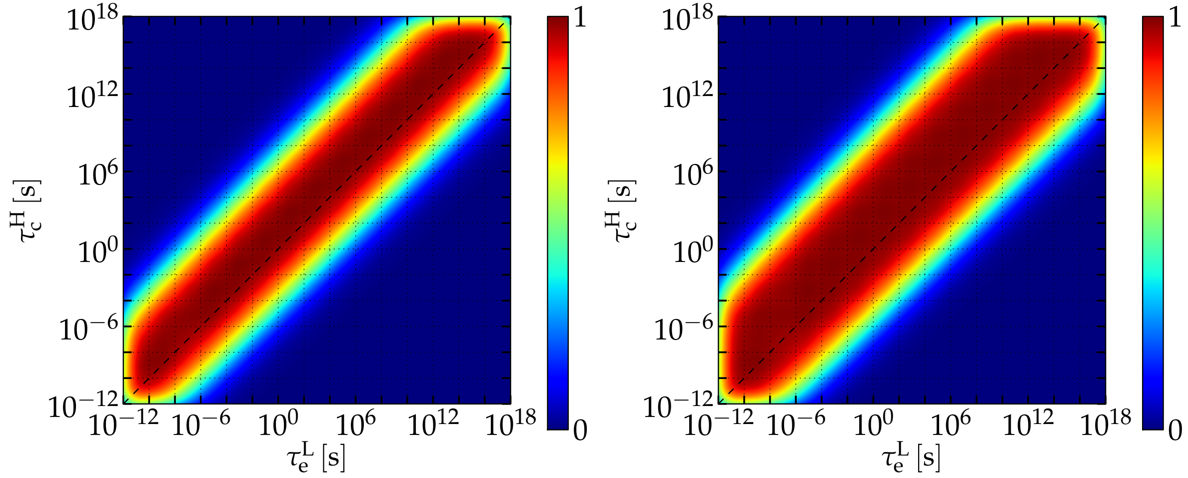

Figure 6.19: Estimation of the equilibrium occupancy difference of NMP transitions with $R_{12} = 0.6$ and $x_t = 0.4\,\mathrm{nm}$ for $T = 150°\mathrm{C}$ (left) and $T = 50°\mathrm{C}$ (right). The oxide thickness of the device is 1.4 nm and the gate voltages are $V_G^H = -2\,\mathrm{V}$ and $V_G^L = -0.5\,\mathrm{V}$.

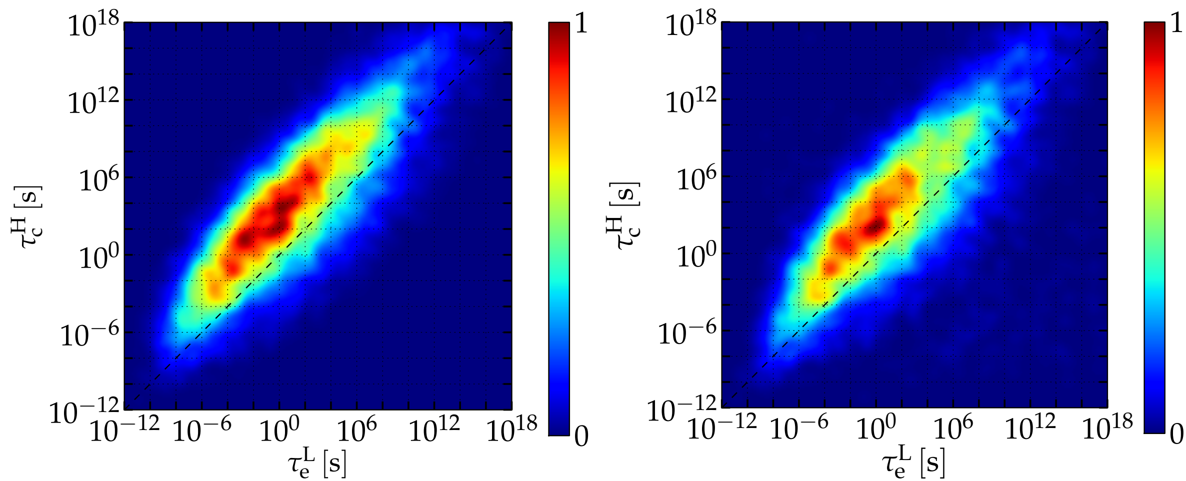

Figure 6.20: CET maps based on the NMP four state model parameters of Table 5.6 with the equilibrium occupancy difference approximated by $a(\tau_c^H, \tau_e^L)$ (left) and the exact equilibrium occupancy difference $a(\tau_c^H, \tau_c^L, \tau_e^H, \tau_e^L)$ (right). Both CET maps were simulated with $V_G^H = -2\,\mathrm{V}$, $V_G^L = -0.5\,\mathrm{V}$, and $T = 50°\mathrm{C}$.

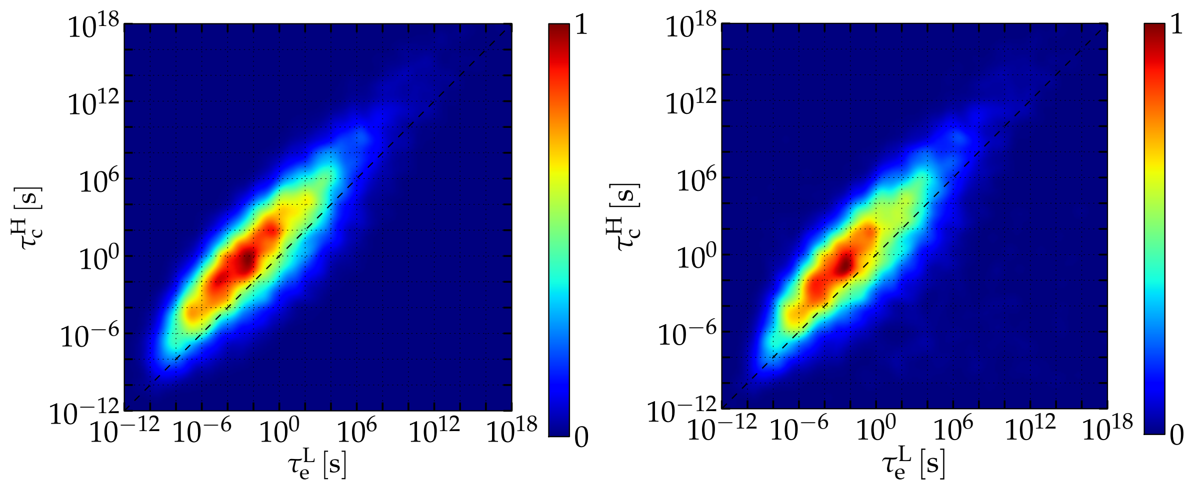

Figure 6.21: Same as in Figure 6.20 but with $V_G^H = -2\,\mathrm{V}$, $V_G^L = -0.5\,\mathrm{V}$, and $T = 150°\mathrm{C}$.

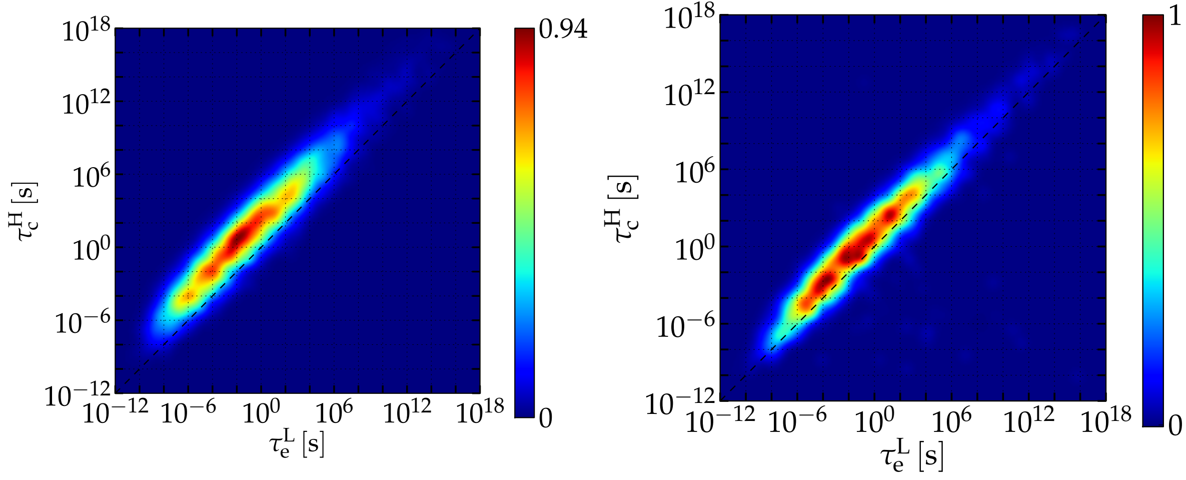

Figure 6.22: Same as in Figure 6.20 but with $V_G^H = -1\,\text{V}$, $V_G^L = -0.5\,\text{V}$, and $T = 150°\text{C}$.

6.4 Conclusions

The bias and temperature dependence of CET maps with traps modeled by the NMP four state model were discussed. Furthermore, transitions in the regime of negative weak electron phonon coupling in CET maps were investigated. A correlation between the equilibrium occupancy difference of NMP transitions and the location where they contribute on CET maps was pointed out and quantified. The findings about the bias dependence of the equilibrium occupancy difference of NMP transitions was in agreement with the bias dependence observed in CET maps. Additionally, an estimation of the distribution of the equilibrium occupancy difference for NMP transitions was derived. The dependence of these distributions were in agreement with all previous observations as well. Finally, the estimation was verified by a comparison with the results of exact simulations of CET maps of the NMP four state model.

CHAPTER 7 Summary and Outlook

Charge capture and emission of oxide defects in pMOSFETs and the resulting threshold voltage shift have been simulated and investigated in this work. In order to describe the temperature and bias dependence of the time constants of single defects, the NMP four state model was employed. Utilizing the all states of this model, TDDS measurement data of fixed positive charge traps, as well as switching traps were accurately reproduced in this work. This required proper estimation of the parameters of the NMP four state model, followed by their optimization.

The charge of oxide traps causes device degradation, which can be quantified by the shift of the threshold voltage. This degradation was simulated for a large-area pMOSFET. As a multitude of defects contribute to the degradation of larger devices, the corresponding trap parameters were defined by distribution functions. Still, the optimization required a lot of parameters. Additionally, a second model had to be employed, in order to account for the permanent component of BTI. Based on these two models, provided measurement data of threshold voltage shifts for different temperatures and gate voltages was reproduced. This involved the processing of the measurement data, the creation of the correct device structure, and the optimization of a reasonable initial guess.

Finally, a good match of the measured and simulated threshold voltage shifts was obtained. The resulting distribution of the trap parameters was investigated thoroughly, in order to verify the correct modeling and to understand the complex processes involved in BTI and its simulation. Additionally, CET maps were calculated, based on the obtained trap distribution. In these simulated maps all traps can be investigated, independent of whether they are visible in experiments or not. This allowed to understand the temperature and bias dependence of CET maps. Furthermore, a detailed discussion about NMP transitions and the equilibrium occupancy difference revealed interesting connections between the time constants of traps, and their contribution to threshold voltage shifts.

The promising results of this work confirmed the correctness of the NMP four state model, and encourage further verification of simulated and measured data with a focus on CET maps.

Bibliography

[1] M. Uren, M. Kirton, and S. Collins, "Anomalous Telegraph Noise in Small-Area Silicon Metal-Oxide-Semiconductor Field-Effect Transistors," *Physical Review B*, vol. 37, no. 14, pp. 8346–8350, May 1988.

[2] T. Grasser, K. Rott, H. Reisinger, P.-J. Wagner, W. Goes, F. Schanovsky, M. Waltl, M. Toledano-Luque, and B. Kaczer, "Advanced Characterization of Oxide Traps: The Dynamic Time-Dependent Defect Spectroscopy," in *Proc.IRPS*, 2013, pp. 2D.2.1–2D.2.7.

[3] D. Schroder and J. Babcock, "Negative Bias Temperature Instability: Road to Cross in Deep Submicron Silicon Semiconductor Manufacturing," *J.Appl.Phys.*, vol. 94, no. 1, pp. 1–18, 2003.

[4] D. Schroder, "Negative Bias Temperature Instability: What Do We Understand?" *Microelectron.Reliab.*, vol. 47, no. 6, pp. 841–852, 2007.

[5] F. Schanovsky, O. Baumgartner, V. Sverdlov, and T. Grasser, "A Multi Scale Modeling Approach to Non-Radiative Multi Phonon Transitions at Oxide Defects in MOS Structures," *Journ. of Comp. Electronics*, vol. 11, no. 3, pp. 218–224, 2012.

[6] F. Schanovsky, W. Goes, and T. Grasser, "An Advanced Description of Oxide Traps in MOS Transistors and its Relation to DFT," *Journ. of Comp. Electronics*, vol. 9, pp. 135–140, 2010.

[7] A. Mysovsky, P. Sushko, S. Mukhopadhyay, A. Edwards, and A. Shluger, "Calibration of Embedded-Cluster Method for Defect Studies in Amorphous Silica," *Phys.Rev.B*, vol. 69, no. 8, p. 085202, 2004.

[8] P. Blöchl, "First-Principles Calculations of Defects in Oxygen-Deficient Silica Exposed to Hydrogen," *Phys.Rev.B*, vol. 62, no. 10, pp. 6158–6179, 2000.

[9] T. Grasser, "Stochastic Charge Trapping in Oxides: From Random Telegraph Noise to Bias Temperature Instabilities," *Microelectron.Reliab.*, vol. 52, no. 1, pp. 39–70, 2012.

[10] R. Entner, "Modeling and Simulation of Negative Bias Temperature Instability," Ph.D. dissertation, Technische Universität Wien, 2007.

[11] B. Deal, "Standardized Terminology for Oxide Charges Associated with Thermally Oxidized Silicon," *IEEE Transactions on Electron Devices*, vol. 27, no. 3, pp. 606–608, Mar 1980.

[12] D. Fleetwood, ""Border Traps" in MOS Devices," *IEEE Trans.Nucl.Sci.*, vol. 39, no. 2, pp. 269–271, 1992.

[13] T. Grasser, T. Aichinger, G. Pobegen, H. Reisinger, P. Wagner, J. Franco, M. Nelhiebel, and B. Kaczer, "The 'Permanent' Component of NBTI: Composition and Annealing," in *Proc.IRPS*, 2011, pp. 6A.2.1–6A.2.9.

[14] T. Grasser, B. Kaczer, P. Hehenberger, W. Goes, R. O'Connor, H. Reisinger, W. Gustin, and C. Schlünder, "Simultaneous Extraction of Recoverable and Permanent Components Contributing to Bias-Temperature Instability," in *Proc.IEDM*, 2007, pp. 801–804.

[15] T. Grasser, P.-J. Wagner, P. Hehenberger, W. Goes, and B. Kaczer, "A Rigorous Study of Measurement Techniques for Negative Bias Temperature Instability," *IEEE Trans.Dev.Mater.Rel.*, vol. 8, no. 3, pp. 526 – 535, 2008.

[16] M. Denais, A. Bravaix, V. Huard, C. Parthasarathy, G. Ribes, F. Perrier, Y. Rey-Tauriac, and N. Revil, "On-the-fly Characterization of NBTI in Ultra-Thin Gate Oxide pMOSFET's," in *Proc.IEDM*, 2004, pp. 109–112.

[17] T. Grasser, H. Reisinger, P.-J. Wagner, and B. Kaczer, "The Time Dependent Defect Spectroscopy for the Characterization of Border Traps in Metal-Oxide-Semiconductor Transistors," *Phys.Rev.B*, vol. 82, no. 24, p. 245318, 2010.

[18] M. Waltl, P.-J. Wagner, H. Reisinger, K. Rott, and T. Grasser, *Advanced Data Analysis Algorithms for the Time-Dependent Defect Spectroscopy of NBTI.* Institute of Electrical and Electronics Engineers, Oct 2012, pp. 74–79.

[19] T. Grasser, P.-J. Wagner, H. Reisinger, T. Aichinger, G. Pobegen, M. Nelhiebel, and B. Kaczer, *Analytic Modeling of the Bias Temperature Instability Using Capture/Emission Time Maps.* Institute of Electrical and Electronics Engineers, Dec 2011, pp. 27.4.1–27.4.4.

[20] P. Lenahan and J. Conley, "What Can Electron Paramagnetic Resonance Tell Us about the Si/SiO_2 System?" *J.Vac.Sci.Technol.B*, vol. 16, no. 4, pp. 2134–2153, 1998.

[21] P. Lenahan, P. Campbell, T. Krishnan, and S. Krishnan, "A Model for NBTI in Nitrided Oxide MOSFETs Which Does Not Involve Hydrogen or Diffusion," *IEEE Trans.Dev.Mater.Rel.*, vol. 99, p. 1, 2010.

[22] J. M. M. de Nijs, K. G. Druijf, V. V. Afanas'ev, E. van der Drift, and P. Balk, "Hydrogen Induced Donor-Type Si/SiO2 Interface States," *Applied Physics Letters*, vol. 65, no. 19, p. 2428, 1994.

[23] P. Blöchl and J. Stathis, "Aspects of Defects in Silica Related to Dielectric Breakdown of Gate Oxides in MOSFETs," *Phys.B*, vol. 273-274, pp. 1022–1026, 1999.

[24] M. Boero, A. Pasquarello, J. Sarnthein, and R. Car, "Structure and Hyperfine Parameters of E_1' Centers in α-Quartz and in Vitreous SiO_2," *Phys.Rev.Lett.*, vol. 78, no. 5, pp. 887–890, 1997.

[25] T. Grasser, B. Kaczer, W. Goes, T. Aichinger, P. Hehenberger, and M. Nelhiebel, "Understanding Negative Bias Temperature Instability in the Context of Hole Trapping (Invited Paper)," *Microelectron.Eng.*, vol. 86, no. 7-9, pp. 1876–1882, 2009.

[26] P. Blöchl and J. Stathis, "Hydrogen Electrochemistry and Stress-Induced Leakage Current in Silica," *Phys.Rev.Lett.*, vol. 83, no. 2, pp. 372–375, 1999.

[27] K. Huang and A. Rhys, "Theory of Light Absorption and Non-Radiative Transitions in F-Centres," *Proc.RoyalSoc. of London. Ser. A*, vol. 204, pp. 406–423, 1950.

[28] M. Born and R. Oppenheimer, "Zur Quantentheorie der Molekeln," *Annalen der Physik*, vol. 389, no. 20, pp. 457–484, 1927.

[29] W. Goes, F. Schanovsky, and T. Grasser, *The Bias Temperature Instability: Experiment, Theory, and Modeling for Devices and Circuits* . Springer-Verlag, 2013, ch. Advanced Modeling of Oxide Defects.

[30] W. Nolting, *Grundkurs Theoretische Physik 5/2: Quantenmechanik - Methoden und Anwendungen.* Springer-Verlag, 2006.

[31] T. Grasser, H. Reisinger, P.-J. Wagner, F. Schanovsky, W. Goes, and B. Kaczer, "The Time Dependent Defect Spectroscopy (TDDS) for the Characterization of the Bias Temperature Instability," in *Proc.IRPS*, 2010, pp. 16 –25.

[32] A. Nitzan, *Chemical Dynamics in Condensed Phases.* Oxford University Press, 2006.

[33] O. Ibe, *Markov Processes for Stochastic Modeling.* Academic Press, 2009.

[34] T. Grasser, B. Kaczer, W. Goes, T. Aichinger, P. Hehenberger, and M. Nelhiebel, "A Two-Stage Model for Negative Bias Temperature Instability," in *Proc.IRPS*, 2009, pp. 33–44.

[35] *GTS Vision / Structure User Manual.* [Online]. Available: www.globaltcad.com

[36] *Minimos-NT User Manual.* [Online]. Available: www.globaltcad.com

[37] M. Bina, O. Triebl, B. Schwarz, M. Karner, B. Kaczer, and T. Grasser, “Simulation of Reliability on Nanoscale Devices,” in *Proc.SISPAD*, 2012, pp. 109–112.

[38] *GTS Framework User Manual*. [Online]. Available: www.globaltcad.com

[39] R. Plasun, “Optimization of VLSI Semiconductor Devices,” Ph.D. dissertation, Technische Universität Wien, 1999.

[40] W. Goes, F. Schanovsky, H. Reisinger, B. Kaczer, and T. Grasser, “Bistable Defects as the Cause for NBTI and RTN,” *Solid State Phenomena*, vol. 178-179, pp. 473–482, Aug 2011.

[41] G. Pobegen and T. Grasser, “On the Distribution of NBTI Time Constants on a Long, Temperature-Accelerated Time Scale,” *IEEE Transactions on Electron Devices*, vol. 60, no. 7, pp. 2148–2155, Jul 2013.

[42] T. Tewksbury, “Relaxation Effects in MOS Devices due to Tunnel Exchange with Near-Interface Oxide Traps,” Ph.D. Thesis, MIT, 1992.

[43] A. Asenov, R. Balasubramaniam, A. Brown, and J. Davies, “RTS Amplitudes in Decananometer MOSFETs: 3-D Simulation Study,” *IEEE Trans.Elect.Dev.*, vol. 50, no. 3, pp. 839–845, 2003.

[44] B. Kaczer, P. Roussel, T. Grasser, and G. Groeseneken, “Statistics of Multiple Trapped Charges in the Gate Oxide of Deeply Scaled MOSFET Devices-Application to NBTI,” *IEEE Elect.Dev.Let.*, vol. 31, pp. 411–413, 2010.